**POLITECNICO**

MILANO 1863

SCUOLA DI INGEGNERIA INDUSTRIALE
E DELL'INFORMAZIONE

# Ligand field and magnetic excitations in High Entropy Oxides studied by RIXS

TESI DI LAUREA MAGISTRALE IN
ENGINEERING PHYSICS

Author: **Davide Impelluso**

Student ID: 962595
Advisor: Prof. Marco Moretti
Academic Year: 2022-2023

# Abstract

High Entropy Oxides (HEOs) are an emergent class of materials characterized by high configurational disorder. The growing interest in these materials is motivated by their unique properties, including low thermal conductivity, colossal dielectric constant and superionic conductivity. This work proposes the very first study of the structural, electronic and magnetic properties of prototypical HEOs based on resonant inelastic x-ray scattering (RIXS). Specifically, rock-salt compounds $Mg_{0.2}Cu_{0.2}Ni_{0.2}Co_{0.2}Zn_{0.2}O$ (Mg-CNCZ) and $Cu_{0.25}Ni_{0.25}Co_{0.25}Zn_{0.25}O$ (CNCZ) have been tested. RIXS measurements have been performed at the copper $L_3$ absorption edge, at distinct scattering geometries and incident photon polarization. Ligand field, including $dd$ and charge-transfer, excitations evidence a sizeable Jahn-Teller distortion of the $CuO_6$ octahedra, which is larger for Mg-CNCZ than for CNCZ, and allow us to estimate the energy gain associated to the distortion, a missing information in the literature. The low-energy spectral region shows features, which can likely be assigned to magnetic excitations. Our major clue is the observation that the energy of the magnetic peak in Mg-CNCZ is lower than in CNCZ because of the extra non-magnetic ion present in the lattice of the former, which reduces the effective magnetic interaction strength: based on this argument, we can quantitatively explain the relative energies of the magnetic peaks in the two systems and note that RIXS effectively probes collective excitations that are coherently excited at multiple resonant sites. In light of this, we could explain the momentum dependence of magnetic excitations within the framework of a simple Heisenberg model with an effective antiferromagnetic coupling of approximately 22 meV. This work demonstrates that RIXS provides a wealth of information about the structural, electronic and magnetic properties of Mg-CNCZ and CNCZ, and could possibly do the same for many other HEOs.

# Sommario

Gli ossidi ad alta entropia (High Entropy Oxides, HEOs) sono una emergente classe di materiali ad elevato disordine configurazionale. Il crescente interesse diffusosi nella comunità della scienza dei materiali è motivato dalle proprietà uniche di questi ossidi, tra le quali citiamo bassa conduttività termica, costante dielettrica colossale e conduttività superionica. Questo lavoro di tesi propone un innovativo studio sulle proprietà strutturali, elettroniche e magnetiche di prototipici HEOs basato sulla tecnica resonant inelastic x-ray scattering (RIXS). In particolare, abbiamo testato i composti a struttura rock-salt $Mg_{0.2}Cu_{0.2}Ni_{0.2}Co_{0.2}Zn_{0.2}O$ (Mg-CNCZ) e $Cu_{0.25}Ni_{0.25}Co_{0.25}Zn_{0.25}O$ (CNCZ). Le misure RIXS sono state effettuate alla soglia $L_3$ del rame, a diverse geometrie di scattering e polarizzazione incidente. Le eccitazioni di campo ligante, incluse le $dd$ e le eccitazioni charge-transfer, evidenziano una considerevole distorsione di tipo Jahn-Teller delle unità ottaedriche $CuO_6$, che risulta maggiore nel composto Mg-CNCZ, e ci permettono di stimare il guadagno energetico associato alla distorsione, un'informazione assente nella letteratura. La regione spettrale a bassa energia evidenzia picchi che possono essere assegnati a eccitazioni magnetiche. La caratteristica principale è l'osservazione del fatto che l'energia del picco magnetico in Mg-CNCZ è minore che in CNCZ, a causa della presenza di un extra ione non magnetico nel reticolo, che riduce la forza dell'interazione magnetica effettiva: sulla base di questa affermazione, possiamo spiegare quantitativamente le energie relative dei picchi magnetici nei due sistemi e notare che il RIXS sonda eccitazioni collettive che sono eccitate coerentemente nei siti risonanti. Alla luce di questo, abbiamo dato una spiegazione all'andamento delle eccitazioni magnetiche in funzione di variazioni di momento trasferito nel contesto del modello di Heisenberg, con un effettivo accoppiamento antiferromagnetico di approssimativamente 22 meV. Questo lavoro dimostra che il RIXS fornisce abbondanti informazioni sulle proprietà strutturali, elettroniche e magnetiche di Mg-CNCZ e CNCZ, e potrebbe eventualmente fare lo stesso per molti altri HEOs.

# Contents

# 1 | High Entropy Oxides

In the early 2000s the materials science community has explored a new class of multi-element alloy systems called High Entropy Alloys (HEAs). This branch of research was first introduced in 2004 by Yeh et al. [1] and Cantor et al. [2]. The term "high entropy" is attributed by virtue of their many constituent elements: HEAs are syhtesized by mixing at least five elements in roughly equimolar concentration. One might think that the resulting high degree of configurational disorder would lead to the synthesis of multi-phase alloys, which are complex materials with limited applications. Nevertheless, experiments show that the high-entropy character is fundamental in the formation of a single-phase material and is at the basis of its mechanism of stabilization.

In the following years the realm of high-entropy materials rapidly expanded including novel and interesting families of compositionally complex compounds (Fig. 1.1).
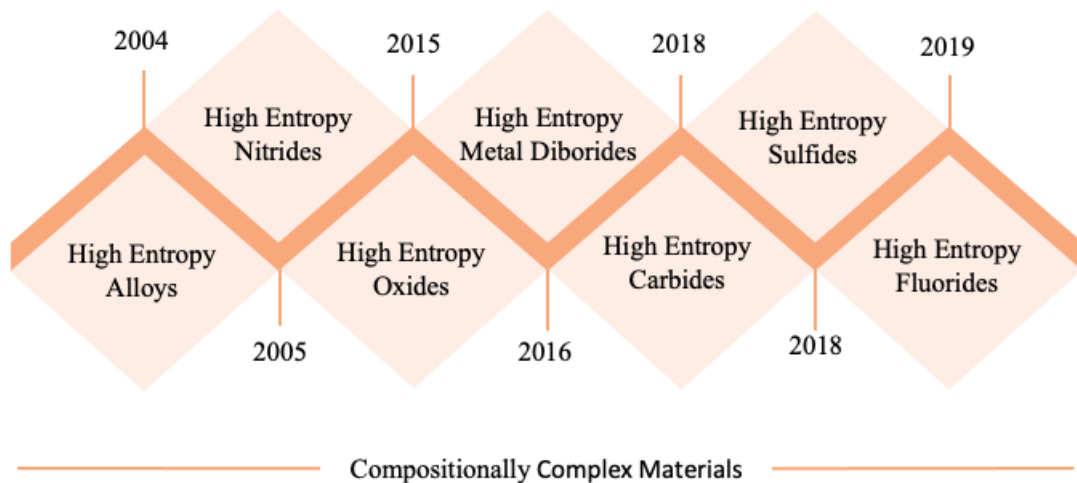


Figure 1.1: A timeline of the synthesis of new high-entropy materials is proposed. The high number of classes testifies the increasing interest in compositionally complex materials. Adapted from B. L. Musicò et al. [3].

Among them, High Entropy Oxides (HEOs) appear to be very promising for a wide range of applications and represent the main topic of this work. The first HEO was synthesized

in 2015, when the multi-metal oxide $Mg_{0.2}Co_{0.2}Ni_{0.2}Cu_{0.2}Zn_{0.2}O$ was shown to stabilize in a rock-salt single phase. Its properties will be better discussed in chapter 1.2. Actually, over the years oxides with many other crystal structures have been synthesized, including fluorite oxides (HEFOs) [4], perovskite oxides [5], spinel oxides [6] and many more [7]. Even though there is no clear and widely agreed definition of HEOs, it is still possible to underline some of their main properties and remark important aspects [8]:

- they are single-phase crystalline materials where the high level of entropy is not related to an atomic positional disorder (as it would be in amorphous materials): entropy is primarily related to the random distribution of metallic cations of different chemical species on the cation sub-lattice sites;

- in most of the cases, the single phase is observed only at sufficiently high temperatures, while multiple phases are observed at low temperature conditions. A deeper study of the transitions to single-phase states is provided in the following section (1.1);

- another peculiar property of HEOs is the temperature-controlled reversibility of the single-phase to multi-phase transition, evidence of the crucial role played by entropy in the material stabilization [9–11].

In conclusion, we mention that there is a strong interest in studying this class of oxides. Exciting properties and results were reported, including excellent strength and ductility [12], colossal dielectric constant [13], room temperature superionic conductivity [14], which can be tuned by controlling the phase stabilization process.

## 1.1.   The role of entropy in HEOs

The complete understanding of the entropy-driven stabilization of HEOs requires the introduction of some thermodynamic arguments. The multi-phase to single-phase transition occurs if the variation of Gibbs free energy $\Delta G$ associated to it is negative: $\Delta G < 0$. We recall that the Gibbs free energy $G$ is a thermodynamic potential defined as

$$G = H - TS \tag{1.1}$$

where $T$ is the temperature of the thermodynamic system, $H$ is the enthalpy and $S$ the is entropy. The free energy variation of the transition in HEOs must take into account both an enthalpic and an entropic contribution. The enthalpic contribution is the enthalpy of formation $H_f$, i.e., the variation of enthalpy caused by the formation of a compound from its constituent elements. The variation of entropy is, instead attributed to the compositional disorder associated to the random arrangement of metallic ions on the cationic sub-lattice; it is denominated **configurational entropy**. From equation 1.1 we obtain

$$\Delta G = \Delta H_f - T\Delta S_{config} \tag{1.2}$$

Equation 1.2 encompasses some approximations: in particular, we neglect the existence of any kind of disorder within the oxygen sub-lattice (vacancies or other point defects), that would have contributed with a further increase of the total entropy [15]; moreover other entropy enhancements due to the local environment [8] - such as expansions and contractions of the oxygen sub-lattice, Jahn-Teller distortions, vacancies, interstitials or anti-site defects - are not considered; finally, it is assumed that the synthesized HEO compound is an ideal solid solution, so that further enthalpic contributions due to enthalpy of mixing are neglected [10].

The configurational entropy of a metal oxide with $N$ different metal cations can be evaluated as [7, 10, 15]

$$\Delta S_{config} = -R \sum_{i=1}^{N} \chi_i \ln \chi_i \tag{1.3}$$

where $\chi_i$ represents the molar fraction of the $i^{th}$ chemical species and $R = 8.314$ Jmol$^{-1}$K$^{-1}$ is the universal gas constant. In an equimolar system $\chi_i = 1/N$ and equation 1.3 can be simplified to

$$\Delta S_{config} = R \ln N \tag{1.4}$$

It is clear that configurational entropy is an increasing function of the number $N$ of
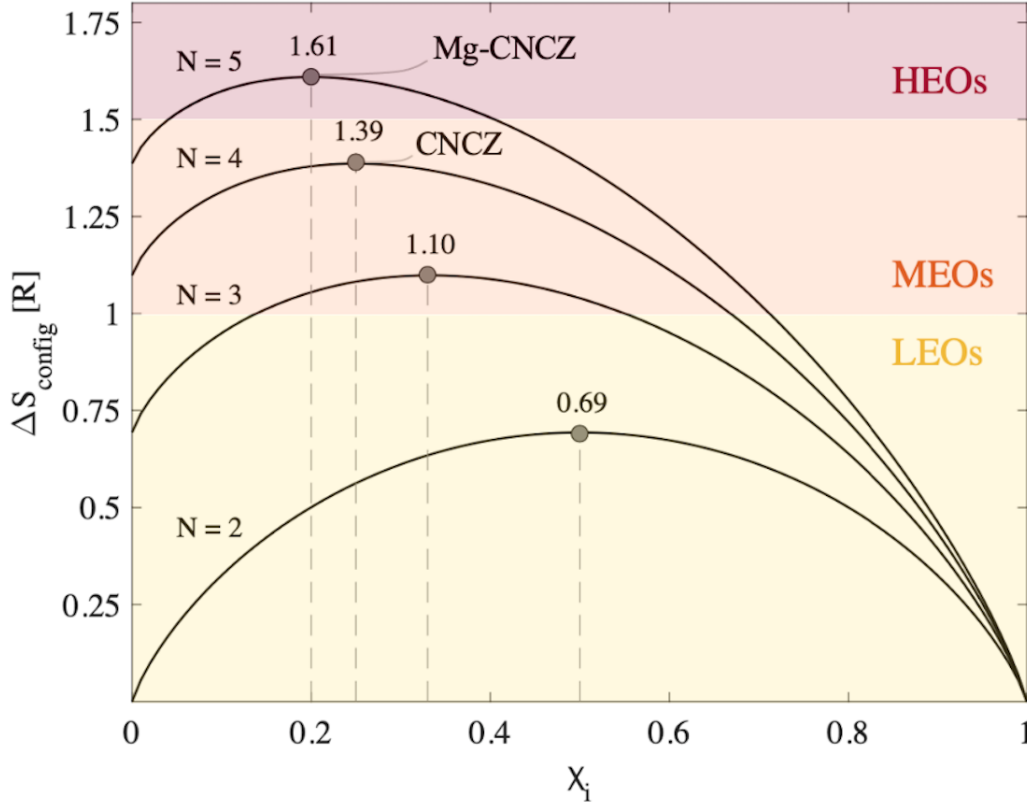
constituent elements.



Figure 1.2: Configurational entropy dependence on number of components $N$ and on their molar fraction $\chi_i$. For each number of cations, the value of $S_{config} = R \ln N$ at equimolar cation ratios is reported.

According to this definition, attempts to distinguish HEOs from Medium Entropy Oxides (MEOs) and Low Entropy Oxides (LEOs) were proposed [8, 16]. Oxides with a configurational entropy larger than $1.5R$ are classified as HEOs. According to equation 1.4, at least 5 different metal constituents are required to achieve this level of disorder. An oxide material satisfying the condition $S_{config} \leq 1.0R$ is instead classified as a LEO, while if $1.0R \leq S_{config} \leq 1.5R$ the material is a MEO. Figure 1.2 shows how configurational entropy depends on the number $N$ and on the molar fraction $\chi_i$ of the constituent metal cations. One can see that entropy is maximized at equimolar cation ratios.

Now that we have introduced the main terms of equation 1.2, we immediately understand how configurational disorder and enthalpy of formation affect the multi-phase to single-phase transition in HEOs. The analytical condition required to obtain the stabilization

of the single phase in a high entropy material with generic molar cation ratios is

$$\Delta H_f < RT \sum_{i=1}^{N} \chi_i \ln \chi_i \qquad (1.5)$$

and clarifies that a HEO is formed when the entropic contribution dominates the free energy landscape over $\Delta H_f$. In this framework, the scientific community felt the necessity to distinguish High Entropy Oxides from the so-called Entropy Stabilized Oxides (ESOs) [7, 15, 17]. ESOs are a sub-class of HEOs identified by those materials having both a positive enthalpy of formation and a sufficiently high configurational entropy, for which the single-phase state is reached uniquely due to the entropic contribution. Instead, the "high entropy" terminology in HEOs simply refers to the system with high configurational entropy, but possibly with $\Delta H_f < 0$.

Generally, temperature plays a crucial role in the single phase stabilization. For example, rock-salt $Mg_{0.2}Co_{0.2}Ni_{0.2}Cu_{0.2}Zn_{0.2}O$ is formed solely at high temperatures, and this is a common result among all ESOs. Equation 1.5 consistently clarifies that elevated temperatures promote the multi-phase to single-phase transition, given that the entropic term is proportional to $T$. Specifically, a critical temperature $T_c$ may be associated to the temperature required to satisfy the condition $\Delta H_f = T_c \Delta S_{config}$. When $T < T_c$, the single phase is not stable anymore and phase segregation is observed. People relies on quenching procedures to kinetically freeze the single-phase state and prevent the system from relaxing to the minimum of the free energy landscape, which corresponds to a multi-phase system [8]. To summarize, we recall that the synthesis of HEOs requires a negative variation of Gibbs free energy associated to the single-phase to multi-phase transition. This is done by

- heating up the multi-phase system, therefore incrementing $T\Delta S_{config}$;

- increasing the total number of constituent metal cations $N$;

- forcing equimolar cation ratios to maximize $\Delta S_{config}$.

## 1.2. (MgCoNiCuZn)O: the prototypical HEO

In 2015, Rost et al. [10] reported the synthesis of $Mg_{0.2}Co_{0.2}Ni_{0.2}Cu_{0.2}Zn_{0.2}O$ (from now on, Mg-CNCZ), a single-phase five-component HEO obtained from equimolar mixture of MgO, CuO, ZnO, NiO and CoO. Here we discuss about some of the most relevant properties of this prototypical compound.

As already mentioned, it exhibits a rock-salt structure: the crystal lattice is obtained from the superposition of one FCC oxygen sub-lattice and one FCC metal cations sub-lattice. A representation of the Mg-CNCZ crystal structure is proposed in Fig. 1.3.
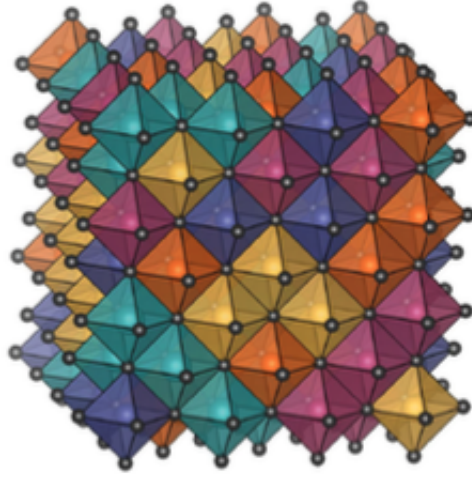


Figure 1.3: Structure of a generic five-component rock-salt HEO. Differently coloured octahedral cages highlight the randomness in the distribution of metal cations. Picture taken from Solveig S. Aamlid et al. [8].

Metal cations are randomly and homogeneously distributed over the sub-lattice sites, while locally they are surrounded by an octahedral cage of $O^{2-}$ ions. The reported lattice parameter values span from 4.214 Å to 4.235 Å [13, 18, 19].

Regarding thermal properties, Mg-CNCZ exhibits a low thermal conductivity $\kappa$, in the order of 3 $Wm^{-1}K^{-1}$ [20]. This is a common property to all members of the HEOs family. Indeed, materials with high configurational entropy are characterized by an increased density of phonon scattering centers, responsible for the large thermal resistance [21]. Consistently, all precursor oxides (CoO, CuO, MgO, NiO and ZnO) have a higher thermal conductivity by at least one order of magnitude at room temperature (> 20 $Wm^{-1}K^{-1}$) [22–26]. The thermal conductivity of Mg-CNCZ compares to that of amorphous materials (around $\sim$ 1 $Wm^{-1}K^{-1}$ [27]), where the density of scattering centers is even larger. However, they possess a much larger electrical conductivity (see below) which makes them optimal

materials for thermoelectric applications. Interestingly, experiments show that adding a cation species to Mg-CNCZ (such as Sc, Sb, Sn, Cr, Ge) leads to a reduction of the thermal conductivity by a factor of 2 [20], hinting that configurational disorder may be regarded as an additional tool to design their thermal properties.

Electrochemical Impedance Spectroscopy [28] studies on the temperature dependence of electrical conductivity $\sigma_m$ revealed that it increases with temperature [29], which is typical of a thermally activated process, according to the following expression:

$$\sigma_m \sim \frac{1}{T} e^{-\frac{E_a}{k_B T}}, \qquad (1.6)$$

where $k_B$ is the Boltzmann constant, $E_a$ is the polaron activation energy and $T$ is the temperature of the system. Experimental data are plotted on an Arrhenius plot in Fig. 1.4.
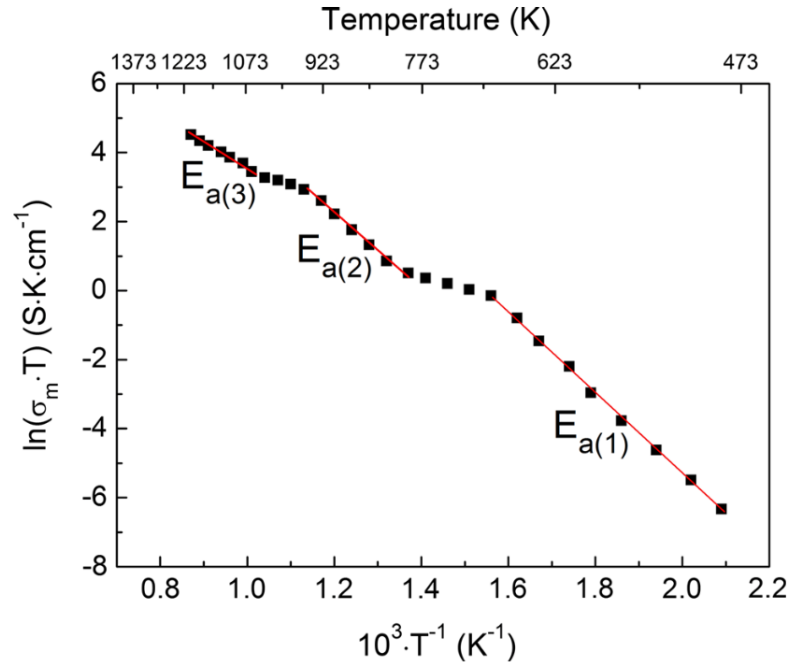


Figure 1.4: Electrical conductivity of Mg-CNCZ in logarithmic scale as a function of $T^{-1}$ [29].

Different linear dependencies are observed in three temperature regimes. Since the slope in an Arrhenius plot is related to the activation energy of the process, three distinct activation energies are assigned: $E_{a(1)} = 1.01 \pm 0.01$ eV is the activation energy of the process in the low $T$ regime, $E_{a(2)} = 0.91 \pm 0.03$ eV is referred to a medium $T$ regime and $E_{a(3)} = 0.62 \pm 0.03$ eV is assigned to the activation energy in the high $T$ regime. Balcerzak

et al. suggest that the change of the slope is related to phase transformation processes upon heating, such as phase segregation due to the low compatibility of $Cu^{2+}$ and $Zn^{2+}$ with other constituent elements. The authors also reported that $\sigma_m$ was $8.0 \times 10^{-2}$ Scm[-1] at 1148 K, when Mg-CNCZ possesses a rock-salt single phase. This value is comparable to the electrical conductivity of semiconductors, and it is several orders of magnitude larger than conductivity in insulators; as a reference, at room temperature, the electrical conductivity of Germanium is $2.2 \times 10^{-2}$ Scm[-1] [30], while in insulating fused quartz it is equal to $1.3 \times 10^{-16}$ Scm[-1] [31].

As for comparison, we focused on the equimolar four-component oxide $Co_{0.25}Ni_{0.25}Cu_{0.25}Zn_{0.25}O$ (CNCZ): it is mostly equivalent to the parent compound Mg-CNCZ, where the individual constituent MgO was removed from the mixing procedure.

Mg-CNCZ and CNCZ samples, studied in this work, have been synthesized by the group of P. Ghigna at University of Pavia (Italy) with the Sol-Gel based Pechini method [32], followed by thermal treatment at 1000°C and by quenching in air. Since the CNCZ sample has less constituent elements than Mg-CNCZ, we expect the configurational disorder to be smaller: indeed, from equation 1.4 one has that $\Delta S_{config} = R \ln 5 = 1.61R$ for Mg-CNCZ and $\Delta S_{config} = R \ln 4 = 1.39R$ for CNCZ, as also reported in Fig. 1.2, which classifies them as HEO and MEO, respectively.

MgO, CoO and NiO naturally adopt a rock-salt structure [33–37], while CuO and ZnO exhibit tenorite and wurtzite structure, respectively [37–39], therefore contributing with a positive enthalpic contribution to the variation of the Gibbs free energy in the transition to the single-phase rock-salt structure. Indeed, for the purpose of adapting to an overall rock-salt structure, Cu and Zn atoms are forced to modify their local environment; more precisely, interatomic Cu-O and Zn-O distances and bond directions are forced to change, and this process demands a certain amount of energy. That said, a quantification of the energy associated to the multi-phase to single-phase transition can be done assuming that the variation of enthalpy in the $CuO_{tenorite} \rightarrow CuO_{rock-salt}$ transition and in the $ZnO_{wurtzite} \rightarrow ZnO_{rock-salt}$ transition can be approximated by estimates of Gibbs free energy variations [10], as in the following: according to Ref. [40] and Ref. [41], $\Delta H_{f,CuO} \approx \Delta G_{CuO} = 22$ kJmol[-1] is the CuO transition free energy from tenorite to rock-salt and $\Delta H_{f,ZnO} \approx \Delta G_{ZnO} = 25$ kJmol[-1] is the equivalent estimate for the ZnO transition from wurtzite to rock-salt; the total variation of the Gibbs free energy during the transition for Mg-CNCZ is

$$\Delta H_{f,Mg-CNCZ} = 0.2\Delta H_{f,CuO} + 0.2\Delta H_{f,ZnO} = 9.4 \text{ kJmol}^{-1} \tag{1.7}$$

where $0.2 = \frac{1}{5}$ accounts for the molar fraction of CuO and ZnO in the Mg-CNCZ sample.

The same calculation can be applied to the four-component oxide, taking into account that each of the parent oxides has a molar fraction equal to $0.25 = \frac{1}{4}$

$$\Delta H_{f,CNCZ} = 0.25\Delta H_{f,CuO} + 0.25\Delta H_{f,ZnO} = 11.75 \text{ kJmol}^{-1}. \tag{1.8}$$

As expected, the enthalpy of formation is positive for both systems, and is larger for the four-component oxide because there is a larger probability of finding an atomic site in the metal cation sub-lattice occupied by Cu or Zn.

From these estimates, a quantitative prediction of the lower boundary to the transition temperature $T_c$ can be provided:

$$\begin{aligned}
T_{c,Mg-CNCZ} &> \frac{0.2\Delta H_{f,CuO} + 0.2\Delta H_{f,ZnO}}{R \ln 5} = 429 \text{ °C} \\
T_{c,CNCZ} &> \frac{0.25\Delta H_{f,CuO} + 0.25\Delta H_{f,ZnO}}{R \ln 4} = 746 \text{ °C}
\end{aligned} \tag{1.9}$$

Due to the smaller number of constituents, the four-component oxide requires larger temperatures to overcome the enthalpic cost of the structural transition compared to Mg-CNCZ, in agreement with experimental observations. However, these calculations underestimate the experimental critical temperatures, since Mg-CNCZ stabilizes in a single phase at 875 °C and CNCZ is expected to require even higher temperatures [10]. Clearly, the above thermodynamic arguments are approximate and further entropic and/or enthalpic terms must be included in this picture. The mismatch might be partially explained by the fact that this simple model overestimates the configurational order attributed to these materials [8]: indeed, configurational entropy suffers from reductions with respect to the ideal scenario captured by equation 1.4. Specifically, clustering and short-range ordering may be responsible for departures from an ideal random distribution of metal cations throughout the crystal lattice, reducing configurational disorder. Clustering happens when cations of the same chemical species prefer to be surrounded by first-neighbours either of different or same species, i.e., when a preferential short-range chemical bonding is present. A 2-D simple model visualizing an example of clustering in a 2-components metal oxide is shown in panel (b) of Fig. 1.5: the oxygen sub-lattice is represented by the ordered arrangement of grey spheres; blue and light-blue spheres model metal cations and complete the full rock-salt structure. Even though the disordered state corresponds to a maximum of the configurational entropy, the clustered state might be close in energy competition and be kinetically preferred during the quenching procedure. This is why optimized quenching protocols play a major role in preventing the formation of clusters.
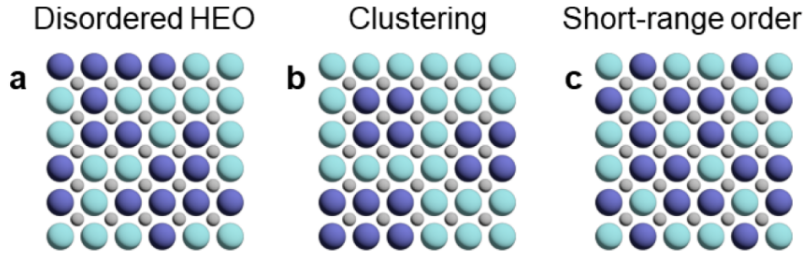
Figure 1.5: (a) Perfect random distribution of metal cations in the metal FCC sub-lattice, represented by blue and light-blue spheres. (b) Presence of clustering reduces the system entropy. (c) Example of short-range order arising in the sample. Figure taken from Solveig S. Aamlid et al. [8].

An example of clustering was observed on $(Ce_{0.2}Zr_{0.2}Hf_{0.2}Sn_{0.2}Ti_{0.2})O_2$, an oxide with fluorite structure showing elemental segregation of Ce [17]. Panel (c) visualizes short-range ordering on a nanometric length scale, which arises from electrostatic forces and disrupt the ideal lattice disorder. Unfortunately, short-range ordered clusters are challenging to observe [42, 43].

An additional element to be taken into account is the presence of a spontaneous local distortion of the octahedral unit, which reduces the symmetry of the HEO system, namely Jahn-Teller effect. It splits degenerate states as a consequence of symmetry breaking, increasing the degree of disorder associated to the compound. This effect will be deeply discussed in section 2.1.1. It is not yet clear if Jahn-Teller distortions have a sizeable influence on the critical temperature estimates and quantitative evaluations of its contribution to the entropic and enthalpic terms are missing in the literature, despite a number of paper report on its experimental observation. The primary aim of our work is to provide an estimate of the energy associated to the Jahn-Teller distortion in Mg-CNCZ and CNCZ.

## 1.3.  Jahn-Teller distortions in Mg-CNCZ

At the beginning of section 1.2 we introduced that in the family of rock-salt HEOs the local coordination leads to the formation of octahedral complexes, as depicted in Fig. 1.3. Consequently, we may expect that the local environment of metal cations in HEOs undergoes Jahn-Teller (JT) distortions.

A number of articles among the HEO literature report both the theoretical prediction [44–46] and the experimental observation [18, 19] of a certain degree of structural disorder, which adds up to the intrinsic configurational disorder of these materials. Extended X-ray Absorption Fine Structure (EXAFS) is a useful tool to verify the distortion of the local atomic structure. Indeed, the peaks in Fourier-Transformed EXAFS spectra contain information on the radial distribution of neighbours to the probed cation. Rost et al. [18] published an analysis of EXAFS spectra retrieved from rock-salt $Mg_{0.2}Co_{0.2}Ni_{0.2}Cu_{0.2}Zn_{0.2}O$, as shown in Fig. 1.6. The Mg cation was omitted from the experiment "due to the energetic limitations of the beamline".
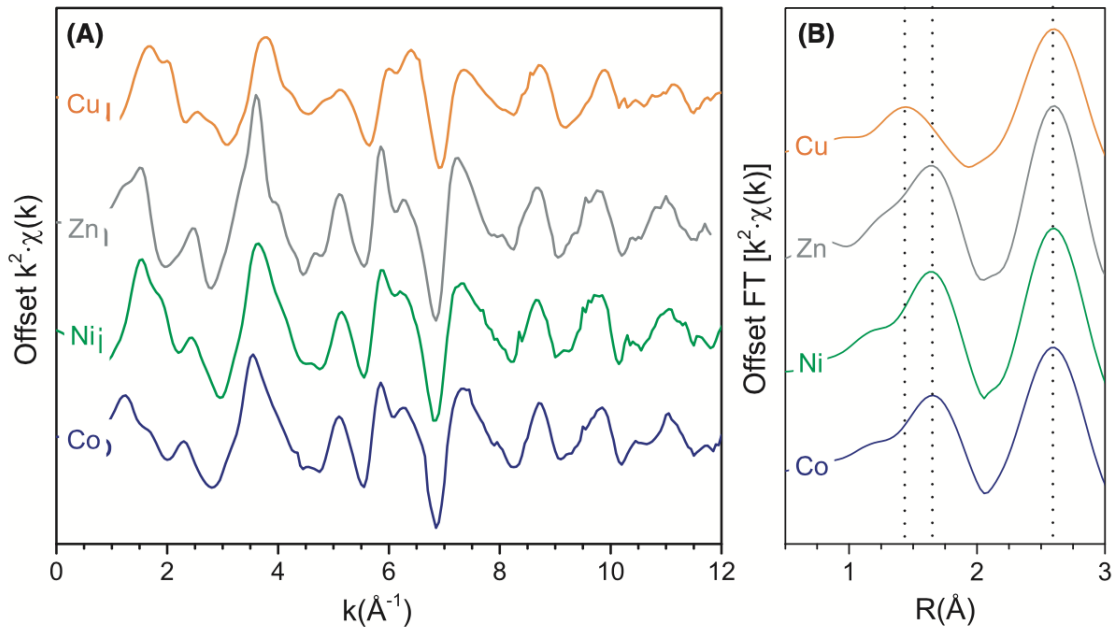


Figure 1.6: $k^2\chi(k)$ EXAFS functions for cations of NiO, CoO, CuO, and ZnO precursor oxides are shown in panel (A). Panel (B) reports $\chi(R)$ i.e. the FT of the EXAFS function [18].

$\chi(k)$ is the EXAFS signal properly treated, and its Fourier transform, $\chi(R)$, is the radial distribution function. $R$ is the radial distance from the probed ion, not to be confused with the universal gas constant introduced in section 1.1. From $\chi(R)$ we observe that

the second peak, referring to the radial position of the next nearest neighbours (cations), is found at roughly 2.6 Å in all cases: the cation-cation distance distribution does not depend on the particular cations involved and is centered at the same value because of the cubic symmetry of the rock-salt structure. The first peak, instead, is a measure of the metal-anion distance: it is broader and shifted towards smaller $R$ for Cu than for other cations. In essence, the EXAFS study reveal a near-ideal FCC cation sub-lattice interpenetrated to a locally distorted anion sub-lattice, especially around $Cu^{2+}$ sites. The same group performed also a more quantitative analysis on EXAFS spectra by fitting the two coordination shell peaks of the $\chi(R)$ function, retrieving estimates of cation-oxygen distances. They report a Zn-O bond length of $2.078 \pm 0.009$ Å, a Co-O bond length of $2.089 \pm 0.009$ Å and a Ni-O bond length of $2.084 \pm 0.005$ Å, found in an ideal local octahedral environment. Furthermore, they obtained a bimodal distribution of Cu-O legths: 4 in-plane Cu-O bonds of length $1.993 \pm 0.007$ Å and two out-of-plane Cu-O bonds of length $2.22 \pm 0.02$ Å, consistently with a JT-like tetragonal elongation of the octahedral complex.

Further evidences of structural distortion in HEOs come from other techniques, such as X-ray Diffraction (XRD) or Electron Paramagnetic Resonance (EPR) studies [47]. Berardan et al. exploited these techniques to prove that the amount of tetragonal distortion depends on Cu stoichiometry in Mg-CNCZ. For the sake of brevity, we only report the XRD patterns for 7 Mg-CNCZ samples with increasing Cu molar fraction (Fig. 1.7).
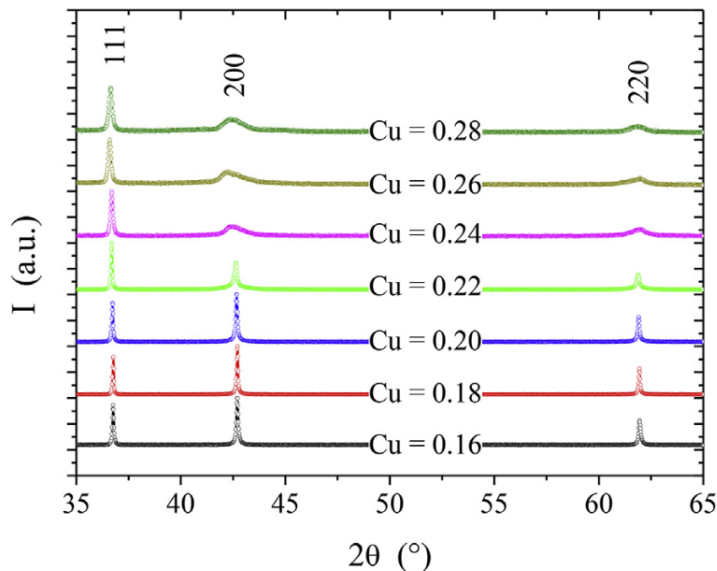


Figure 1.7: X-ray diffraction patterns for $Mg_{1-x}Co_{1-x}Ni_{1-x}Zn_{1-x}Cu_xO$, with $x$ spanning from 0.16 to 0.28 [47].

The (111), (200) and (220) reflections show well defined peaks for a Cu molar fraction smaller than 0.2. When $x > 0.2$, the (111) peak remains independent on the copper fraction, while the (200) peak and the (220) suffer from a strong intensity reduction and an evident broadening, revealing an increasing departure of the material from the ideal rock-salt structure. The opportunity of tuning the degree of distortion by controlling the Cu molar fraction becomes interesting if we consider that functional properties depend on the crystal structure: the distortion can be engineered to optimize the resistivity and the dielectric constant of these materials [47].

From the discussion above, it seems clear that Mg-CNCZ and possibly other HEOs are affected by JT distortions. However, associated bond length variations are never translated into corresponding energy changes that might have an impact on the thermodynamic considerations we made before. In particular, JT distortions might diminish the enthalpy of formation associated to the transition of CuO and ZnO from the tenorite and the wurtzite to the rock-salt structure, as well as increase the configurational entropy associated to the JT distortions along different axes. In this context, we believe that RIXS could give a useful insight, because it directly measures the energies at play in locally-distorted octahedral complexes.

## 1.4.    Magnetic properties of Mg-CNCZ

The strong interest in HEOs does not pertain only to structural or configurational disorder: in the recent past the scientific community focused its attention on the investigation of the magnetic behaviour of this family of oxides, revealing some interesting properties. Even though several studies on HEOs with a variety of crystalline structures are available [48–50], we restrict our review on the prototypical Mg-CNCZ compound.

In 2019, Junjie Zhang et al. [51] reported the first use of neutron powder diffraction to explore the magnetic structure of the Mg-CNCZ oxide, together with other complementary techniques (Inelastic Neutron Diffraction and measurements of heat capacity and magnetic susceptibility) with unexpected results. Indeed, intuitively, a structurally disordered compound consisting of 40% of non-magnetic ions is expected to display a spin-glass state [52]; nevertheless, this naive expectation was disproved by the experimental evidence of long-range magnetic ordering with propagation vector $(\frac{1}{2}\frac{1}{2}\frac{1}{2})$. The magnetic structure is driven by the anti-ferromagnetic (AFM) couplings between (111) planes of the cation sub-lattice, while magnetic moments in each (111) plane exhibit ferromagnetic ordering. A visual representation of the magnetic structure is proposed in Fig. 1.8. The magnetic structure is analogous to that of CoO [53] and NiO [54].
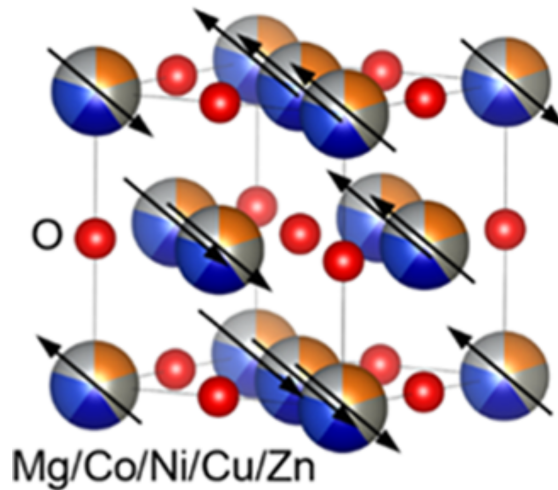


Figure 1.8: Magnetic structure of the $Mg_{0.2}Co_{0.2}Ni_{0.2}Cu_{0.2}Zn_{0.2}O$ compound. The $O^{2-}$ sub-lattice does not contribute to any magnetic property, since $O^{2-}$ ions are not magnetic. (111) planes of the cation sub-lattice exhibit AFM coupling. In-plane spins, instead, remain parallel [51].

The fact that Mg-CNCZ undergoes a transition to a long-range ordered magnetic phase has been investigated theoretically: Zs. Rák and D.W. Brenner exploited first-principles

methods in combination with Monte Carlo (MC) simulations [55] and reproduce the correct magnetic structure with average magnetic interactions between nearest neighbours and next-nearest neighbours of 0.18 meV and -2.72 meV, respectively, where the negative sign accounts for antiferromagnetic coupling. Magnetic susceptibility measurements and temperature-dependent neutron diffraction patterns reveal a Néel temperature $T_N$ in the $110-120$ K range [51, 56]. As shown in Fig. 1.9, we report the temperature dependence of magnetic susceptibility for the 5-component compound measured by Zhang et al. A clear cusp is observed at 113 K, suggesting the occurrence of a paramagnetic-antiferromagnetic phase transition.
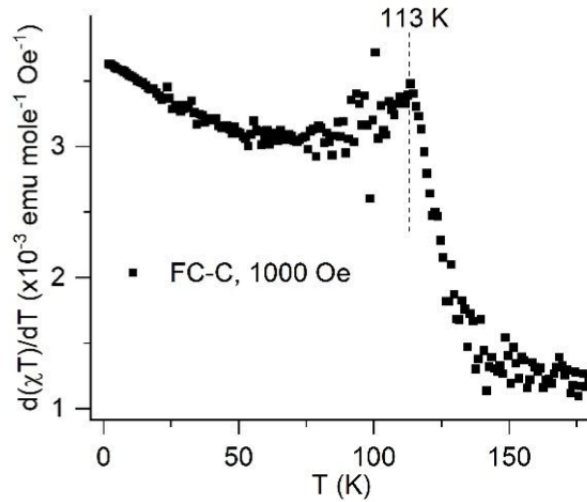


Figure 1.9: Magnetic susceptibility data as a function of temperature, in presence of a 0.1 T magnetic field. Measurements were performed in the cooling regime (FC-C) [51].

Now we examine another phenomenological aspect concerning the magnetism of those HEOs differing in the content of magnetic ions. The samples of our interest fall into this category since they show a distinct magnetic ion fraction: 40% of cations in Mg-CNCZ are non-magnetic, while the fraction decreases to 25% in CNCZ. Jimenez-Segura et al. [56] published a direct comparison of magnetic susceptibility $\chi(T)$ measured on a variety of samples prepared with a variable content of magnetic ions. Samples were obtained by replacing one magnetic (or non-magnetic) cation of the parent compound Mg-CNCZ with a 1:1 mixture of non-magnetic monovalent and trivalent cations, such as $Li^+$ and $Ga^{3+}$. All samples containing three magnetic cations display a distribution of Néel temperatures in the $100-150$ K range, in agreement with the Néel temperature of the parent compound. HEO samples possessing only two magnetic ions exhibit a much smaller Néel temperature

of about 25 K. This phenomenology captures the strengthening of long-range magnetic ordering with increasing fraction of magnetic ions. The trend was predicted also by Monte Carlo simulations [55], where the Néel temperature of the long-range magnetic phase was calculated as a function of the molar fraction of the non-magnetic cations.
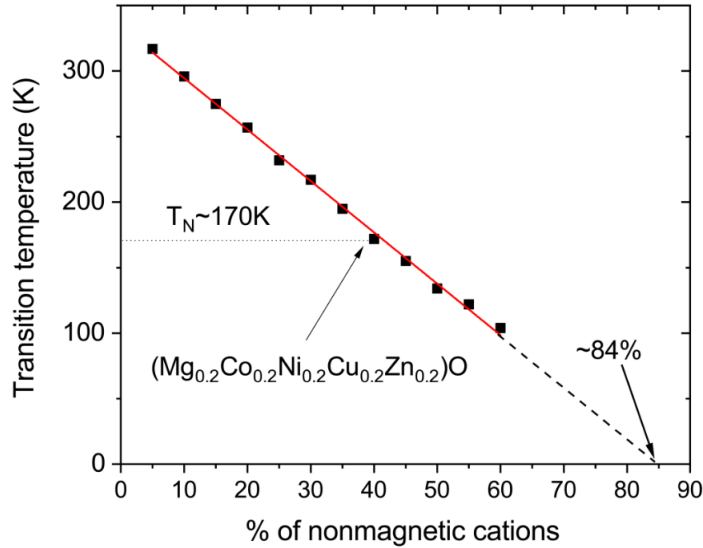


Figure 1.10: Simulated transition temperatures of the Mg-CNCZ compound as a function of the fraction of non-magnetic cations. The red line highlights a linear relationship [55].

As depicted in Fig. 1.10, calculations led to a linear relationship between $T_N$ and the magnetic ion content. Additionally, the computed linear dependence predicts that for a fraction of non-magnetic cations larger than 84% the compound becomes a paramagnet. We notice that the predicted Néel temperature for the equimolar cation ratio oxide (170 K) is 40% larger than the experimental value.

By virtue of this theoretical result, the ability to tune the phase transition temperature by adjusting the fraction of magnetic cations turns into a concrete possibility.

# 2 | Resonant Inelastic X-ray Scattering from $Cu^{2+}$

The goal of this chapter is to provide the theoretical background to fully understand the presentation and the discussion of the experimental results obtained performing Resonant Inelastic X-ray Scattering on the HEO powder samples. The chapter is divided in 3 sections: at first, the electronic properties of $Cu^{2+}$ and its octahedral environment will be addressed; after that, an overview of the RIXS technique, together with cross section calculations, is proposed; finally, a brief description of the employed experimental setup is reported.

## 2.1. Electronic structure of $Cu^{2+}$

In the following sections an introduction to some fundamental concepts regarding Crystal Field theory, Jahn-Teller effects and Ligand Field theory is given, together with an explanation of their importance in the framework of HEOs. In conclusion, a brief discussion on spin-orbit coupling effects on $3d$ states will be reported. Since we performed RIXS experiments at the $Cu^{2+}$ $L_3$ absorption edge, these theories will be presented with the aim to specifically describe the electronic structure of the $Cu^{2+}$ ion. It is known that $Cu^{2+}$ cations in octahedral complexes have a $3d^9$ configuration [57], hence one electron is left unpaired in the highest energy level; the electronic properties are well described by the physics of a one-hole system and electron-electron interaction phenomena are neglected.

### 2.1.1. Crystal Field theory and Jahn-Teller effect

Crystal Field theory (CF) describes the breaking of degeneracies of electronic states due to the electric field produced by the ligand ions. Typical systems properly modeled by this theory are octahedral complexes of transition metals, where a transition metal cation is surrounded by six anionic ligands at the vertices of an octahedron. The octahedral symmetry splits the $d$ orbitals of transition metals in two separate sets of degenerate

levels, namely $e_g$ ($d_{x^2-y^2}$ and $d_{3z^2-r^2}$) and $t_{2g}$ ($d_{xy}$, $d_{xz}$ and $d_{yz}$) orbitals, that would be fully degenerate in metal cations with spherical symmetry. On top of this, the system may also suffer from a spontaneous mechanism known as Jahn-Teller (JT) effect, or Jahn-Teller distortion, occurring in systems characterized by electronic degeneracy. The JT effect consists in the removal of the electronic degeneracy as a direct consequence of a symmetry-breaking local distortion, which provides a reduction of the overall energy. A well studied example is the six-coordinated Cu$^{2+}$ complex, where tetragonal compression or elongation of the octahedral cage is responsible for further splitting both $e_g$ and $t_{2g}$ states.
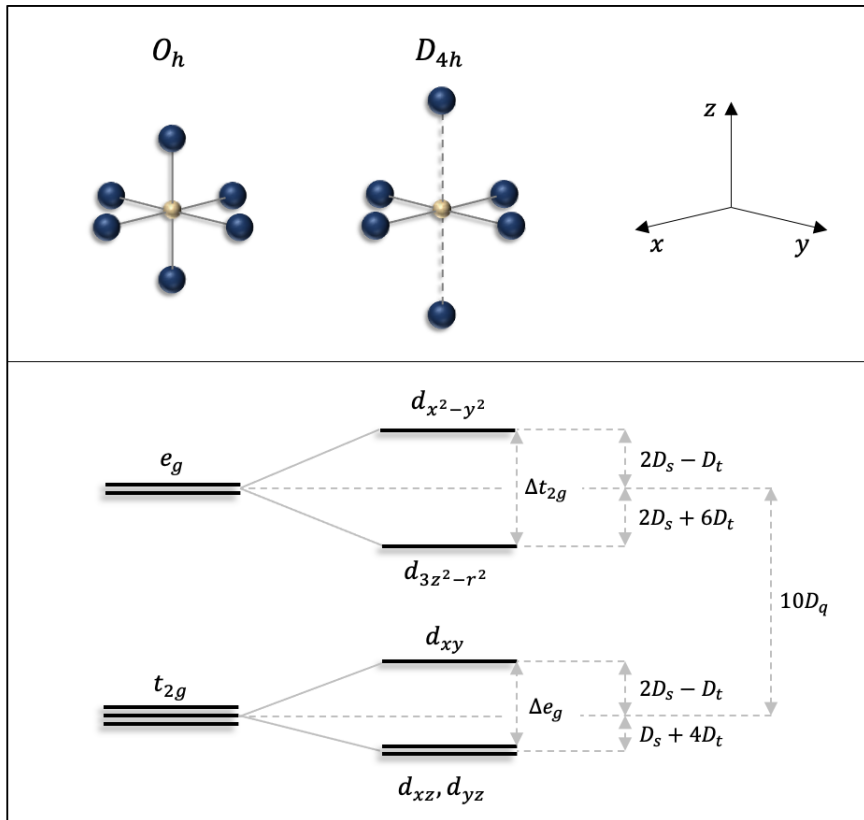


Figure 2.1: Electronic energy diagram of $3d$ orbitals in Cu$^{2+}$ without distortion ($O_h$ symmetry) and with tetragonal elongation ($D_{4h}$ symmetry).

Figure 2.1 shows the electronic energy diagram in an octahedral complex. In absence of distortion the symmetry is cubic: the cation and the ligands form a perfect octahedron ($Oh$ space group), since all cation-ligand interatomic distances are equivalent. As already introduced, $e_g$ and $t_{2g}$ states show 4-fold and 6-fold degeneracy, respectively. If either compression or elongation is present, the cubic symmetry is reduced to a tetragonal symmetry ($D_{4h}$ space group). Assuming that elongation occurs along the $z$ axis (as shown in Fig.

2.1), the metal cation $d_{3z^2-r^2}$ orbital undergoes a strong energy stabilization: a $3d$ electron suffers from a smaller Coulomb repulsion when occupying the $d_{3z^2-r^2}$ orbital rather than orbitals laying on the $xy$ plane, since along the $z$ direction non-bonding electrons in the apical anions are further away. The same rationale is used in case of a JT compression and leads to an energy stabilization of the $d_{x^2-y^2}$ state. This is the motivation under the removal of degeneracy of $e_g$ states. Regarding $t_{2g}$ states, a similar result is expected. $d_{xz}$ and $d_{yz}$ orbitals are energy-stabilized by tetragonal elongation and undergo splitting from the $d_{xy}$ state. One can notice that $d_{xz}$ and $d_{yz}$ orbitals are degenerate even in tetragonal symmetry. Looking at Fig. 2.1, we introduce $D_q$, $D_s$ and $D_t$ parameters: they are effective crystal field parameters and are exploited to quantify the amount of tetragonal distortion. Their values is determined by comparison with experimental results and strongly depend on the material [58]. $10D_q$ provides the energy splitting between the $e_g$ levels and the $t_{2g}$ levels. $2D_s - D_t$ and $2D_s + 6D_t$ identify the position of $d_{x^2-y^2}$ and $d_{3z^2-r^2}$ with respect to $e_g$. Similarly $2D_s - D_t$ and $D_s + 4D_t$ give the positions of $d_{xy}$ and $d_{xz}$ ($d_{yz}$) orbitals with respect to the $t_{2g}$ energy reference. Except for a common shift, $d$ energy levels are given by [59]

$$
\begin{aligned}
E_{x^2-y^2} &= 6D_q + 2D_s - D_t \\
E_{3z^2-r^2} &= 6D_q - 2D_s - 6D_t \\
E_{xy} &= -4D_q + 2D_s - D_t \\
E_{xz} = E_{yz} &= -4D_q - D_s + 4D_t
\end{aligned}
\tag{2.1}
$$

such that

$$
\begin{aligned}
\Delta e_g &= E_{x^2-y^2} - E_{3z^2-r^2} = 4D_s + 5D_t \\
\Delta t_{2g} &= E_{xy} - E_{xz,yz} = 3D_s - 5D_t.
\end{aligned}
\tag{2.2}
$$

### 2.1.2. Fundamentals of Ligand Field theory

The following section provides some fundamental concepts regarding Ligand Field (LF) theory, which is instrumental in the interpretation of our experimental results. The LF model applies the theory of molecular orbitals to transition metal complexes with the aim to refine the CF picture of the electronic structure of the system. Indeed, while in CF theory ligands are only responsible for the electrostatic forces that generate the crystal field, LF theory takes into account the effects of possible hybridization of the ligand orbitals with the transition metal orbitals. In octahedral complexes, the transition metal $d$ orbitals superimpose to the surrounding $p$ orbitals of $O^{2-}$ ions placed at the vertices of the octahedra. The resulting molecular orbitals are mathematically described by means of linear combination of atomic Cu $d$ and O $p$ orbitals. In this picture, metal and ligand

electrons are delocalized over the resulting molecular bonds.

The electronic energy diagram can be obtained by solving the eigenvalue equation for the Hamiltonian $\mathcal{H}_{MO}$ of the metal-O system. Assuming the simple case of a bi-atomic molecule, the basis set is formed by 5 $d$ orbitals ($d_{x^2-y^2}$, $d_{3z^2-r^2}$, $d_{xy}$, $d_{xz}$ and $d_{yz}$) and 3 ligand $p$ orbitals ($p_x$, $p_y$ and $p_z$) and the corresponding Hilbert space is 8-dimensional. Specifically, the Hamiltonian can be written as

$$
\mathcal{H}_{MO} =
\begin{array}{cccccccc}
d_{x^2-y^2} & d_{3z^2-r^2} & d_{xy} & d_{xz} & d_{yz} & p_x & p_y & p_z \\
\end{array}
$$

$$
\mathcal{H}_{MO} =
\left(
\begin{array}{cccccccc}
E_{x^2-y^2} & 0 & 0 & 0 & 0 & \sqrt{\frac{3}{2}}t_\sigma & 0 & 0 \\
0 & E_{3z^2-r^2} & 0 & 0 & 0 & -\frac{1}{2}t_\sigma & 0 & 0 \\
0 & 0 & E_{xy} & 0 & 0 & 0 & t_\pi & 0 \\
0 & 0 & 0 & E_{xz} & 0 & 0 & 0 & t_\pi \\
0 & 0 & 0 & 0 & E_{yz} & 0 & 0 & 0 \\
\sqrt{\frac{3}{2}}t_\sigma & -\frac{1}{2}t_\sigma & 0 & 0 & 0 & \Delta & 0 & 0 \\
0 & 0 & t_\pi & 0 & 0 & 0 & \Delta & 0 \\
0 & 0 & 0 & t_\pi & 0 & 0 & 0 & \Delta \\
\end{array}
\right)
\begin{array}{l}
d_{x^2-y^2} \\
d_{3z^2-r^2} \\
d_{xy} \\
d_{xz} \\
d_{yz} \\
p_x \\
p_y \\
p_z \\
\end{array}
$$

Diagonal terms represent the expectation values of the energy of unperturbed atomic orbitals. This is why we found the expression of energy for $d$ levels in the diagonal of the 5x5 sub-matrix (see equations 2.1 and 2.2). From now on, we will refer to this sub-matrix as $\mathcal{H}_{CF}$. Instead, $\Delta$ is the expectation value of the energy of $p$ orbitals relative to the energy of the hole ground state $d_{x^2-y^2}$, within the assumption that $p_x$, $p_y$ and $p_z$ are degenerate. Off-diagonal terms are the Slater-Koster overlap integrals $t$ calculated between any couple of atomic orbitals within the basis set. We must specify the meaning of $\sigma$ and $\pi$ labels: they represent the character of the bond resulting from the superposition of $p$ and $d$ orbitals. For instance, the off-diagonal term $\sqrt{\frac{3}{2}}t_\sigma$ ($1^{st}$ row, $6^{th}$ column) represents the $\sigma$-like overlap integral between the transition metal $d_{x^2-y^2}$ state and the oxygen $p_x$ state. The factor $\sqrt{\frac{3}{2}}$ accounts for the relative orientations of metal and ligand orbitals. A detailed explanation can be found in Ref. [60].

In more realistic systems, such as octahedral cages in transition metal oxides, the cation $d$ orbitals superimpose to $p$ orbitals of all 6 surrounding O$^{2-}$ anions. Consequently, an extension of the previous picture must be introduced. The Hamiltonian of the whole metal-oxide octahedral complex, named $\mathcal{H}_{MO_6}$, is a 23x23 matrix since the basis set consists of 5 $d$ orbitals and 18 $p$ orbitals (3 for each anion). The full expression is reported in Appendix A.3. The Hamiltonian includes the effects of JT distortion. Along the direction of the apical ligands, orbital overlaps are either enhanced or weakened by compression or elongation, respectively. As a consequence, we introduced distinct Slater-Koster overlap

integrals, $t_{\sigma,apical}$ and $t_{\pi,apical}$, in the Hamiltonian entries involving $p$ orbitals of the apical anions. They are obtained by multiplying $t_\sigma$ and $t_\pi$ by a factor $F$: $F > 1$ implies $t_{\sigma,apical}(t_{\pi,apical}) > t_\sigma(t_\pi)$ and describes the situation of compresses tetragonal distortion , while $F < 1$ implies $t_{\sigma,apical}(t_{\pi,apical}) < t_\sigma(t_\pi)$ and describes elongated tetragonal distortion.

By calculating the eigenvalues of $\mathcal{H}_{MO_6}$ one is able to build the energy diagram of the whole octahedral complex. Fig. 2.2 reports an example of calculated energies for hybridized molecular states.
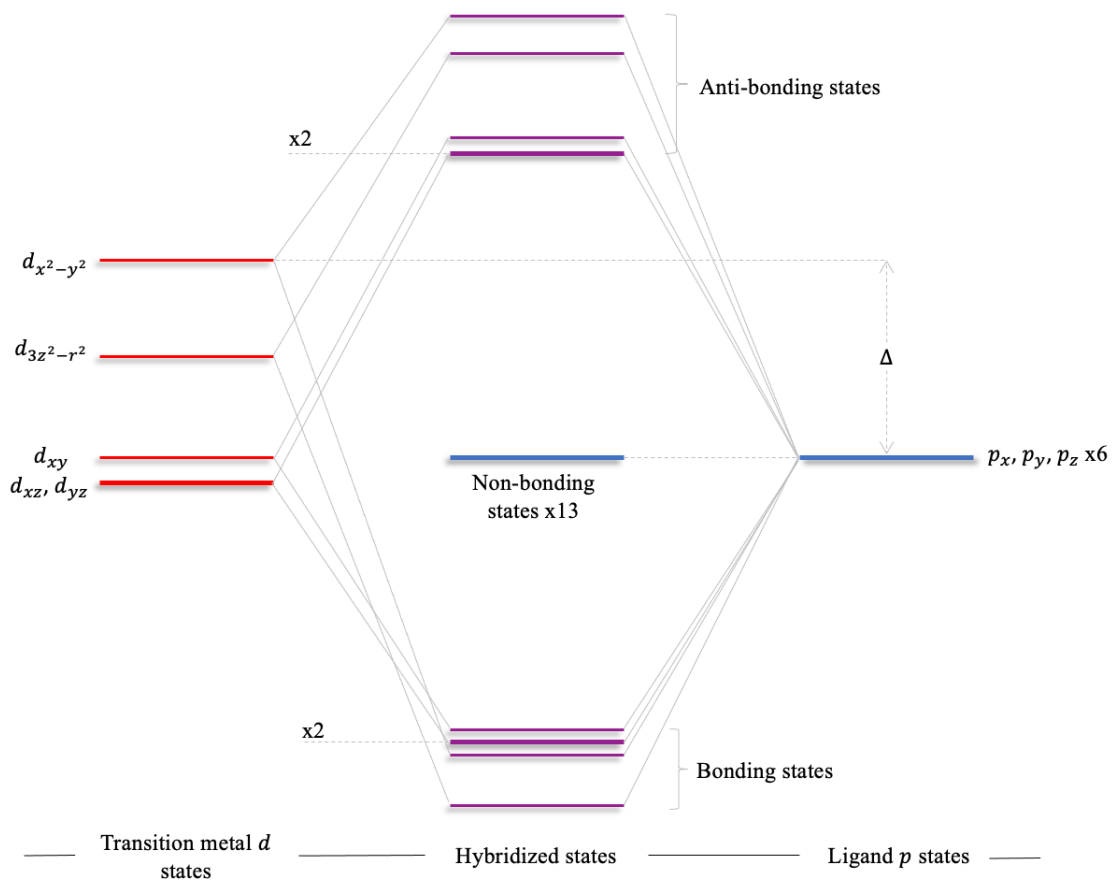


Figure 2.2: Calculated molecular energy levels of an octahedral complex system. The color of each state is related to its symmetry character: red = $d$ states, blue = $p$ states, shades of purple = linear combination of $p$ and $d$ states.

The effective crystal field parameters for transition metal $d$ states were assumed to be $D_q = 0.1$ eV, $\Delta e_g = 0.5$ eV and $\Delta t_{2g} = 0.15$ eV. Moreover, the energy difference $\Delta$ between the 18-fold degenerate $p$ states and the transition metal $d_{x^2-y^2}$ state was set to be -1 eV. Hybridized states are found in the central section of the picture. The five least energetic levels are bonding states, while the five most energetic orbitals are anti-bonding

states. 13 out of 18 anionic $p$ states are not involved in any overlap mechanism and are non-bonding states.

In principle, by optimizing the parameters to match experimental energies, one should be able to retrieve a quantitative estimate of the CF and LF interactions. However, in the present work we will extract quantitative CF parameters from the analysis of $dd$ excitations and use LF theory to qualitatively describe charge-transfer excitations.


### 2.1.3.   The effect of spin-orbit coupling

A more refined description of the electronic properties of the transition metal should also include the effects of spin-orbit coupling. In the following, we adopt the CF description of Cu electronic states: the electronic properties of the Cu$^{2+}$ ion are related solely to the set of $3d$ states listed in Tab. 2.1, which are eigenstates of the CF Hamiltonian $\mathcal{H}_{CF}$. Actually, in the presence of spin-orbit interaction, $3d$ states are not the eigenstates of the system and spin is no longer a good quantum number. The Hamiltonian must be corrected to include the spin-orbit interaction. We write

$$\mathcal{H}_{tot} = \mathcal{H}_{CF} + \mathcal{H}_{SO}, \tag{2.3}$$

with

$$\mathcal{H}_{SO} = \lambda \left[ \frac{(L_+ S_- + L_- S_+)}{2} + L_z S_z \right], \tag{2.4}$$

where $\lambda$ is the strength of the spin-orbit interaction, $L_z$ and $S_z$ are the $z$ components of the orbital angular momentum operator $L$ and spin angular momentum operator $S$, respectively, and $L_\pm$ and $S_\pm$ the corresponding ladder operators. If we rely on the matrix formalism for the representation of the operators, the eigenvalue equation for $\mathcal{H}_{tot}$ is written as

$$\mathcal{H}_{tot}\mathcal{T}_{SO} = \Lambda \mathcal{T}_{SO}, \tag{2.5}$$

where the new eigenvectors are the column vectors of $\mathcal{T}_{SO}$. The eigenvalues, instead, are found on the diagonal of $\Lambda$. In $3d$ transition metal oxides the spin-orbit coupling (0.05 eV) is small compared to CF parameters ($\sim 1$ eV), and the effect of spin-orbit coupling is negligible, except for degenerate states. Indeed, the degeneracy of $d_{xz}$ and $d_{yz}$ states is removed and the final states are formed by their linear combination. We name them $d_-$

(lower in energy) and $d_+$ (higher in energy), and they are written as

$$
\left.\begin{array}{l} d_{xz,\downarrow} - id_{yz,\uparrow} \\ d_{yz,\downarrow} + id_{xz,\uparrow} \end{array}\right\} \quad d_- \\
\left.\begin{array}{l} d_{yz,\downarrow} - id_{xz,\uparrow} \\ d_{xz,\downarrow} + id_{yz,\uparrow} \end{array}\right\} \quad d_+
$$

$$(2.6)$$

## 2.2. Resonant Inelastic X-ray Scattering

In the present chapter a general review on Resonant Inelastic X-ray Scattering (RIXS) is provided. We will present the properties of the technique and its main features, acknowledging the reasons why RIXS is regarded as a powerful tool for the investigation of the electronic, magnetic and structural properties of a large variety of materials, including transition metal oxides. In the following, starting from the well-known Kramers-Heisenberg equation, we present the relevant steps in the calculation of the scattering cross section for a generic powder sample, in the framework of the single-ion model. In conclusion, a brief description of the set-up of the experiment carried out at the European Synchrotron Radiation Facility (ESRF) in Grenoble is reported.

### 2.2.1. General properties

Resonant Inelastic X-ray Scattering is a photon in-photon out spectroscopic technique able to probe elementary excitations in solid samples. It is a synchrotron-based technique: synchrotron radiation sources are indispensable to provide monochromatic and collimated x-ray light compatible with the RIXS scattering process. Nowadays several synchrotron radiation facilities have running RIXS endstations, such as ESRF (France) [61], Swiss Light Source (SLS, in Switzerland) [62], Diamond Light Source (DLS, in UK) [63], The National Synchrotron Light Source II (Brookhaven National Laboratory, USA) [64] and others.

RIXS is an example of light-matter interaction process: an incoming photon of energy $\hbar\omega_i$, momentum $\mathbf{k}_i$ and polarization state $\boldsymbol{\epsilon}_i$ is scattered out by a solid sample towards an arbitrary direction, acquiring - in the most general case - different energy $\hbar\omega_f$, momentum $\mathbf{k}_f$ and polarization state $\boldsymbol{\epsilon}_f$, that is the system might be left in an excited state. Indeed, the relevant physics captured by RIXS is infered by inelastic features, those features involving energy transfer from radiation to matter. Furthermore, RIXS is a resonant technique: the incoming photon energy is selectively chosen to match one of the atomic absorption edges of the probed atom, enhancing the probability of the scattering event. Many other relevant characteristics of RIXS can be mentioned [58, 65]:

- due to conservation rules, the momentum change of the photon implies that momentum is also transferred to the sample:

$$\hbar\mathbf{q} = \hbar\mathbf{k_i} - \hbar\mathbf{k_o} \tag{2.7}$$

$\mathbf{q}$ is the transferred momentum and is equal and opposite to the momentum change.

As a consequence, the **momentum dependence** of any elementary excitation can be measured, probing a variable portion of the 1$^{st}$ Brillouin Zone in the reciprocal space;

- the **neutrality** of the sample is conserved during the RIXS process. Indeed, being a photon in-photon out technique, no charge is expected to affect the overall sample charge balance;

- the x-ray penetration depth depends strongly on the photon energy. Despite this, RIXS is regarded as a **bulk-sensitive** technique: even in the soft x-ray spectral range the penetration depth reaches a few $\mu$m. The resulting advantage is the opportunity to explore the properties of a sample without worrying about the surface degree of contamination;

- light-matter interaction is sufficiently strong to **probe small samples**, even thin films. Big sample volumes are not a requirement of the technique;

- in-going photon energy tuning allows one to select the atomic species to probe, guaranteeing **element selectivity**. We only recall that all atomic absorption edges are dependent on their chemical environment. Consequently, RIXS is able to discriminate between chemically inequivalent atomic species i.e. with different oxidation states or coordination symmetries.

One of the main concerns of RIXS has always been energy resolution. A huge resolving power is required, due to the large difference between the energy scales of the source (keV) and of the desired resolution (tens of meV). However, state-of-the-art RIXS instrumentation has made a gigantic step forward: we mention the ID32 soft x-ray beamline at ESRF, which is able to discriminate features less than 50 meV apart at the $L_3$ absorption edge of Cu (931 eV) by means of a resolving power up to 30000 [61]. A typical RIXS spectrum is visualized in Fig. 2.3 for a generic condensed matter system. The spectrum reports the detected x-ray scattering intensity as a function of the photon energy loss i.e. energy transferred to the sample. The main inelastic features are found in an energy scale which ranges from tens of meV (magnetic or phonon excitations) to tens of eV (charge-transfer excitations). Charge-Transfer (CT) excitations involve the transfer of electrons from one ion to another of different chemical species. To give an example, in transition metal oxides the incoming photon provides sufficient energy to transfer an electron from the probed metal cation to one of the $O^{2-}$ anions found in the local environment. The required energy depends on the inter-ionic Coulomb repulsion.
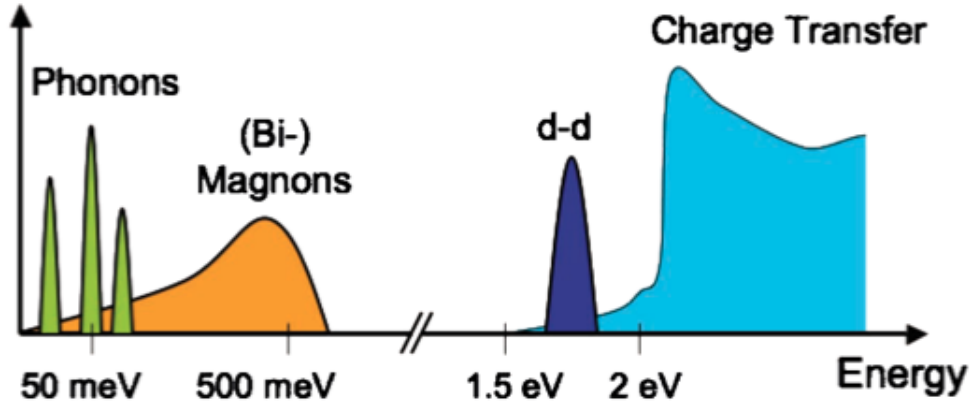
Figure 2.3: An exemplifying depiction of all accessible inelastic features in a RIXS experiment [66].

In systems exhibiting an orbital degree of freedom, orbital excitations are observed. They consist in tranfers of valence electrons between two orbitals of the same ion. In transition metal oxides valence electrons are found in $d$ orbitals, hence the label "$dd$ excitations". Therefore, in principle, a RIXS spectrum contains the information of the position of all $d$ energy levels. Via CF theory, we are able to predict the energy splitting between $d$ orbitals and, in turn, the energy positions of $dd$ peaks: by comparing them with RIXS spectra, we have access to electronic and structural properties of the sample, such as the local symmetry of transition metal ions. Just by looking at $dd$ excitations, it is possible to infere the degree of tetragonal distortion in the ionic local environment, knowing that JT effects affect the position of $d$ levels (see paragraph 2.1.1). Relevant studies can be found proving the reliability of the technique in probing the electronic structure of materials [67–69].

The low energy part of the spectrum is dominated by magnons and phonons. Magnetic peaks are found when probing compounds containing magnetic ions, so ions possessing partially filled outer shells. Their magnetic moments interact with each other to realize an ordered magnetic structure, whose collective excitations are magnons and can be probed by RIXS. Since **q**-resolved measurements of any excitation are accessible, RIXS gives the opportunity to measure magnonic dispersions for a variety of samples, such as transition metal oxides or cuprate superconductors [54, 70, 71] and similarly for phonons, collective excitations of the ions in the lattice.

We conclude by mentioning that RIXS detectors collect also scattered photons with zero energy loss, leading to the formation of an elastic feature. The elastic peak is regarded as a potential obstacle in the interpretation of RIXS spectra, since it is sometimes stronger than the neighbouring low energy excitations. In this sense, the recent improvement in

the instrumentation performance in terms of energy resolution was crucial in the discrimination of low energy features from elastic peak tails.

## 2.2.2.    The RIXS process

The scattering process in a RIXS event is schematized in Fig. 2.4. An x-ray photon with momentum $\mathbf{k}_i$ and energy $\hbar\omega_{\mathbf{k}_i}$ promotes a core electron to an empty state in the valence band, leaving a hole in the core level. We recall that the probability of this event is strongly enhanced by matching the energy of the in-going photon to the absorption edge of the system. Since the core levels are not fully occupied, energy is not minimized and this intermediate state is unstable: an electron (not necessarily the excited core electron) relaxes from a valence band state - either above or below the Fermi level - to the core hole, emitting a photon with momentum $\mathbf{k}_o$ and energy $\hbar\omega_{\mathbf{k}_o}$. The net result is the excitation of an electron-hole pair in the valence band. The lifetime of the intermediate state is set by radiative electron-hole recombination times (a few fs), while the energy $E$ transferred to the system i.e. the energy of the final state is determined by the difference between the in-going photon energy $\hbar\omega_{\mathbf{k}_i}$ and the out-going photon energy $\hbar\omega_{\mathbf{k}_o}$, following the energy conservation rule

$$E = \hbar\omega_{\mathbf{k}_i} - \hbar\omega_{\mathbf{k}_o}. \tag{2.8}$$

By virtue of the 2-steps nature of the process, RIXS is referred to as a **second order process**.

Actually, what we have described is a process called *direct* RIXS, which is less complicated than the counterpart *indirect* RIXS. Indirect RIXS will not be part of this thesis work.
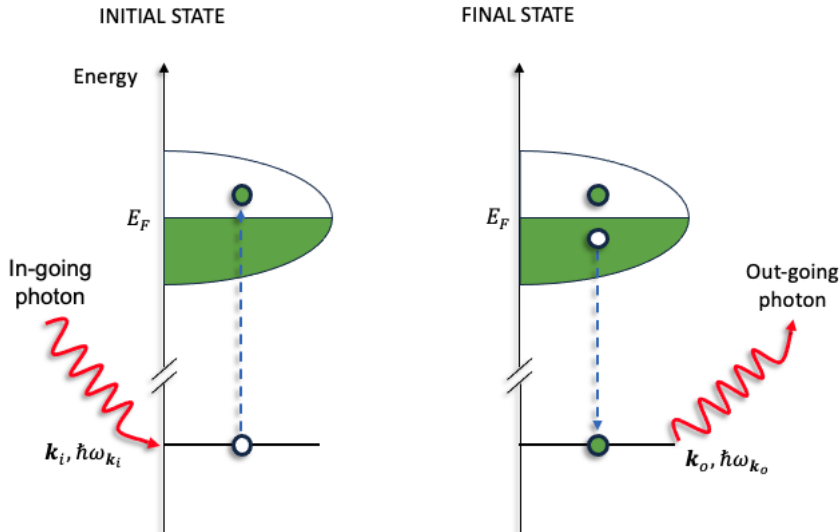


Figure 2.4: Schematization of the two steps involved in the scattering process. The first step consists of photon absorption leading to an unstable intermediate state, where the the electronic excitation leaves a core hole behind. In the second step, the final state is achieved by a valence electron-core hole recombination event.

### 2.2.3.  RIXS cross section in the single-ion model

The cross section for a RIXS event is calculated by means of the well-known Kramers-Heisenberg equation [65]:

$$\frac{d^2\sigma}{d\hbar\omega d\Omega} = r_e^2 m^2 \omega_{\mathbf{k}_o}^3 \omega_{\mathbf{k}_i} \sum_f \left| \sum_n \frac{\langle f|\mathcal{D}_o^\dagger|n\rangle \langle n|\mathcal{D}_i|g\rangle}{E_g + \hbar\omega_{\mathbf{k}} - E_n + i\Gamma_n} \right|^2 \delta(E_g - E_f + \hbar\omega) \qquad (2.9)$$

It is essentially the probability that an incoming x-ray photon with energy $\hbar\omega_{\mathbf{k}_i}$ is scattered to a state with energy $\hbar\omega_{\mathbf{k}_o}$ by one electron of the ionic species probed by the technique. $|g\rangle$ and $|f\rangle$ are the electronic initial and final states of the material, respectively, while $|n\rangle$ labels all available intermediate states of the two-steps process. $E_g$, $E_f$ and $E_n$ represent their corresponding energies. $\mathcal{D}_i$ and $\mathcal{D}_o$ are the transition dipole operators for the absorption step and the for the electron-hole relaxation step, respectively; they contain all information on the scattering geometry and on the polarization states of the incoming and out-going photons. Finally, the delta function ensures conservation of energy during the scattering process. The equation is derived in the framework of time-dependent perturbation theory and on the hypothesis of electric dipole approximation. More details on its derivation are found in Appendix A.1.

Luckily, the Kramers-Heisenberg formula can be largely simplified in the framework of the single-ion model. The RIXS measurements we discuss in this work were exclusively performed at the Cu $L_3$ absorption edge. Therefore, among the five (four) distinct cations in the HEO samples, we focus our attention on the Cu$^{2+}$ local environment probed by the technique. The electronic configuration of a Cu$^{2+}$ ion is [Ar]$3d^9$ and, in a $D_{4h}$ symmetry (see Fig. 2.1), one hole is left in the most energetic $3d_{x^2-y^2}$ level. The electronic properties of Cu$^{2+}$ are thus equivalent to the properties of a Hydrogen-like atom described by the wavefunction

$$\psi(r,\theta,\phi) = R_{n,l}(r)Y_{l,m}(\theta,\phi), \qquad (2.10)$$

which is solution (in spherical coordinates) of the Schrödinger equation in the spherically symmetric potential $V = -\frac{1}{4\pi\varepsilon_0}\frac{Ze^2}{r}$. $R_{n,l}(r)$ is the radial part of the wavefunction labelled by the principal quantum number $n$ and by the angular momentum quantum number $l$, while $Y_{l,m}(\theta,\phi)$ represents the spherical harmonic with $l$ and with magnetic quantum number $m$. In the following we will neglect the radial component since it is irrelevant to the RIXS cross section calculation. These simplifications are crucial in the calculation of the scattering cross section, that will be presented mostly along the lines of Moretti's work [58].

Before delving into this subject, we analyze the specific case of the scattering process at

the $L_3$ edge of Copper. An electron from the four-fold degenerate $2p_{\frac{3}{2}}$ states is promoted to the unoccupied $3d_{x^2-y^2}$ level upon photon absorption, leaving a core hole behind. The electronic excitation can be interpreted as a one-hole promotion from the $3d_{x^2-y^2}$ ground state to one of the $2p_{\frac{3}{2}}$ levels. In any case, the intermediate state is always represented by a fully occupied $3d$ shell and by a core hole in the $2p_{\frac{3}{2}}$ levels. The second step of the RIXS process consists in the radiative recombination of a $3d$ electron with the $2p_{\frac{3}{2}}$ core hole. Consequently, a hole is left either in the ground state $(3d_{x^2-y^2})$ or in a $3d$ state with different symmetry and/or spin state. We recall that all core levels can host 2 electrons with opposite spin state in agreement with Pauli exclusion principle, hence they are doubly degenerate. We assume, in the hole representation, a $|3d_{x^2-y^2}, \downarrow\rangle$ ground state, where arrows indicate the spin direction ($\uparrow$ for spin up and $\downarrow$ for spin down). In this hypothesis, a magnetic excitation (or spin-flip excitation) is interpreted as a scattering process where a core hole transits from the ground state $|3d_{x^2-y^2}, \downarrow\rangle$ to the excited state $|3d_{x^2-y^2}, \uparrow\rangle$, in systems where magnetic interactions are responsible for further splitting the $3d_{x^2-y^2}$ level. Instead, the elastic scattering implies a $|3d_{x^2-y^2}, \downarrow\rangle$ final state. All other $3d$ levels are the final states of local $dd$ excitations.

We report here the expression of the matrix element for a given final state $f$, extracted from the Kramers-Heisenberg equation (A.18):

$$\left.\frac{d^2\sigma}{d\hbar\omega d\Omega}\right|_f \propto \left|\sum_n \langle f|\mathcal{D}_o^\dagger|n\rangle\langle n|\mathcal{D}_i|g\rangle\right|^2 \tag{2.11}$$

where we recall that $|g\rangle$ and $|f\rangle$ are the material ground state and final state, respectively, and $n$ runs over all possible intermediate states.

As we assumed, the hole ground state $|g\rangle$ is $|3d_{x^2-y^2}, \downarrow\rangle$, while $|f\rangle$ is one of the $3d$ states. The $3d$ orbitals wavefunctions can be expressed as a linear combination of spherical harmonics with $l = 2$ and $m = -2, ..., 2$. Moreover, if we account for a generic spin direction of the hole with respect to an arbitrary $z$ quantization axis, we need to calculate the eigenstates of the spin operator

$$\sigma_s(\theta_s, \phi_s) = (\sigma_x \cos\phi_s + \sigma_y \sin\phi_s)\sin\theta_s + \sigma_z \cos\theta_s \tag{2.12}$$

where $\theta_s$ and $\phi_s$ define the spin direction and $\sigma_x$, $\sigma_y$ and $\sigma_z$ are Pauli matrices. The eigenstates are found by solving

$$\sigma_s(\theta_s, \phi_s)\begin{pmatrix} U_\pm \\ D_\pm \end{pmatrix} = \pm 1 \begin{pmatrix} U_\pm \\ D_\pm \end{pmatrix}. \tag{2.13}$$

$U_+$ ($U_-$) and $D_+$ ($D_-$) are the components of the eigenvector corresponding to the $+1$ ($-1$) eigenvalue. Finally, the expressions of the resulting 10 $3d$ orbitals can be calculated, and are shown in table 2.1; they represent the available final states of the scattering process, labelled with $|f\rangle$ in the matrix element. Instead, $2p$ intermediate states are characterised by a strong spin-orbit interaction, hence spin is not a good quantum number anymore. Again, $2p_{\frac{1}{2}}$ and $2p_{\frac{3}{2}}$ wavefunctions can be written as linear combinations of spherical harmonics (Tab. 2.2). In a RIXS process at the $L_3$ absorption edge, only states with $m_{3/2} = -\frac{3}{2}, ..., \frac{3}{2}$ are available as effective intermediate states. In the following we will focus our attention exclusively on them. The matrix element is then rewritten as

$$\frac{d^2\sigma}{d\hbar\omega d\Omega}\bigg|_f \propto \left| \sum_{m_{3/2}} \langle f|\mathcal{D}_o^\dagger|p_{\frac{3}{2},m_{3/2}}\rangle\langle p_{\frac{3}{2},m_{3/2}}|\mathcal{D}_i|d_{x^2-y^2},\downarrow\rangle \right|^2, \qquad (2.14)$$

| | |
|---|---|
| $\|d_{x^2-y^2},\downarrow\rangle$ | $\|\frac{1}{\sqrt{2}}\left[U_-\left(Y_{2,2}^\uparrow + Y_{2,\bar{2}}^\uparrow\right) + D_-\left(Y_{2,2}^\downarrow + Y_{2,\bar{2}}^\downarrow\right)\right]\rangle$ |
| $\|d_{x^2-y^2},\uparrow\rangle$ | $\|\frac{1}{\sqrt{2}}\left[U_+\left(Y_{2,2}^\uparrow + Y_{2,\bar{2}}^\uparrow\right) + D_+\left(Y_{2,2}^\downarrow + Y_{2,\bar{2}}^\downarrow\right)\right]\rangle$ |
| $\|d_{3z^2-r^2},\downarrow\rangle$ | $\|U_+Y_{20}^\uparrow + D_+Y_{20}^\downarrow\rangle$ |
| $\|d_{3z^2-r^2},\uparrow\rangle$ | $\|U_-Y_{20}^\uparrow + D_-Y_{20}^\downarrow\rangle$ |
| $\|d_{xy},\downarrow\rangle$ | $\|-\frac{i}{\sqrt{2}}\left[U_+\left(Y_{2,2}^\uparrow - Y_{2,\bar{2}}^\uparrow\right) + D_+\left(Y_{2,2}^\downarrow - Y_{2,\bar{2}}^\downarrow\right)\right]\rangle$ |
| $\|d_{xy},\uparrow\rangle$ | $\|-\frac{i}{\sqrt{2}}\left[U_-\left(Y_{2,2}^\uparrow - Y_{2,\bar{2}}^\uparrow\right) + D_-\left(Y_{2,2}^\downarrow - Y_{2,\bar{2}}^\downarrow\right)\right]\rangle$ |
| $\|d_{xz},\downarrow\rangle$ | $\|\frac{1}{\sqrt{2}}\left[U_+\left(Y_{2,1}^\uparrow - Y_{2,\bar{1}}^\uparrow\right) + D_+\left(Y_{2,1}^\downarrow - Y_{2,\bar{1}}^\downarrow\right)\right]\rangle$ |
| $\|d_{xz},\uparrow\rangle$ | $\|\frac{1}{\sqrt{2}}\left[U_-\left(Y_{2,1}^\uparrow - Y_{2,\bar{1}}^\uparrow\right) + D_-\left(Y_{2,1}^\downarrow - Y_{2,\bar{1}}^\downarrow\right)\right]\rangle$ |
| $\|d_{yz},\downarrow\rangle$ | $\|-\frac{i}{\sqrt{2}}\left[U_+\left(Y_{2,1}^\uparrow + Y_{2,\bar{1}}^\uparrow\right) + D_+\left(Y_{2,1}^\downarrow + Y_{2,\bar{1}}^\downarrow\right)\right]\rangle$ |
| $\|d_{yz},\uparrow\rangle$ | $\|-\frac{i}{\sqrt{2}}\left[U_-\left(Y_{2,1}^\uparrow + Y_{2,\bar{1}}^\uparrow\right) + D_-\left(Y_{2,1}^\downarrow + Y_{2,\bar{1}}^\downarrow\right)\right]\rangle$ |

Table 2.1: $3d$ states wavefunctions in the spherical harmonic basis.

| | |
|---|---|
| $\lvert p_{\frac{3}{2},\frac{3}{2}}\rangle$ | $\lvert Y_{1,1}^{\uparrow}\rangle$ |
| $\lvert p_{\frac{3}{2},\frac{1}{2}}\rangle$ | $\lvert\sqrt{\frac{2}{3}}Y_{1,0}^{\uparrow} + \sqrt{\frac{1}{3}}Y_{1,1}^{\downarrow}\rangle$ |
| $\lvert p_{\frac{3}{2},-\frac{1}{2}}\rangle$ | $\lvert\sqrt{\frac{1}{3}}Y_{1,\bar{1}}^{\uparrow} + \sqrt{\frac{2}{3}}Y_{1,0}^{\downarrow}\rangle$ |
| $\lvert p_{\frac{3}{2},-\frac{3}{2}}\rangle$ | $\lvert Y_{1,\bar{1}}^{\downarrow}\rangle$ |
| $\lvert p_{\frac{1}{2},\frac{1}{2}}\rangle$ | $\lvert -\sqrt{\frac{1}{3}}Y_{1,0}^{\uparrow} + \sqrt{\frac{2}{3}}Y_{1,1}^{\downarrow}\rangle$ |
| $\lvert p_{\frac{1}{2},-\frac{1}{2}}\rangle$ | $\lvert -\sqrt{\frac{2}{3}}Y_{1,\bar{1}}^{\uparrow} + \sqrt{\frac{1}{3}}Y_{1,0}^{\downarrow}\rangle$ |

Table 2.2: $2p_{\frac{1}{2},m_{1/2}}$ and $2p_{\frac{3}{2},m_{3/2}}$ states wavefunctions in the spherical harmonic basis.

where $\langle f\rvert$ is the corresponding bra of one of the $3d$ wavefunctions reported in Tab. 2.1. Up to now, the dependence of the RIXS process on the scattering geometry has not yet been explicitly addressed. The scattering geometry affects the cross section calculations through the polarization components of the photons, which in turn are found in the matrix elements, as we will see later on. In order to explain how this relation works, we start by defining the scattering geometry. The normalized wavevectors of the in-going and out-going photons in spherical coordinates are

$$\hat{\mathbf{k}}_i = \sin\theta_i\cos\phi_i\hat{\mathbf{x}} + \sin\theta_i\sin\phi_i\hat{\mathbf{y}} + \cos\theta_i\hat{\mathbf{z}} \tag{2.15}$$

$$\hat{\mathbf{k}}_o = \sin\theta_o\cos\phi_o\hat{\mathbf{x}} + \sin\theta_o\sin\phi_o\hat{\mathbf{y}} + \cos\theta_o\hat{\mathbf{z}} \tag{2.16}$$

where $\theta_i$ ($\theta_o$) and $\phi_i$ ($\phi_o$) uniquely define the incident (scattered) direction in the sample frame of reference. Usually, the components of the photon polarization are projected on a 2-dimensional basis. The versors of the basis (or polarization versors) are chosen to be parallel ($\pi$ direction) and perpendicular ($\sigma$ direction) to the scattering plane i.e. the plane where $\hat{\mathbf{k}}_i$ and $\hat{\mathbf{k}}_o$ wavevectors lie. Figure 2.5 proposes an illustration of the geometry of the RIXS process. The scattering plane is green-coloured: here the in-going wavevector $\hat{\mathbf{k}}_i$, the out-going wavevector $\hat{\mathbf{k}}_o$ and the $\pi$ polarization direction lie. Consistently, the $\sigma$ polarization direction is represented orthogonal to $\pi$. The incident angle is $\theta_i$, while the out-going photon is collected at angle $\theta_{out}$. $2\theta$ (or $tth$) is the scattering angle. $\theta$ represents the orientation of the in-going wavevector $\hat{\mathbf{k}}_i$ with respect to the sample surface. The angle arising between $\mathbf{y}$ and $\mathbf{k}_o - \mathbf{k}_i$ is named $\delta$. It carries the information on the direction of the transferred momentum $\mathbf{q}$. Correspondingly, $\mathbf{q}_{\parallel}$ is the projection of $\mathbf{q}$ along the $x$ axis. While $2\theta$ is independent from the sample orientation, $\theta$, $\delta$ and $\phi_{i,o}$ vary upon sample
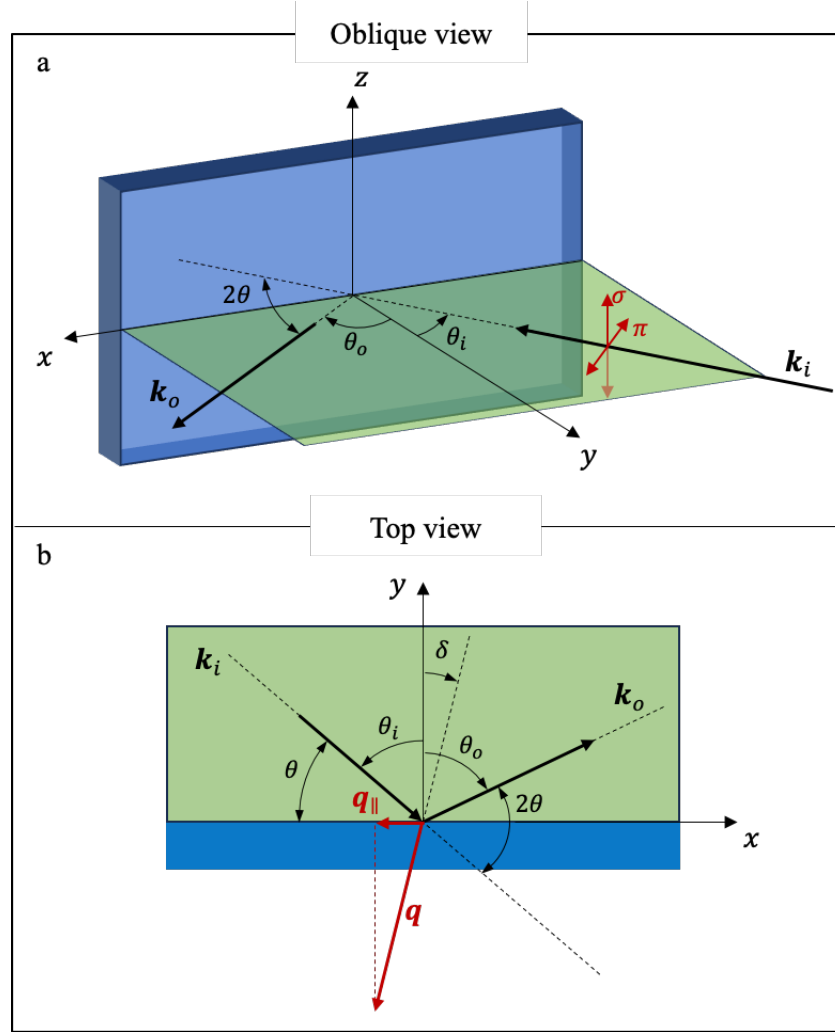
rotation.



Figure 2.5: Oblique (a) and top (b) views of the scattering geometry. Angles $\phi_i$ and $\phi_o$ are assumed to be null, hence the scattering plane is perpendicular to the sample surface.

Going back to the analytical description of polarization versors, we can define the in-going polarization versors as

$$\hat{\boldsymbol{\epsilon}}_i^\sigma = \hat{\mathbf{k}}_i \times \hat{\mathbf{k}}_o$$
$$\hat{\boldsymbol{\epsilon}}_i^\pi = \hat{\mathbf{k}}_i \times \hat{\boldsymbol{\epsilon}}_i^\sigma,$$

$(2.17)$

while the out-going polarization versors are written as

$$\hat{\boldsymbol{\epsilon}}_o^\sigma = \hat{\boldsymbol{\epsilon}}_i^\sigma$$
$$\hat{\boldsymbol{\epsilon}}_o^\pi = \hat{\mathbf{k}}_o \times \hat{\boldsymbol{\epsilon}}_o^\sigma.$$

$(2.18)$

The components of the left-circular $(L)$, right-circular $(R)$ and linear $(z)$ photon polar-

ization along the $\sigma$ direction are calculated exploiting the following scalar products:

$$L_{i(o)}^\sigma = \hat{\boldsymbol{\epsilon}}_{i(o)}^\sigma \cdot \left[\frac{\hat{\mathbf{x}} - i\hat{\mathbf{y}}}{\sqrt{2}}\right]$$

$$R_{i(o)}^\sigma = -\hat{\boldsymbol{\epsilon}}_{i(o)}^\sigma \cdot \left[\frac{\hat{\mathbf{x}} + i\hat{\mathbf{y}}}{\sqrt{2}}\right] \tag{2.19}$$

$$z_{i(o)}^\sigma = \hat{\boldsymbol{\epsilon}}_{i(o)}^\sigma \cdot \hat{\mathbf{z}}$$

Analogous equations can be written to calculate $L$, $R$ and $z$ components along the $\pi$ direction:

$$L_{i(o)}^\pi = \hat{\boldsymbol{\epsilon}}_{i(o)}^\pi \cdot \left[\frac{\hat{\mathbf{x}} - i\hat{\mathbf{y}}}{\sqrt{2}}\right]$$

$$R_{i(o)}^\pi = -\hat{\boldsymbol{\epsilon}}_{i(o)}^\pi \cdot \left[\frac{\hat{\mathbf{x}} + i\hat{\mathbf{y}}}{\sqrt{2}}\right] \tag{2.20}$$

$$z_{i(o)}^\pi = \hat{\boldsymbol{\epsilon}}_{i(o)}^\pi \cdot \hat{\mathbf{z}}$$

Now, all quantities required for the full characterization of the dipole transition operators have been introduced. In the following the matrix formalism will be used. The matricial form of the dipole transition operator in the spherical harmonics basis, $\mathcal{D}_{sph}$, is

$$
\begin{array}{c}
\begin{array}{cccccccccc}
Y_{2,2}^\downarrow & Y_{2,2}^\uparrow & Y_{2,1}^\downarrow & Y_{2,1}^\uparrow & Y_{2,0}^\downarrow & Y_{2,0}^\uparrow & Y_{2,\bar{1}}^\downarrow & Y_{2,\bar{1}}^\uparrow & Y_{2,\bar{2}}^\downarrow & Y_{2,\bar{2}}^\uparrow
\end{array} \\
\begin{array}{c}
Y_{1,1}^\downarrow \\ Y_{1,1}^\uparrow \\ Y_{1,0}^\downarrow \\ Y_{1,0}^\uparrow \\ Y_{1,\bar{1}}^\downarrow \\ Y_{1,\bar{1}}^\uparrow
\end{array}
\left(
\begin{array}{cccccccccc}
-\sqrt{6}L & 0 & \sqrt{3}z & 0 & -\sqrt{1}R & 0 & 0 & 0 & 0 & 0 \\
0 & -\sqrt{6}L & 0 & \sqrt{3}z & 0 & -\sqrt{1}R & 0 & 0 & 0 & 0 \\
0 & 0 & -\sqrt{3}L & 0 & \sqrt{4}z & 0 & -\sqrt{3}R & 0 & 0 & 0 \\
0 & 0 & 0 & -\sqrt{3}L & 0 & \sqrt{4}z & 0 & -\sqrt{3}R & 0 & 0 \\
0 & 0 & 0 & 0 & -\sqrt{1}L & 0 & \sqrt{3}z & 0 & -\sqrt{6}R & 0 \\
0 & 0 & 0 & 0 & 0 & -\sqrt{1}L & 0 & \sqrt{3}z & 0 & -\sqrt{6}R
\end{array}
\right).
\end{array} \tag{2.21}
$$

Just to make an example, the matrix element in position $(1,1)$ was obtained solving the integral $\langle Y_{1,1}^\downarrow | \mathcal{D}_i | Y_{2,2}^\downarrow \rangle$. Since we are interested in transitions involving $2p$ and $3d$ states, it is useful to rewrite the operator in a cubic harmonics basis, as reported here:

$$
\begin{array}{c}
\begin{array}{ccc}
d_{x^2-y^2,\downarrow} & \dots & d_{yz,\uparrow}
\end{array} \\
\begin{array}{c}
p_{\frac{3}{2},\frac{3}{2}} \\ \vdots \\ p_{\frac{1}{2},-\frac{1}{2}}
\end{array}
\left(
\begin{array}{ccc}
\langle p_{\frac{3}{2},\frac{3}{2}} | \mathcal{D}_i | d_{x^2-y^2},\downarrow \rangle & \dots & \langle p_{\frac{3}{2},\frac{3}{2}} | \mathcal{D}_i | d_{yz},\uparrow \rangle \\
\vdots & \ddots & \vdots \\
\langle p_{\frac{1}{2},-\frac{1}{2}} | \mathcal{D}_i | d_{x^2-y^2},\downarrow \rangle & \dots & \langle p_{\frac{1}{2},-\frac{1}{2}} | \mathcal{D}_i | d_{yz},\uparrow \rangle
\end{array}
\right)
\end{array} \tag{2.22}
$$

By doing so, the resulting 6x10 matrix (from now on, $\mathcal{D}_{cub}$) intrinsically contains the matrix elements appearing in the Kramers-Heisenberg formula. $\mathcal{D}_{cub}$ is calculated from

$\mathcal{D}_{sph}$ performing the basis transformation

$$\mathcal{D}_{cub} = \mathcal{T}_p \mathcal{D}_{sph} \mathcal{T}_d^\dagger, \tag{2.23}$$

where $\mathcal{T}_d$ is the transition matrix transforming a spherical harmonics basis with $l = 2$ into the 10-dimensional $3d$ orbitals basis (Tab. 2.1), while $\mathcal{T}_p$ is the transition matrix from the spherical harmonics basis with $l = 1$ to the 6-dimensional $2p$ orbitals basis (Tab. 2.2). $\mathcal{T}_d$ and $\mathcal{T}_p$ are reported in Appendix A.2. Actually, equation 2.23 allows to evaluate only the matrix elements related to the absorption step of the RIXS process, involving the promotion of the $3d$ core hole to the $2p$ shell. This is why we used the transition operator from the initial state $\mathcal{D}_i$ in 2.22. The matrix elements related to the second step (electron-hole radiative recombination) are found by taking the conjugate transpose of $\mathcal{D}_{cub}$:

$$\mathcal{D}_{cub}^\dagger = \mathcal{T}_d \mathcal{D}_{sph}^\dagger \mathcal{T}_p^\dagger. \tag{2.24}$$

The resulting 10x6 matrix is written in the form

$$
\begin{array}{c}
\\
d_{x^2-y^2},\downarrow \\
\vdots \\
d_{yz},\uparrow
\end{array}
\begin{pmatrix}
\overset{p_{\frac{3}{2},\frac{3}{2}}}{\langle d_{x^2-y^2},\downarrow |\mathcal{D}_o|p_{\frac{3}{2},\frac{3}{2}}\rangle} & \overset{\cdots}{\cdots} & \overset{p_{\frac{1}{2},-\frac{1}{2}}}{\langle d_{x^2-y^2},\downarrow |\mathcal{D}_o|p_{\frac{1}{2},-\frac{1}{2}}\rangle} \\
\vdots & \ddots & \vdots \\
\langle d_{yz},\uparrow |\mathcal{D}_o|p_{\frac{3}{2},\frac{3}{2}}\rangle & \cdots & \langle d_{yz},\uparrow |\mathcal{D}_o|p_{\frac{1}{2},-\frac{1}{2}}\rangle
\end{pmatrix}. \tag{2.25}
$$

In order to take into account the effect of spin-orbit coupling on $d$ states, another basis transformation is required. Indeed, as introduced in section 2.1.3, the eigenstates of the Hamiltonian $\mathcal{H}_{tot} = \mathcal{H}_{CF} + \mathcal{H}_{SO}$ are no longer the $3d$ states and writing the operators in the cubic harmonics basis becomes meaningless. The new basis are the column vectors of $\mathcal{T}_{SO}$, i.e., the eigenstates of $\mathcal{H}_{tot}$, obtained by solving the eigenvalue equation 2.5. Consequently, the complete basis transformation to apply is encompassed by the following equation:

$$\mathcal{D}_{cub} = \mathcal{T}_p \mathcal{D}_{sph} \mathcal{T}_d^\dagger \mathcal{T}_{SO}. \tag{2.26}$$

It provides the matrix elements of the absorption step in the new basis. Analogously, the equation

$$\mathcal{D}_{cub}^\dagger = \mathcal{T}_{SO}^\dagger \mathcal{T}_d \mathcal{D}_{sph}^\dagger \mathcal{T}_p^\dagger \tag{2.27}$$

is valid for the core-hole relaxation step.

In conclusion, we underline that a correction to the scattering cross section formula we derived must be made. Indeed, even though polarization-resolved RIXS of orbital and

spin excitations at ESRF is possible [72], we didn't measure the polarization of the out-going photons. Consequently, an integration over the out-going polarization states has to be included. If $q$ and $q'$ label the in-going and out-going photon polarizations ($\sigma$ or $\pi$), respectively, the RIXS cross section formula is revisited as

$$\left.\frac{d^2\sigma}{d\hbar\omega d\Omega}\right|_f \propto \sum_{q'}\left|\sum_{m_{3/2}}\langle f|\mathcal{D}^{\dagger}_{o,q'}|p_{\frac{3}{2},m_{3/2}}\rangle\langle p_{\frac{3}{2},m_{3/2}}|\mathcal{D}_{i,q}|d_{x^2-y^2},\downarrow\rangle\right|^2. \tag{2.28}$$

### 2.2.4.  RIXS cross section for a powder sample

The scattering cross section we derived is suited for a single-crystal system, where the incoming and scattered photon wavevectors have the same orientation with respect to any octahedral units in Cu$^{2+}$ lattice sites. Polycrystalline materials, such as powder samples, are composed of many crystallites with several distinct orientations; the incoming x-ray radiation impinges with different incident angles the local octahedral structures found in distinct crystallites. Hence, an integration of the scattering cross section over all crystallite orientations is required to take into account the polycrystalline nature of the probed samples. For the sake of clarity we report the expressions for the in-going and out-going normalized photon wavevectors:

$$\hat{\mathbf{k}}_i = \sin\theta_i\cos\phi_i\hat{\mathbf{x}} + \sin\theta_i\sin\phi_i\hat{\mathbf{y}} + \cos\theta_i\hat{\mathbf{z}} \tag{2.29}$$

$$\hat{\mathbf{k}}_o = \sin\theta_o\cos\phi_o\hat{\mathbf{x}} + \sin\theta_o\sin\phi_o\hat{\mathbf{y}} + \cos\theta_o\hat{\mathbf{z}} \tag{2.30}$$

recalling that $\theta_{i(o)}$ and $\phi_{i(o)}$ define the direction of the wavevectors in the sample reference system. In a single crystal all octahedral structures are equally oriented and the $\{\theta_{i(o)}, \phi_{i(o)}\}$ set of angles can be exploited for any photon-ion scattering event. In a poly-crystal, instead, this set must be re-defined for any single event. This problem is simplified if we assume that octahedral units are randomly and homogeneously oriented in space. On these premises, from a purely analytical perspective, the solution consists in performing an integration of the RIXS cross section over all space. Due to computational reasons, we decided to perform a random sampling of the infinite available directions. The RIXS cross section for a powder sample is then calculated as the spatial average over all sampled orientations:

$$\sigma_{powder} = \frac{1}{N_o}\sum_{\hat{\mathbf{k}}_{i,l},\hat{\mathbf{k}}_{o,l}}\frac{d^2\sigma}{d\hbar\omega d\Omega}\left(\hat{\mathbf{k}}_{i,l}, \hat{\mathbf{k}}_{o,l}\right) \tag{2.31}$$

$N_o$ represents the number of sampled orientations, while $\hat{\mathbf{k}}_{i,l}$ and $\hat{\mathbf{k}}_{o,l}$ are the in-going and out-going wavevectors written in the $l^{th}$ octahedron reference system. $\hat{\mathbf{k}}_{i,l}$ ($\hat{\mathbf{k}}_{o,l}$) is calculated applying a proper rotation matrix to $\hat{\mathbf{k}}_i$ ($\hat{\mathbf{k}}_o$):

$$\hat{\mathbf{k}}_{i,l} = \mathcal{R}(\alpha_l, \beta_l, \gamma_l)\hat{\mathbf{k}}_i \tag{2.32}$$

$$\hat{\mathbf{k}}_{o,l} = \mathcal{R}(\alpha_l, \beta_l, \gamma_l)\hat{\mathbf{k}}_o \tag{2.33}$$

$\mathcal{R}$ is expressed as a function of the Euler angles $\alpha$, $\beta$ and $\gamma$ [73]. To implement the randomic character of the sampling procedure, $\alpha$ and $\gamma$ are chosen randomly in the range $[0, 2\pi]$, while $\beta$ is chosen within the range $[0, \pi]$. The full expression of the matrix $\mathcal{R}$ for the $l^{th}$ orientation is reported below:

$$\begin{pmatrix} \cos\alpha_l\cos\beta_l & \cos\alpha_l\sin\beta_l\sin\gamma_l - \sin\alpha_l\cos\gamma_l & \cos\alpha_l\sin\beta_l\cos\gamma_l + \sin\alpha_l\sin\gamma_l \\ \sin\alpha_l\cos\beta_l & \sin\alpha_l\sin\beta_l\sin\gamma_l + \cos\alpha_l\cos\gamma_l & \sin\alpha_l\sin\beta_l\cos\gamma_l - \cos\alpha_l\sin\gamma_l \\ -\sin\beta_l & \cos\beta_l\sin\gamma_l & \cos\beta_l\cos\gamma_l \end{pmatrix}. \tag{2.34}$$

Finally, figure 2.6 shows the calculated single-ion RIXS cross sections for powder samples, at the $Cu^{2+}$ $L_3$ absorption edge, as a function of the $2\theta$ angle. Each panel report the cross section of the core hole transition from the ground state $d_{x^2-y^2}, \downarrow$ to the corresponding final state indicated on the side (spin-up states on the left side, spin-down states on the right side). Red lines are referred to processes involving photons with in-going $\sigma$ polarization, while black lines are referred to processes with in-going $\pi$ polarization. In all cases, consistently with equation 2.28, a summation over $\sigma$ and $\pi$ out-going photon polarizations has been performed. We choose to represent the cross sections as a function of the angle $2\theta$ since it is the only reasonable choice in case of powders. Indeed, when integrating over spatial orientations, the cross sections lose their $\theta$ (and $\delta$) dependence and they would appear as constant quantities. The cross section of the elastic transition $\sigma_{x^2-y^2, \downarrow}$ ($|d_{x^2-y^2}, \downarrow\rangle \to |d_{x^2-y^2}, \downarrow\rangle$, panel $b$) appears to be stronger than the spin-flip excitation $\sigma_{x^2-y^2, \uparrow}$ ($|d_{x^2-y^2}, \downarrow\rangle \to |d_{x^2-y^2}, \uparrow\rangle$, panel $a$), especially in case of in-going $\sigma$ polarization. Cross sections exhibit, in general, low $2\theta$ and in-going polarization channel dependences. Two exceptions are mentioned: the cross section of the transition to the $|d_{xy}, \uparrow\rangle$ state (panel $e$) is affected by sizeable modulation upon variations of both $2\theta$ and in-going photon polarization; an analogous comment can be made to the cross section shown in panel $a$, associated to the spin-flip excitation. In any case, residual modulations will be exploited to associate the excitations to the distinguishable features of collected RIXS spectra.
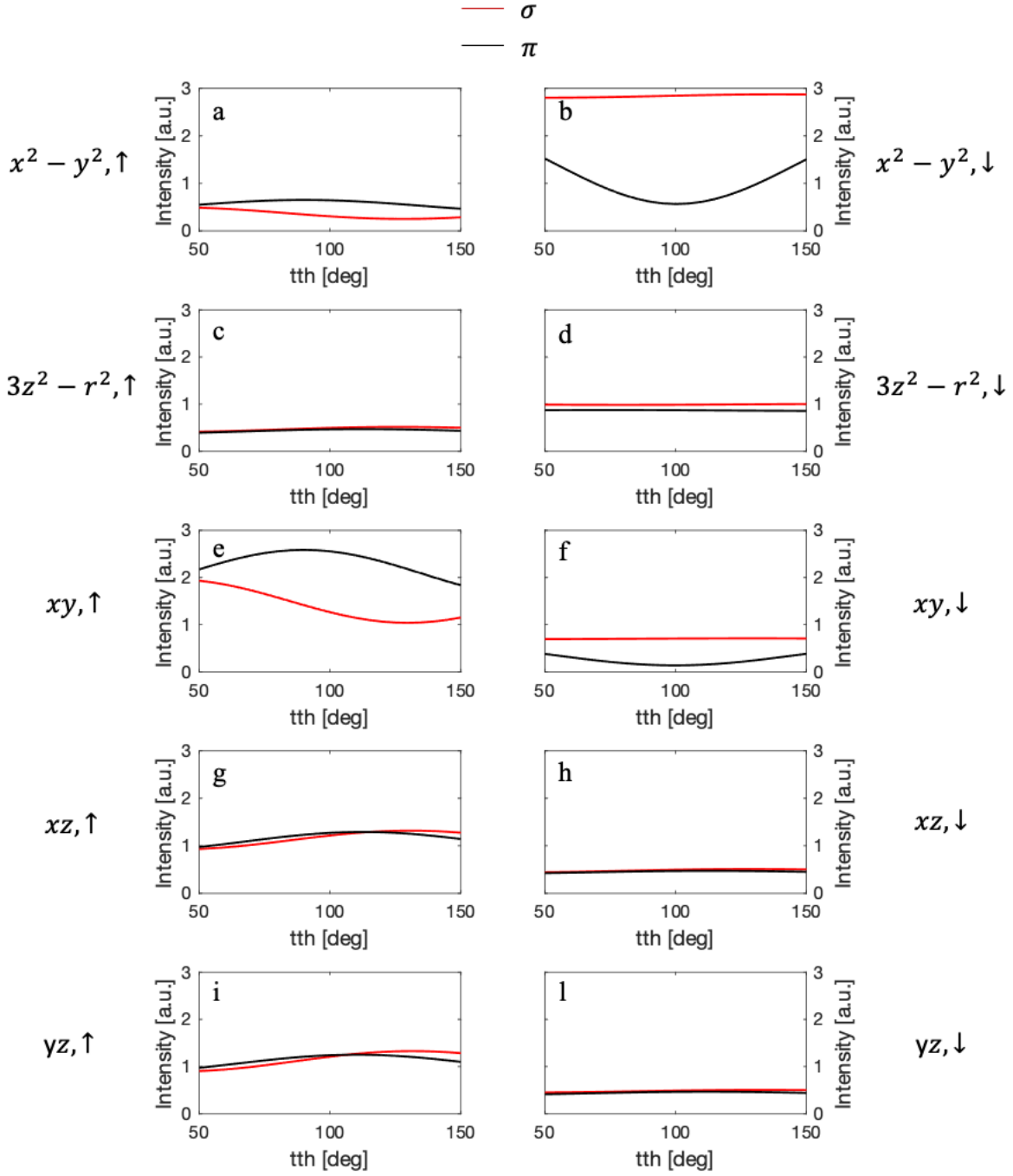
Figure 2.6: Single-ion RIXS cross sections calculated for a powder sample, assuming $\phi_i = \phi_o = 0$. The core-hole spin direction is assumed to be defined by $\theta_s = \frac{\pi}{2}$ and $\phi_s = \frac{\pi}{4}$.

## 2.3. Experimental set-up

As previously mentioned, RIXS is a second order process, thus intrinsically inefficient. The technique requires collimated x-ray beams with large brilliance, in order to provide high output intensity and significant spectra. Hence, RIXS must be performed at extremely brilliant light sources: nowadays either synchrotron radiation sources or Free-Electron Lasers (FELs) constitutes valid solutions. Since we carried out the experiment at ESRF in Grenoble, we will focus our attention on the general properties of a synchrotron radiation source. Subsequently, the ID32 beamline at ESRF will be briefly described.

### 2.3.1. Synchrotron radiation source

It is known that, when charged particles are accelerated, they emit electromagnetic radiation. Synchrotrons produce collimated and extremely brilliant radiation exploiting the acceleration of relativistic electrons. At ESRF, high-energy electrons are emitted by an electron gun and are accelerated by a linear accelerator (Linac) until they travel at relativistic speed, so that the wavelengths of the emitted photons fall in the x-ray spectral region. Subsequently, electrons are injected into a booster synchrotron, a ring-shaped structure exploited to increase electron energies up to 6 GeV. Finally, electrons travel into the storage ring. The storage ring is 844 meters long and electrons are kept under ultra-high vacuum conditions (about $10^{-9}$ mbar). The operational ring current is maintained constant at 200 mA by periodic injection of electrons. A schematic representation of the ESRF facility is proposed in Fig. 2.7. The beamlines are the paths connecting the storage ring to the experimental end-stations. They are cylindrical metal pipes, under ultra-high vacuum, responsible for the travelling of photons emitted from the storage ring to the physical places where experiments are taken. Throughout the whole ring, bending magnets and insertion devices (IDs) are implemented. They are systems of magnets required to bend the electron trajectory and produce light emission. Specifically, **bending magnets** are electromagnets able to generate a strong constant magnetic field towards a direction perpendicular to the storage ring. Each time an electron passes through a magnet, it is forced to change direction and to follow a circular orbit. Moreover, electrons suffer from energy loss in the form of electromagnetic radiation - called **synchrotron light** - directed tangentially to the electron orbit and towards the beamlines. The collimated beam is cone-shaped and the width $\theta_{lc}$ of the emitted light-cone is

$$\theta_{lc} \propto \frac{1}{\gamma}, \tag{2.35}$$

where $\gamma = \frac{1}{\sqrt{1-\frac{v^2}{c^2}}}$ is the relativistic Lorentz factor. Thus, electrons with very high speed will produce a more collimated photon beam.

**Undulators** consist in a set of bending magnets with alternating polarity. When electrons are injected in an undulator, they are forced to follow an oscillating trajectory. At each curve, x-ray radiation is produced and the interaction between x-ray beams from distinct curved result in constructuve interference. If $N$ is the number of periods, the emitted radiation is $N^2$ times more intense than the radiation emitted by bending magnets.

Finally, **focusing magnets** are exploited to keep the electron beam collimated so that it follows the correct orbital trajectory.
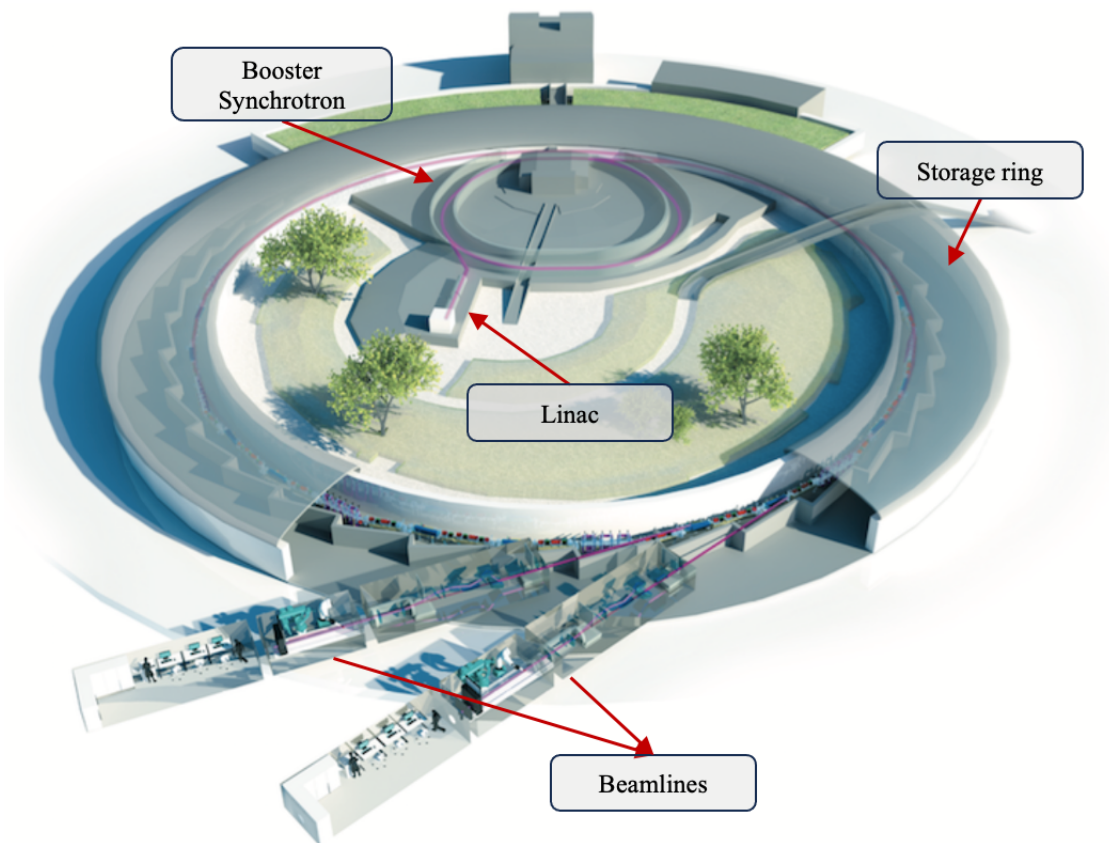


Figure 2.7: Model of the European Synchrotron Radiation Facility. Figure adapted from [74].

### 2.3.2. ID32 RIXS beamline at ESRF

The ID32 beamline at ESRF [61] hosts both a RIXS end-station and an X-ray Magnetic Circular Dichroism (XMCD) end-station. As a consequence, a proper optical system able to provide soft x-rays at both end-stations is required (Fig. 2.8).
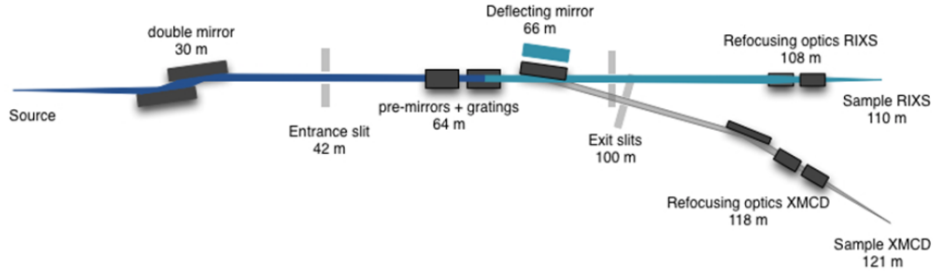


Figure 2.8: ID32 beamline optics [75].

Since the beamline is 100-120 meters long, a system of mirrors is required to keep the beam collimated and focused on the sample. The refocusing optics, found just before the end of the beamline, guarantees a $4 \times 60$ $\mu m^2$ (vertical $\times$ horizontal) beam-size at the sample. The beamline was chosen to be long for essentially two reasons: to allow for the implementation of a large spectrometer (later introduced) and to ensure the separation of the RIXS and XMCD branches. A deflecting mirror can deviate the photon flux towards the XMCD end-station. Since RIXS is a photon-hungry technique, the beamline is equipped with three undulators: one of them is 2.5 meters long (HU88B), others are 1.6 meters long (HU88A and HU88C). The emitted light spans within the 400 eV - 1600 eV energy range. Moreover, undulators provide horizontal linear, vertical linear and circularly polarized light; this is strictly necessary to perform polarized-dependent experiments both at the RIXS branch and at the XMCD branch. The beamline is also equipped with a variable line spacing (VLS) plane grating monochromator [76], with the aim to achieve the highest possible energy resolution.

The sample is located on a ultra-high vacuum-compatible diffractometer, kept inside a sample storage chamber. The diffractometer is exploited to control the scattering geometry, while keeping the incoming beam at the center of rotation of the sample. Specifically, it can translate the sample with respect to the centre of rotation towards three mutually perpendicular directions $x$, $y$ and $z$. It also guarantees four rotational operations. The diffractometer is equipped with a liquid He cryostat, allowing for low-temperature measurements. The minimum temperature achieved by the system is 15 K; in these conditions, the He consumption reaches 0.17 Lmin⁻¹. The final stage of the beamline is the

ERIXS spectrometer, responsible for the measurement of the spectral components of the scattered light. A picture of the spectrometer is reported in Fig. 2.9, together with the schematic of its optical layout (Fig. 2.10). It has an 11 meters moving arm capable of rotating over a 100 degrees angular range, which enables light detection with scattering angle $2\theta$ within the 50-150 degrees interval. The spectrometer arm features a collimating mirror (CM in Fig. 2.10), two gratings (G1 and G2) to disperse scattered photons on the CCD detector and a polarimeter to measure the out-going photon polarization. In the high-resolution mode, the beamline-spectrometer combined energy resolution at the Cu $L_3$ edge reaches 31 meV.
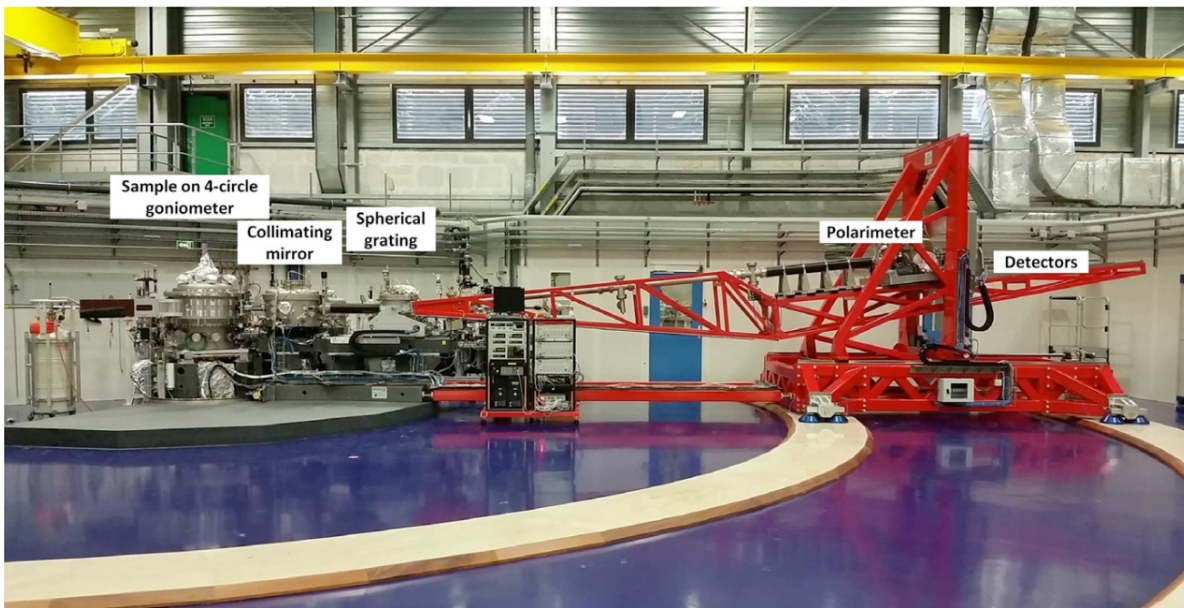


Figure 2.9: Picture showing the ERIXS spectrometer and the sample storage chamber. The main components of the system are indicated [61].

Figure 2.10: Optical layout of the ERIXS spectrometer [61].

# 3 | Ligand field and magnetic excitations in Mg-CNCZ and CNCZ

In the present chapter we report the results of a set of RIXS experiments carried out on both Mg-CNCZ and CNCZ HEOs samples. Performing quantitative and qualitative analysis of the spectra, we will extract relevant information about their structure and their magnetic properties. Before that, a preliminary analysis - based on X-ray Absorption Spectroscopy (XAS) - was complemented to RIXS experiments to check the valence of the ions in the samples by comparison with benchmark spectra. Then, RIXS experiments took place. Five RIXS spectra were collected from each sample with the idea to probe distinct scattering geometries and polarization channels. All tested configurations are listed in table 3.1.

| $2\theta$ [deg] | Polarization |
|:---:|:---:|
| 145 | $\pi$ |
| 110 | $\pi$ |
| 90 | $\pi, \sigma$ |
| 70 | $\pi$ |

Table 3.1: Tested RIXS configurations on Mg-CNCZ and CNCZ.

To reach the correct geometries, the spectrometer arm was made to rotate over the $2\theta$ degree of freedom, while in-going polarization channels were set by acting on the undulators phase. The experiments didn't make use of the beamline polarimeter, hence the output intensity encompasses both $\sigma$ and $\pi$ polarized light.

## 3.1.    Preliminary XAS analysis

As a preliminary work, XAS measurements were performed on Mg-CNCZ and CNCZ HEO samples in Total Electron Yield (TEY) mode. We focused our attention on the analysis of transition metals with partially filled shells: we probed the $L_2$ and $L_3$ absorption edges of Cu, Ni and Co by properly tuning the incoming photon energy. Moreover, a XAS measurement at the K edge of O was also collected. Results are reported in Fig. 3.1. The Cu XAS spectra, shown in the upper panel, are peculiar to divalent $Cu^{2+}$ ions [77, 78], consistently with the expected $3d^9$ configuration of Cu in rock-salt HEOs. Two prominent features are easily observed at 931 eV and at 950.5 eV, related to $L_3$ and $L_2$ edges, respectively. As expected, multiplet splitting is also observed in Ni XAS spectra: $2p_{\frac{3}{2}}$ and $2p_{\frac{1}{2}}$ peaks are visible at about 853 eV and 871 eV. The depicted satellite features are interpreted as absorption events from hybridized ligand field states [79] and the spectral profile follows the trend observed in XAS experiments on divalent Ni ions [80]. Analogous considerations can be done regarding Co and O ions: Co spectra show unambiguous similarities to CoO XAS spectra, where Co is divalent [81, 82], while the absorption features at the K edge of O are comparable to those present in XAS spectra of $3d$ monoxides (such as CoO or NiO) [83].

Being an absorption technique, XAS should be able, in principle, to probe the energy of transition metal $d$ states, extracting information on the crystal field on par with RIXS. Actually, the technique suffers from two fundamental issues:

- occupied states are invisible to XAS. Indeed, upon photon absorption, the excited electron transits necessarily to one of the unoccupied transition metal $3d$ states, while occupied states are strictly forbidden by Pauli exclusion principle. In the most striking case of $Cu^{2+}$, XAS is able to probe the $d_{x^2-y^2}$ state uniquely, being it the only empty state in the $d$ shell;

- even assuming the probeability of each state, XAS would suffer from core-hole lifetime broadening. Indeed, in an x-ray absorption process the excited state is highly unstable, being significantly more energetic (in the order of keV) than the ground state of the system. Correspondingly, the electron-hole recombination time is dramatically small and absorption features on XAS spectra would be characterized by $\sim$300 meV FWHM.

That said, XAS proves to be ineffective at measuring the HEO crystal field. To pursue this goal, RIXS experiment were carried out and their results will be presented in the next section.
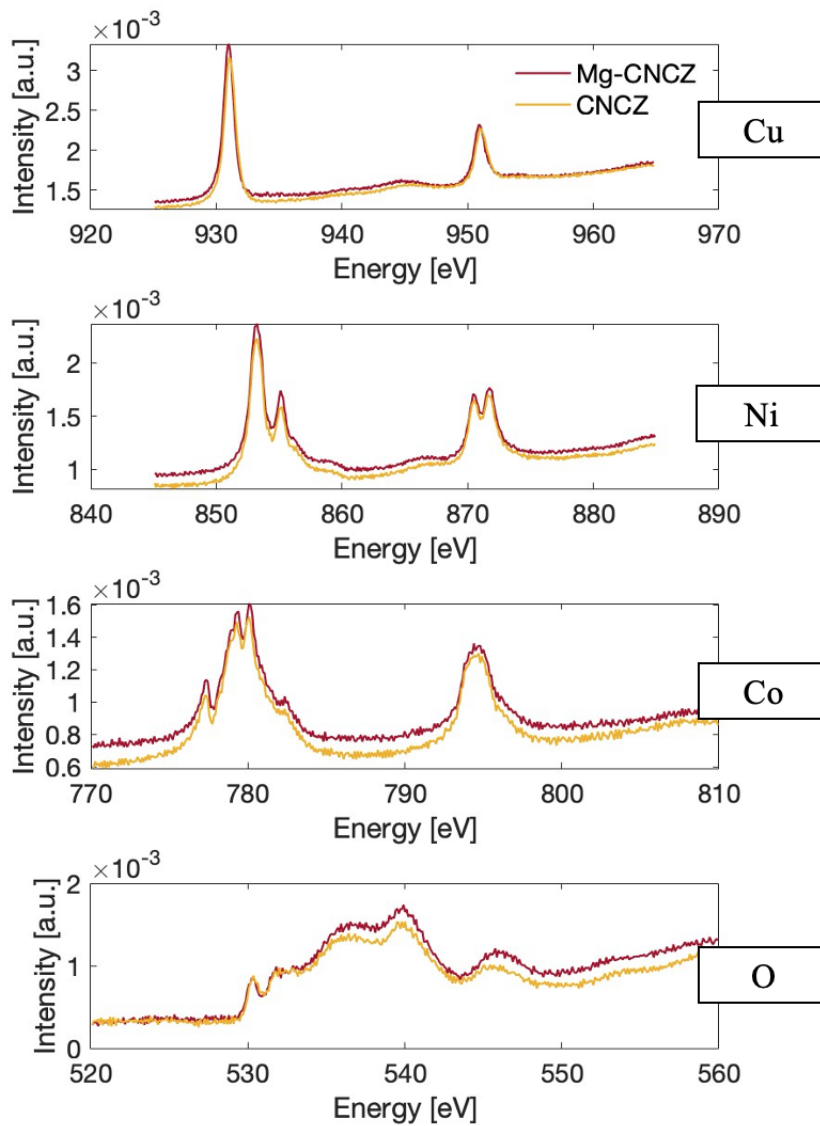
Figure 3.1: Experimental x-ray absorption spectra of Cu, Ni, Co and O in Mg-CNCZ and CNCZ samples.

## 3.2.   *dd* **and Charge-Transfer features**

When we introduced Ligand Field theory, we highlighted that a detailed description of the electronic properties of transition metals should take into consideration not only the crystal field acting on $3d$ orbitals, but also their superposition with the surrounding O $2p$ orbitals. This information is contained in the orbital excitations found in RIXS spectra, which will be analyzed throughout this section. Orbital features of Mg-CNCZ and CNCZ will be compared with the aim to check and interpret possible structural differences. Before that, let us analyse one of the collected spectra.
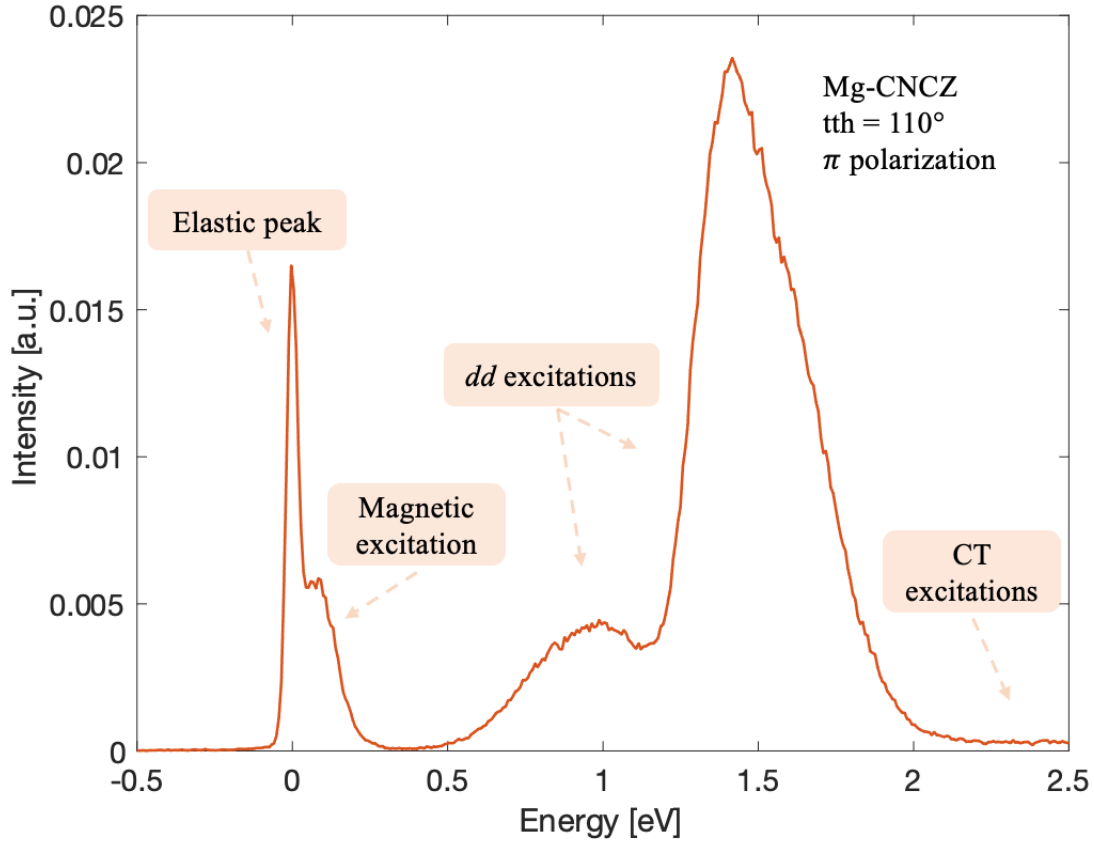


Figure 3.2: Experimental RIXS spectrum collected at $2\theta = 110°$, with $\pi$ in-going photon polarization. The main features are labelled.

Fig. 3.2 reports the RIXS spectrum collected at $2\theta = 110$ with $\pi$ in-going polarization channel. At a first glance, four main features are identified. A strong elastic peak dominates the low-energy region, while a smaller peak arises at about 0.1 eV and is partially covered by the elastic tail. Its origin is magnetic and will be discussed in the next section. Two broader features are found roughly from 0.5 eV to 2 eV and are attributed to *dd*

excitations. Specifically, the pronounced peak at $\sim 1$ eV is attributed to the transition from the $d_{x^2-y^2}$ to the $d_{3z^2-r^2}$ state, as one can infer by comparison with well-known RIXS spectra at the Cu $L_3$ edge in copper oxides, although its position is usually higher in energy [84]. The wide feature around 1.5 eV incorporates all other $dd$-related peaks. Finally, the weak and broad non-zero intensity found at high energy loss (above 2 eV) is attributed to CT excitations. To learn more about the HEOs crystal field, we first concentrate on $dd$ excitations.
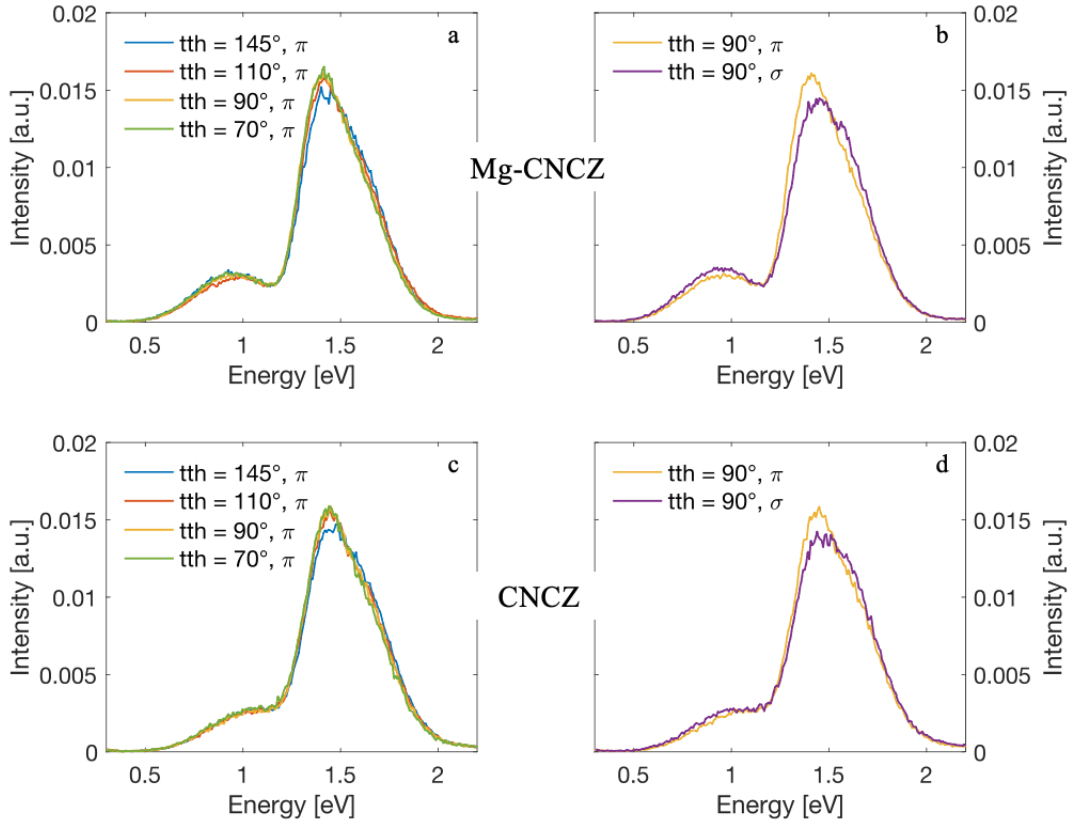


Figure 3.3: Normalized $dd$ excitations in Mg-CNCZ and CNCZ samples. Panels $a$ and $c$ compare spectra taken at distinct scattering angles, while panels $b$ and $d$ highlight the polarization dependence at constant $2\theta$.

Collected spectra are organized in Fig. 3.3 to highlight $dd$ excitations dependencies on the scattering angle and on the in-going photon polarization. In the spectra collected from Mg-CNCZ and CNCZ at distinct scattering angles (panel $a$ and $c$) little variations in shape and intensity are observed: the main peak is characterized by a small, but clear decrease of intensity, while a high energy shoulder grows with larger scattering angles. Similar, but more pronounced effects are observed when switching the incident photon polarization (panel $b$ and $d$).

Interestingly, an inspection of the $d_{3z^2-r^2}$ peak position reveals important differences between the RIXS spectra of the two samples at all scattering angles, as shown in Fig. 3.4.
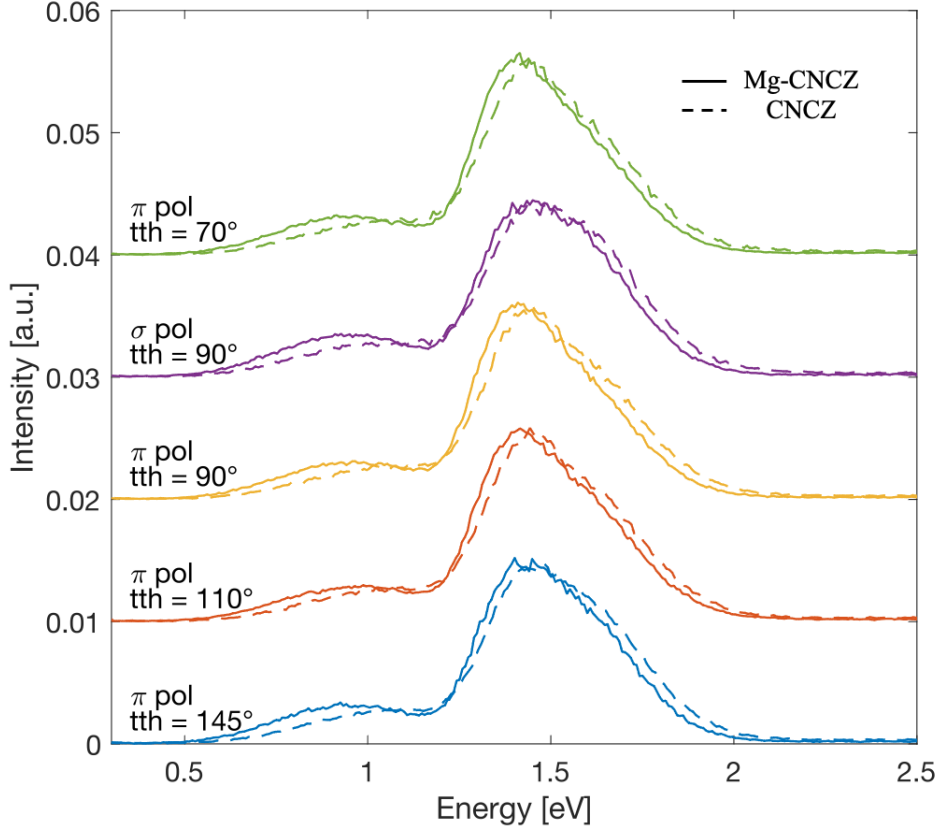


Figure 3.4: Normalized $dd$ excitations for all scattering configurations. A direct comparison shows a small energy shift between Mg-CNCZ and CNCZ $d_{3z^2-r^2}$ peaks.

It is evident that $d_{3z^2-r^2}$ peaks from CNCZ spectra are blue-shifted with respect to $d_{3z^2-r^2}$ peaks in Mg-CNCZ spectra. Moreover, a smaller blue-shift involves also the more energetic $dd$ feature. This is a common result to all spectra, regardless of the scattering angle or polarization channel. From CF theory, we know that the position of $3d$ levels is directly related to the local coordination of the probed Cu$^{2+}$ ion: the energy difference between $d_{x^2-y^2}$ and $d_{3z^2-r^2}$ states represents a measure of the local JT tetragonal distortion affecting octahedral units. Therefore, two important conclusions are drawn:

1. **both Mg-CNCZ and CNCZ samples suffer from tetragonal distortion**, since $d_{3z^2-r^2}$ states are roughly 1 eV more energetic than the core-hole ground state $d_{x^2-y^2}$ (elastic peak);

2. **CNCZ octahedral units are more distorted than Mg-CNCZ units**, since

$d_{3z^2-r^2}$ states in CNCZ are blue-shifted with respect to Mg-CNCZ $d_{3z^2-r^2}$ states.

These are qualitative considerations. In order to provide a quantitative estimate of the JT distortion a curve fitting procedure has been made and is here reported.
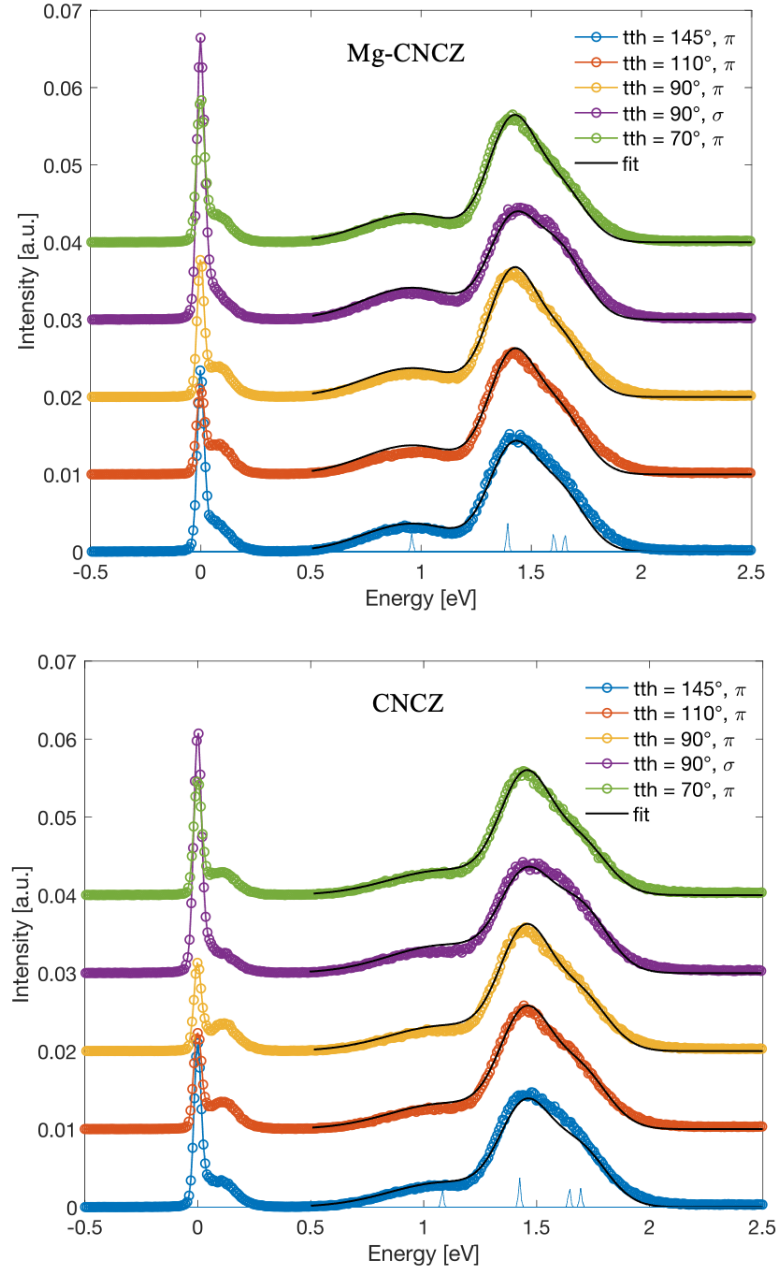


Figure 3.5: Global fit to $dd$ excitations. The blue small peaks included in the bottom of the panels have the purpose to indicate the positions of Gaussian functions.

We have fitted $dd$ excitations including simultaneously RIXS spectra at all experimental configurations, using four Gaussian functions to reproduce $d_{3z^2-r^2}$, $d_{xy}$, $d_+$ and $d_-$

contributions. The analysis on the polarization and scattering angle dependencies, combined with the results of calculated cross sections (Fig. 2.6), has been exploited to assign experimental features to specific $dd$ transitions. The relative intensity of the Gaussian functions was forced to be proportional to the RIXS cross sections we presented in section 2.2.4. In total, the spectra have been fitted using six parameters corresponding to the energy and FWHMs of $dd$ excitations. Results are shown in Fig. 3.5, where the global fits faithfully reproduce the $dd$ features. The energy of $d$ states extracted by the fit are listed in Tab. 3.2. The quantity $\Delta_{dd}$ is the difference between the energies of $d_{3z^2-r^2}$ in CNCZ and Mg-CNCZ.

|  | Mg-CNCZ | CNCZ | $\Delta_{dd}$ [eV] |
|---|---|---|---|
| $E_{3z^2-r^2}$ [eV] | 0.96 | 1.08 | 0.12 |
| $E_{xy}$ [eV] | 1.39 | 1.42 | 0.03 |
| $E_{-}$ [eV] | 1.60 | 1.64 | 0.04 |
| $E_{+}$ [eV] | 1.65 | 1.69 | 0.04 |

Table 3.2: Energy of $d$ states extracted from the global fitting procedure.

From the curve-fitting procedure we estimate that $d_{3z^2-r^2}$ peak in CNCZ is blue-shifted by 0.12 eV with respect to Mg-CNCZ. A smaller shift is also observed for the $d_{xy}$, $d_{-}$ and $d_{+}$ peaks.

In order to provide a complete description of the electronic excitations in RIXS spectra, we report here a qualitative analysis of CT excitations, based on LF theory. As seen from Fig. 3.6, where the RIXS intensity has been normalized to their area, CT excitations are very weak compared to $dd$ excitations, although they extend in a larger energy range, roughly from 2.1 eV to 8 eV. RIXS spectra show little variations upon changes of scattering geometry and incident photon polarization. Visible differences can be found by comparing experimental results from the two samples (Fig. 3.7). The CT broad peak at approximately 2.5 eV in CNCZ is shifted towards higher energies in Mg-CNCZ. Moreover, the feature spanning from 5 eV to 7 eV is weaker in CNCZ than in Mg-CNCZ.

In LF theory electronic states have both a $p$-like and a $d$-like character, i.e., they are hybridized molecular states and RIXS excitations are interpreted as transitions from the bonding ground state to either anti-bonding states or other bonding states. Specifically, transitions to other bonding states represent $dd$ excitations, while transitions to anti-bonding states represent CT excitations.
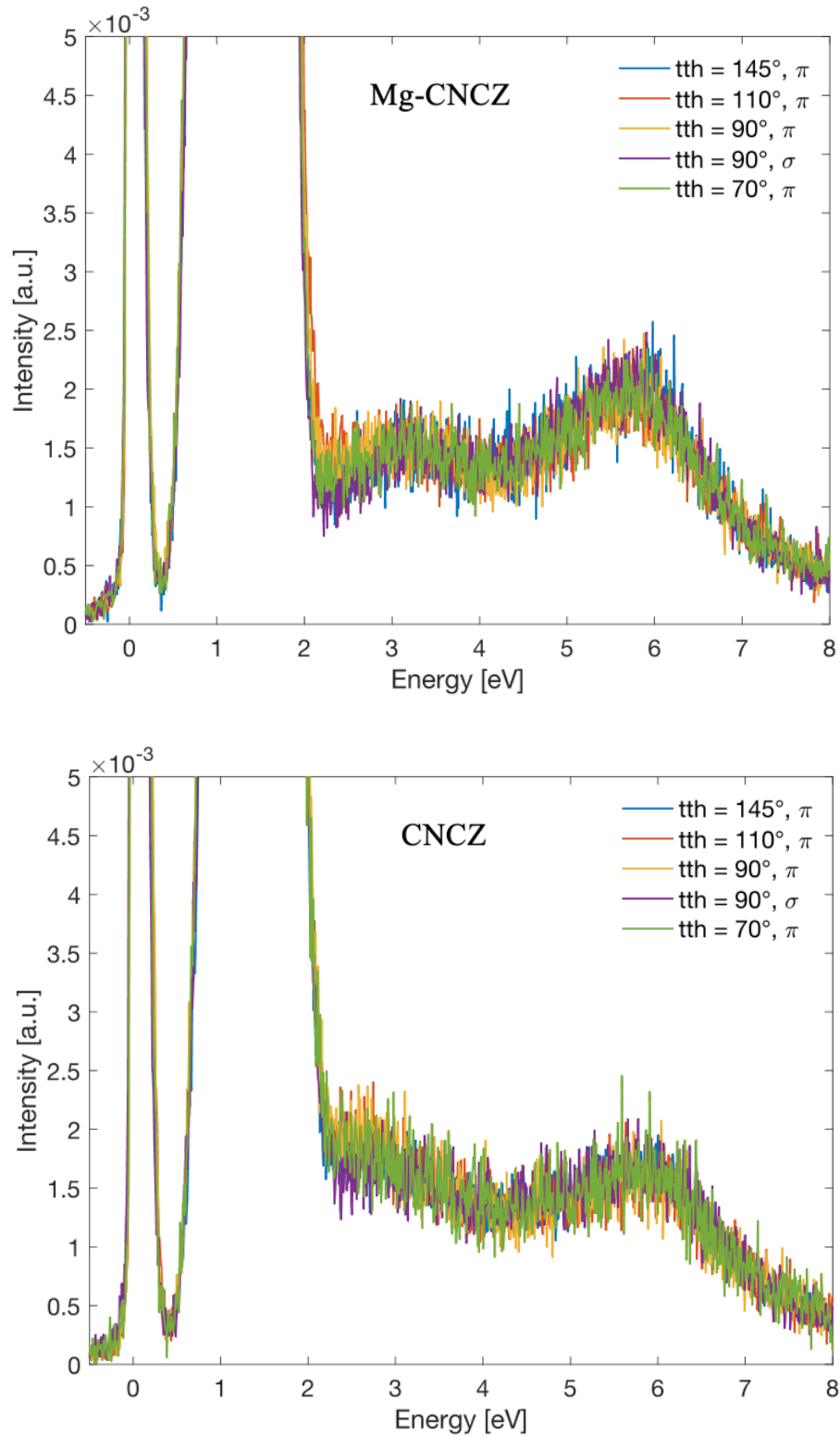
Figure 3.6: CT excitations in Mg-CNCZO (upper panel) and CNCZ (lower panel).

It is of common knowledge that the energy difference between bonding states and anti-

bonding states is roughly proportional to overlap integrals, since the strength of the overlap is a measure of the bonding states stabilization. That said, the blue-shift of the $d_{3z^2-r^2}$ and the red-shift of the CT feature in CNCZ could arise from an energy difference between bonding and anti-bonding states involving apical oxygens smaller than in Mg-CNCZ.
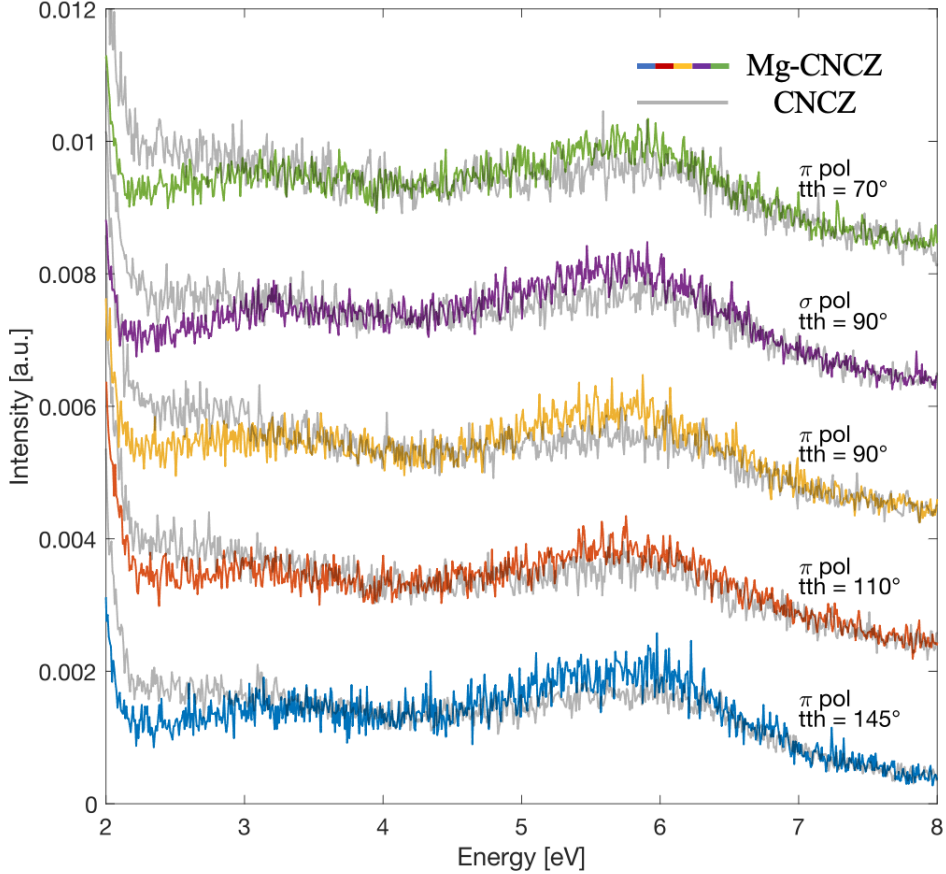


Figure 3.7: Comparison of normalized CT excitations in Mg-CNCZ and CNCZ, for all experimental configurations.

Consequently, in CNCZ the overlap integrals involving $2p$ orbitals of apical $O^{2-}$ ions and the $3d_{3z^2-r^2}$ orbital of Cu should be smaller than in Mg-CNCZ, consistent with a larger JT distortion.

As a final remark on CT excitations, we note that their intensity is much smaller than in cuprates. Indeed, while the intensity of CT excitations is a good fraction of that of $dd$ excitations in cuprates [58], they are almost invisible in HEOs. Given that CT excitations are attributed to the $d$-like character of anti-bonding states, it can be concluded that Mg-CNCZ and CNCZ are characterized by a smaller covalent character than cuprates.

## 3.3.   Magnetic excitations

The present section focuses on the analysis of the low-energy feature found in RIXS spectra at roughly 0.1 eV. We anticipate that, given that the low-energy region of RIXS spectra of cuprates is characterized by magnon-related peaks, and that Mg-CNCZ exhibits anti-ferromagnetic order, we interpret the low-energy feature as a sign of the presence of magnetic excitations. In other words, the peak arises from a spin-flip excitation and involves the $d_{x^2-y^2,\downarrow} \rightarrow d_{x^2-y^2,\uparrow}$ transition. Hence, the position of the peak is characteristic of the magnon energy, i.e., the energy required to flip one spin in the long-range magnetically ordered background.

### 3.3.1.   Analysis of the magnetic peak

Fig. 3.8 shows a comparison of magnetic features in our HEOs samples for all experimental configurations. The most relevant experimental observation is that the energy of the magnetic feature is systematically larger in CNCZ than in Mg-CNCZ.
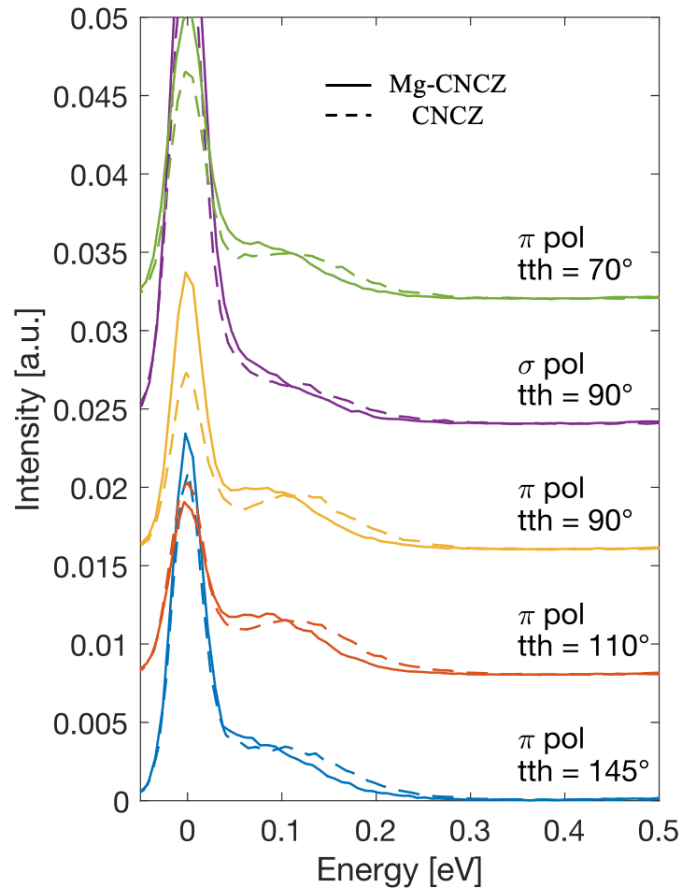


Figure 3.8: Comparison between magnetic excitations in HEO samples.

To quantify this observation, we have fitted the low-energy region of the spectra to two Gaussian functions, whose parameters are left free. Results of the fitting procedure are shown in Fig. 3.9, and the extracted parameters are listed in table 3.3, where $E^{sf}_{Mg-CNCZ}$ and $E^{sf}_{CNCZ}$ are the magnetic excitation energies of Mg-CNCZ and CNCZ, respectively.
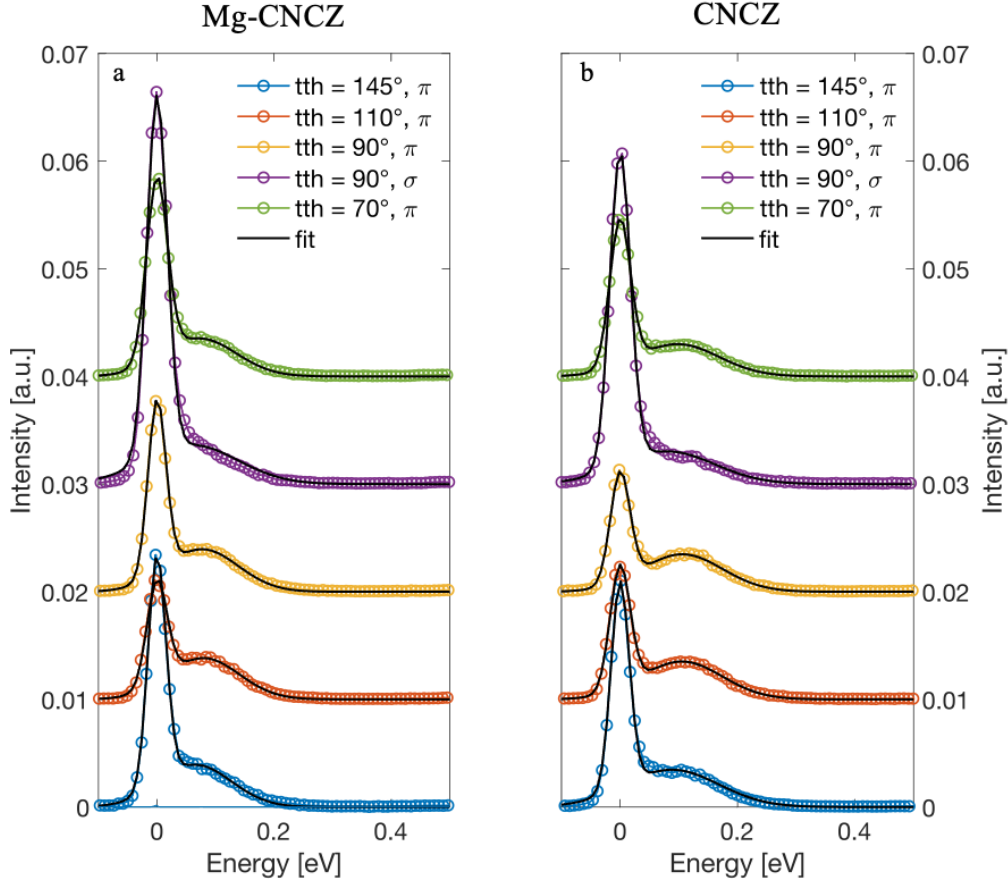


Figure 3.9: Analytical fits to the low-energy region for Mg-CNCZ spectra (panel $a$) and CNCZ spectra (panel $b$).

| | $E^{sf}_{Mg-CNCZ}$ [meV] | $E^{sf}_{CNCZ}$ [meV] | $E^{sf}_{Mg-CNCZ}/E^{sf}_{CNCZ}$ |
|---|---|---|---|
| $2\theta = 145°, \pi$ | 67 | 88 | 0.76 |
| $2\theta = 110°, \pi$ | 79 | 104 | 0.76 |
| $2\theta = 90°, \pi$ | 79 | 105 | 0.75 |
| $2\theta = 90°, \sigma$ | 59 | 72 | 0.82 |
| $2\theta = 70°, \pi$ | 72 | 97 | 0.74 |

Table 3.3: Spin-flip excitation energies obtained by fitting the elastic and the magnetic peaks. The magnetic energy ratio $E^{sf}_{Mg-CNCZ}/E^{sf}_{CNCZ}$ is also reported.

The table shows that the magnetic excitation energy is systematically higher in CNCZ than in Mg-CNCZ. Moreover, their ratio is roughly independent on the experimental geometry or incident photon polarization and averages to 0.77, i.e., close to 4/5. The sizeable variations of the magnetic energy upon changes in the scattering angle is better appreciated in Fig. 3.10 and is suggestive of a momentum dependence of the magnetic excitation.
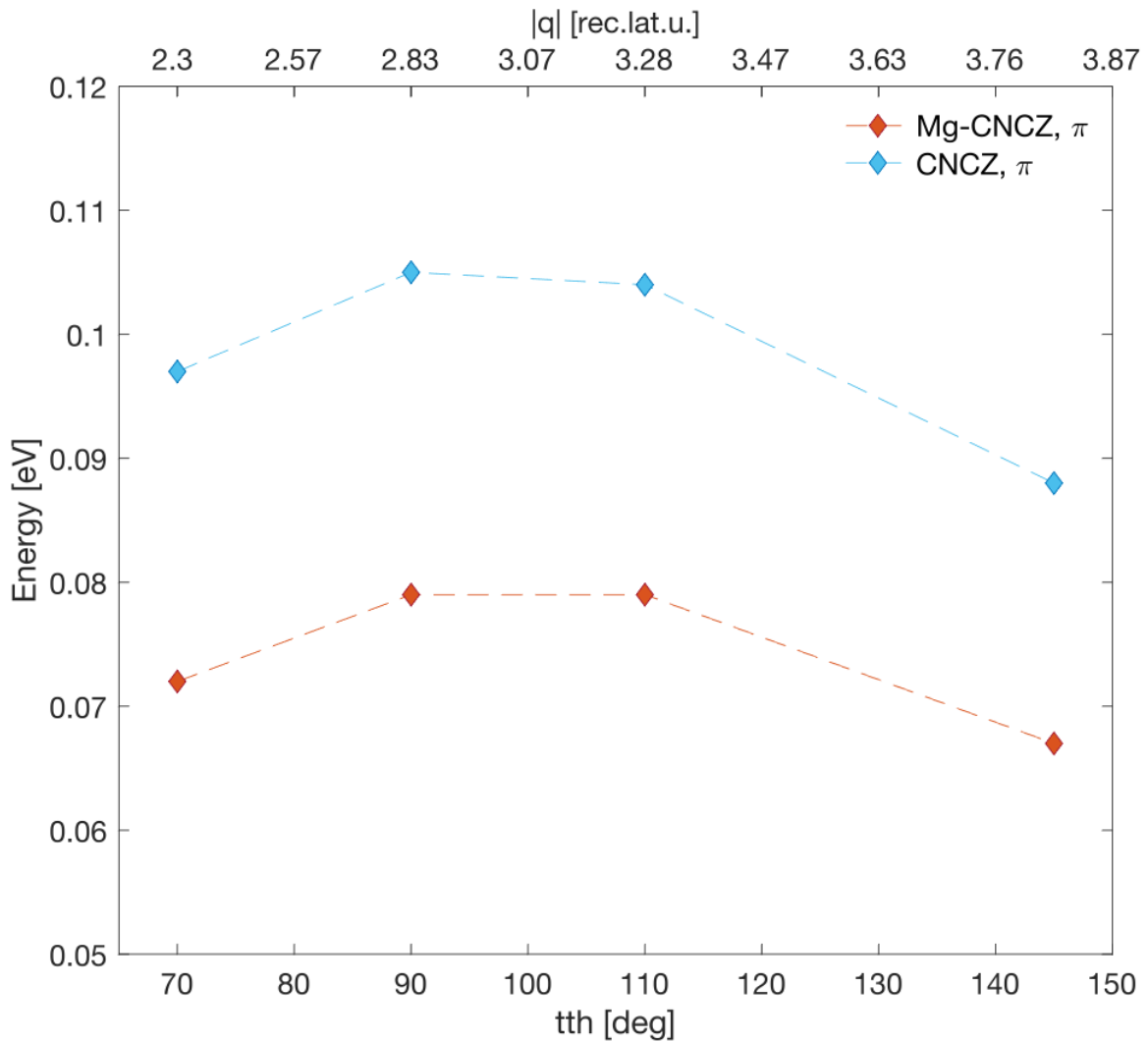


Figure 3.10: Magnetic dispersion in Mg-CNCZ (blue markers) and CNCZ (orange markers) samples. The trend is highlighted by dashed lines.

The dispersion is shown for $\pi$ in-going photon polarization, where measurements at distinct scattering angles are available. As observed, the magnon dispersion is clear and is similar for both samples.

## 3.3.2.    Nature of the magnetic excitation

The magnetic peak shift observed in Fig. 3.8 can be interpreted as it follows. Since in CNCZ the Mg non-magnetic ion is missing, the average spin momentum is larger than in Mg-CNCZ, and so are the strength of the exchange interaction acting on spins and the energy required to flip one spin. This interpretation is supported by quantitative arguments based on the electronic configurations and the magnetic moments of the ions present in Mg-CNCZ and CNCZ, reported in table 3.4.

|           | Electronic configuration | $S$ |
|-----------|:------------------------:|:---:|
| $Mg^{2+}$ | [Ne]                     | 0   |
| $Co^{2+}$ | $[Ar]3d^7$               | $\frac{3}{2}$ |
| $Ni^{2+}$ | $[Ar]3d^8$               | 1   |
| $Cu^{2+}$ | $[Ar]3d^9$               | $\frac{1}{2}$ |
| $Zn^{2+}$ | $[Ar]3d^{10}$            | 0   |

Table 3.4: Electronic configuration and corresponding spin of divalent ions in Mg-CNCZ and CNCZ HEOs. We clarify that the spin of the Co ion $\left(\frac{3}{2}\right)$ is assumed in the high-spin configuration.

Indeed, interestingly, the energy ratio $E^{sf}_{Mg-CNCZ}/E^{sf}_{Mg-CNCZ}$ comes very close to the ratio of the average spin values of the magnetic ions in Mg-CNCZ and CNCZ, respectively:

$$\frac{\overline{S}_{Mg-CNCZ}}{\overline{S}_{CNCZ}} \simeq \frac{E^{sf}_{Mg-CNCZ}}{E^{sf}_{Mg-CNCZ}} \simeq \frac{4}{5} \tag{3.1}$$

where

$$\begin{aligned}
\overline{S}_{Mg-CNCZ} &= \frac{S_{Cu} + S_{Co} + S_{Ni} + S_{Zn} + S_{Mg}}{5} = \frac{3}{5} \\
\overline{S}_{Mg-CNCZ} &= \frac{S_{Cu} + S_{Co} + S_{Ni} + S_{Zn}}{4} = \frac{3}{4}
\end{aligned} \tag{3.2}$$

In order to further test the validity of this interpretation, we report here a more rigorous analysis. In a crystalline material, the magnetic energy is described by the Heisenberg Hamiltonian, which accounts for the interactions between all pairs of atoms:

$$\mathcal{H}_m = -\sum_{(i,j)} J_{i,j}\mathbf{S}_i \cdot \mathbf{S}_j \tag{3.3}$$

where $\mathbf{S}_i$, $\mathbf{S}_j$ and $J_{i,j}$ are the spin momenta and the exchange parameter of the $(i,\ j)$ pair of atoms. The explicit calculation of the exchange energy in HEOs is not straight-

forward, since one needs to account for the random distribution of both magnetic and non-magnetic ions over the magnetic lattice. Moreover, the chemical selectivity of RIXS contrasts with its ability to probe collective excitations in a highly chemically-disordered system and complicates the interpretation of the RIXS process. Here we consider two conceptually distinct scenarios:
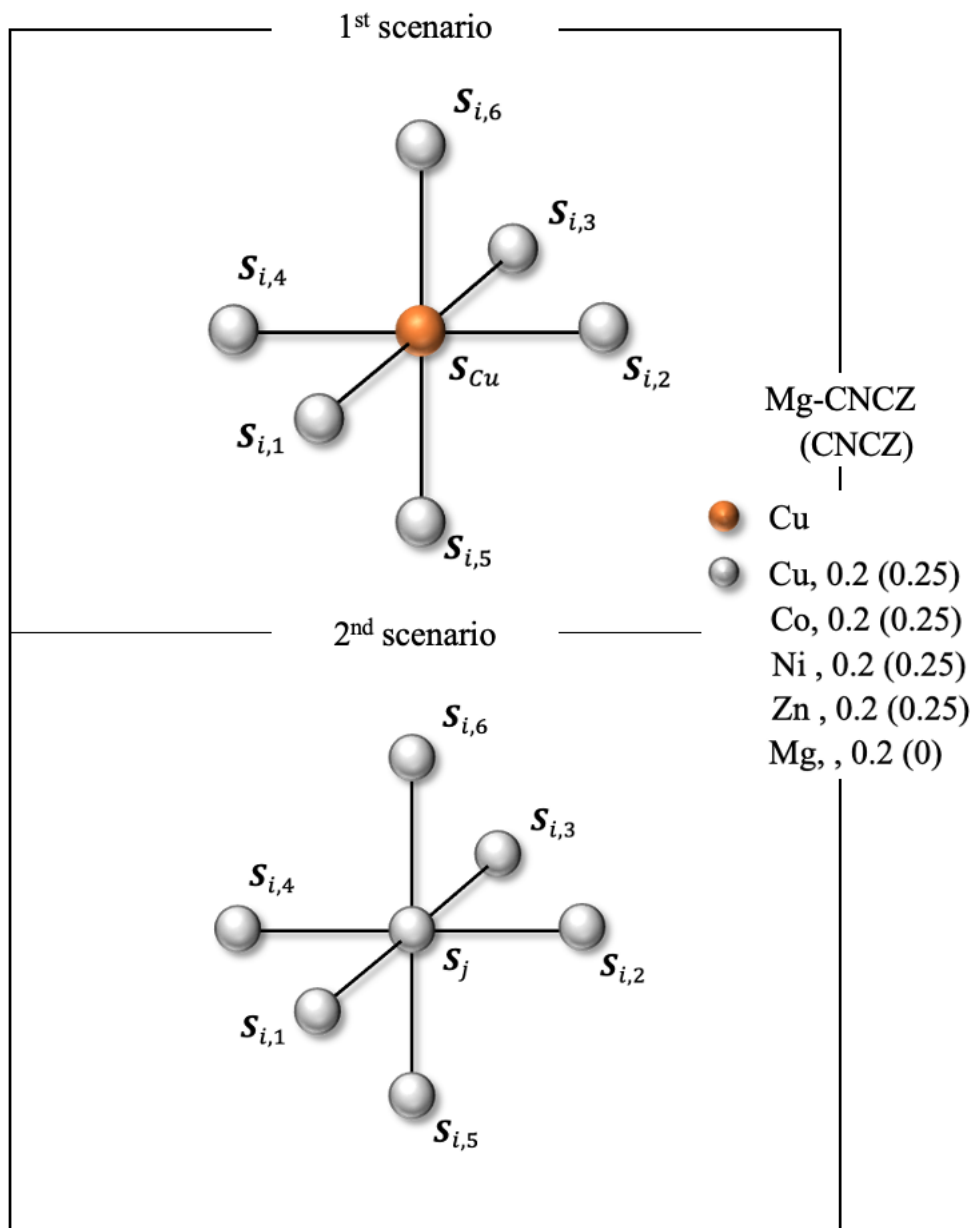


Figure 3.11: Schematics of the distribution of magnetic ions over the cationic sub-lattice in the two mentioned scenarios. Statistical weights are also reported for both HEOs.

**1$^{\text{st}}$ scenario**: here we assume that magnetic excitations involve spins of Cu$^{2+}$ ions only, because of the intrinsic chemical selectivity of the RIXS process. In this case, we limit to consider the Cu$^{2+}$ local environment to calculate the spin-flip energy. Specifically, since we address interactions mediated by oxygen ions, we refer to the 6 next-nearest neighbours in the cationic sub-lattice (upper panel of Fig. 3.11), which are randomly occupied by any of the ions available in the given sample, with equal probability. Hence, the energy of magnetic interaction between Cu$^{2+}$ and one of the surrounding ions is evaluated as the average of the interaction energies between Cu$^{2+}$ and each of the ions. The average is weighted by the probability $p_i$ of occupation of one neighbouring lattice site by an ion of the species $i$, with spin $S_i$. Then, to account for all neighbouring ions, a factor 6 is included. One obtains

$$E^{sf} = 6 \left[ 2S_{Cu} \sum_i^N p_i J_{Cu,i} S_i \right], \tag{3.4}$$

$N$ is the number of species in the sample, while $J_{Cu,i}$ is the exchange parameter of the interaction between Cu$^{2+}$ and species $i$. In Mg-CNCZ, $p_i = 0.2$ for all $N = 5$ available ionic species, while in CNCZ $N = 4$ and, correspondingly, $p_i = 0.25$. Hence, equation 3.7 develops differently for each sample:

$$\begin{aligned} E^{sf}_{Mg-CNCZ} &= 6 \left[ 2 \cdot 0.2 S_{Cu} (J_{Cu,Cu} S_{Cu} + J_{Cu,Co} S_{Co} + J_{Cu,Ni} S_{Ni}) \right] \\ E^{sf}_{Mg-CNCZ} &= 6 \left[ 2 \cdot 0.25 S_{Cu} (J_{Cu,Cu} S_{Cu} + J_{Cu,Co} S_{Co} + J_{Cu,Ni} S_{Ni}) \right] \end{aligned} \tag{3.5}$$

We note that all above terms involve Cu$^{2+}$ ions, in agreement with the assumption that the spin wave propagates over Cu$^{2+}$ sites only. Finally, the ratio between excitation energies is

$$\frac{E^{sf}_{Mg-CNCZ}}{E^{sf}_{CNCZ}} = \frac{0.2 S_{Cu} (J_{Cu,Cu} S_{Cu} + J_{Cu,Co} S_{Co} + J_{Cu,Ni} S_{Ni})}{0.25 S_{Cu} (J_{Cu,Cu} S_{Cu} + J_{Cu,Co} S_{Co} + J_{Cu,Ni} S_{Ni})} = \frac{4}{5}, \tag{3.6}$$

which correctly reproduce the experimental observation.

**2$^{\text{nd}}$ scenario**: here we assume that magnetic excitation involve the spins of all magnetic ions, because of the intrinsic collective nature of magnons. The site that we conceptually identified as the one hosting the spin flip is now hosting any of the $N$ available ions, with equal probability. The lower panel of Fig. 3.11 depicts the described framework, where $S_j$ is the spin of species $j$ occupying the central site. By changing species, $N$ distinct configurations can be identified. Thus, equation 3.7 must be further averaged over these

configurations:

$$E^{sf} = 6\left[2\sum_{j}^{N} p_j S_j \sum_{i}^{N} p_i J_{j,i} S_i\right] \tag{3.7}$$

Once again, the average is weighted by the probability $p_j$ that the central site is occupied by species $j$. Developing the summation for Mg-CNCZ and CNCZ, respectively, one obtains

$$
\begin{aligned}
E^{sf}_{Mg-CNCZ} &= 6\{2 \cdot 0.2[0.2 S_{Cu}(J_{Cu-Cu}S_{Cu} + J_{Cu-Co}S_{Co} + J_{Cu-Ni}S_{Ni}) + ... \\
&\quad ... + 0.2 S_{Ni}(J_{Ni-Cu}S_{Cu} + J_{Ni-Co}S_{Co} + J_{Ni-Ni}S_{Ni})]\} \\
E^{sf}_{CNCZ} &= 6\{2 \cdot 0.25[0.25 S_{Cu}(J_{Cu-Cu}S_{Cu} + J_{Cu-Co}S_{Co} + J_{Cu-Ni}S_{Ni}) + ... \\
&\quad ... + 0.25 S_{Ni}(J_{Ni-Cu}S_{Cu} + J_{Ni-Co}S_{Co} + J_{Ni-Ni}S_{Ni})]\}
\end{aligned}
\tag{3.8}
$$

Performing the ratio all terms cancel out, apart from the statistical weights:

$$\frac{E^{sf}_{Mg-CNCZ}}{E^{sf}_{CNCZ}} = \left(\frac{4}{5}\right)^2 \tag{3.9}$$

According to our derivations, we conclude that the first scenario seems to be the correct one, i.e., the energy of the spin wave is that of the magnetic excitation involving $Cu^{2+}$ ions only. This might be due to the coherence of the RIXS process that effectively probes only the chemical species at resonance.

### 3.3.3. Study of the magnon dispersion

The study here proposed aims at predicting the observed magnetic dispersion by including the magnetic structure factor into calculated scattering cross sections. In this way, an estimate of the average exchange parameter $J$ is given within the hypothesis of coherent magnon excitation over Cu sites only. The magnetic structure factor, named $S_m$, includes the dependence on the transferred momentum $\mathbf{q}$ into the calculation of the intensity $I$ of the magnetic excitation. In particular, one can write

$$I(\mathbf{q}, E) \propto S_m(\mathbf{q}, E)\sigma_{x^2-y^2,\uparrow}, \tag{3.10}$$

where we recall that $\sigma_{x^2-y^2,\uparrow}$ represents the cross section of the spin-flip excitation. $S_m(\mathbf{q}, E)$ has been calculated adapting the work by Hutching and Samuelsen [85] to HEO powders. We anticipate that the structure factor is derived in the assumption that a unique exchange energy is associated to the magnetic interaction, mediated by O, be-

tween Cu and the magnetic ions:

$$J_{Cu-Cu}S_{Cu} = J_{Cu-Co}S_{Co} = J_{Cu-Ni}S_{Ni} = J\bar{S} \qquad (3.11)$$

That said, $S_m(\mathbf{q}, E)$ can be written as

$$S_m(\mathbf{q}, E) = \frac{A(\mathbf{q}, E) - B(\mathbf{q}, E)}{\sqrt{A(\mathbf{q}, E)^2 - B(\mathbf{q}, E)^2}}, \qquad (3.12)$$

where $A$ and $B$ are $\mathbf{q}$-dependent parameters proportional to $J$:

$$A(\mathbf{q}, E) = 6J$$
$$B(\mathbf{q}, E) = 2JC(\mathbf{q}, E) \qquad (3.13)$$
$$C = \cos aq_x + \cos aq_y + \cos aq_z$$

$a$ is the crystal lattice parameter, while $q_x$, $q_y$ and $q_z$ are the projections of $\mathbf{q}$ on the sample frame of reference.

The $\mathbf{q}$-dependence of the magnon energy is instead implemented by means of the following dispersion relation, which makes use of the same $A$ and $B$ parameters above defined:

$$\hbar\omega(\mathbf{q}) = S_{Cu}\bar{S}\sqrt{A(\mathbf{q}, E)^2 - B(\mathbf{q}, E)^2} \qquad (3.14)$$

$\bar{S}$ is the average spin of the magnetic ions, equal to 0.3 in Mg-CNCZ and to 0.375 in CNCZ.

Now we have all the tools to simulate the HEOs magnon dispersion. The idea is to leave $J$ as a free parameter, with the aim to match the simulated dispersion to the experimental data shown in Fig. 3.10. The results of the calculated dispersion are visualized in Fig. 3.12, together with reported experimental points (diamond markers), both for Mg-CNCZ and CNCZ. Simulations appear to well reproduce the experimental trend. The average exchange parameter is estimated to be approximately 22 meV, that is an order of magnitude larger than theoretical estimates [55]. However, this discrepancy may be related to the element selectivity of the RIXS technique: while the proposed theoretical work estimates $J$ as an average of the exchange parameters associated to interactions involving any couple of magnetic ions ($J_{Cu-Cu}$, $J_{Cu-Co}$, $J_{Cu-Ni}$, $J_{Co-Ni}$, $J_{Co-Co}$ and $J_{Ni-Ni}$), we likely measure an exchange parameter averaged uniquely over interactions involving copper ions, the species at resonance. This possibility calls for further investigations in the future: RIXS measurements at other absorption edges could be performed to check the possible dependence of the measured $J$ on the particular probed ion.
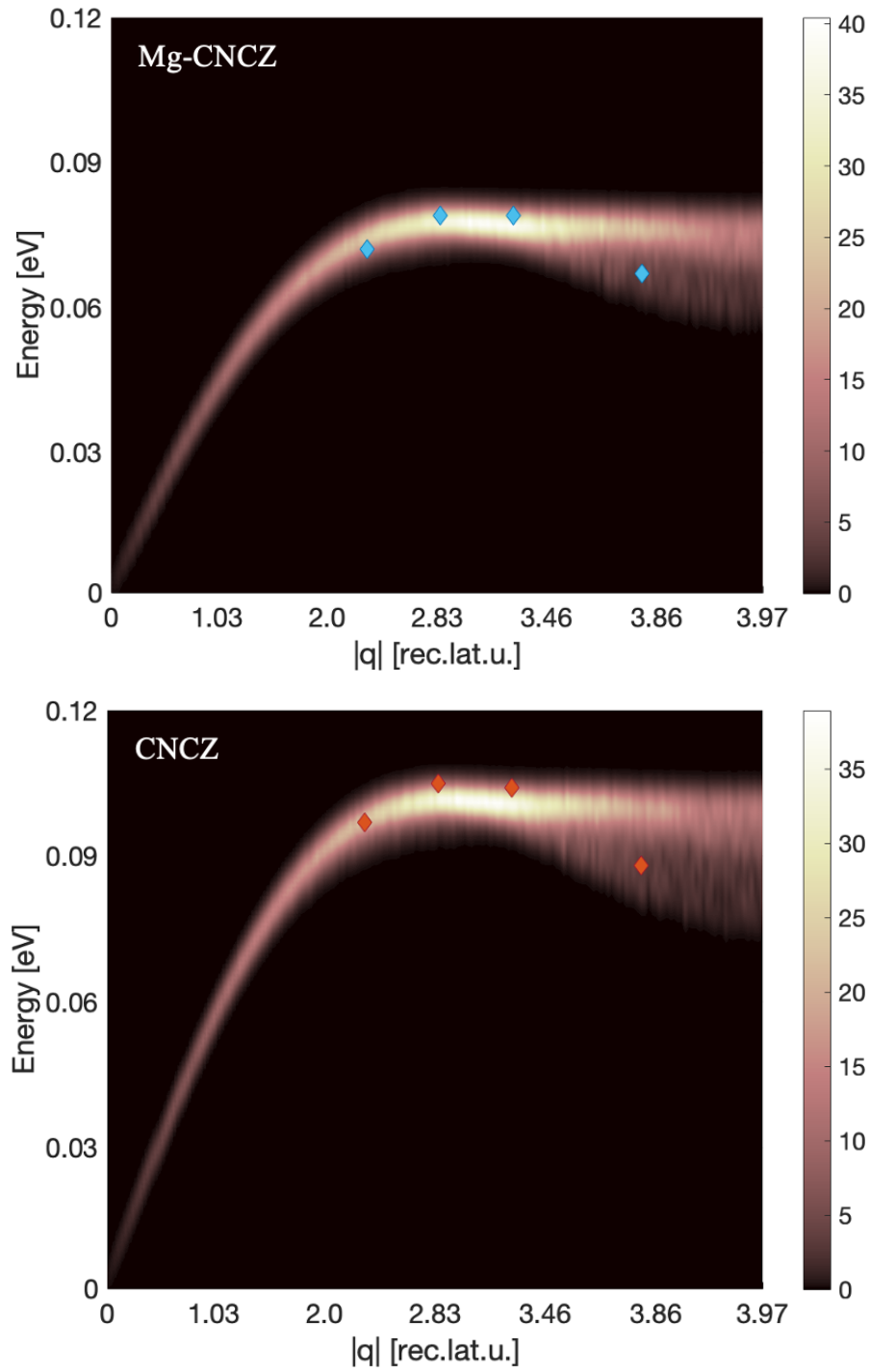
Figure 3.12: Simulated magnon dispersion in Mg-CNCZ (upper panel) and CNCZ (lower panel). The colour scale represents the value of $S_m(\mathbf{q}, E)\sigma_{x^2-y^2,\uparrow}$.

# 4 | Conclusions and Perspectives

Inspired by the growing interest in the family of HEOs, and motivated by the reliability of the RIXS technique on the study of transition metal oxides, we have performed RIXS measurements on two prototypical rock-salt HEOs, Mg-CNCZ and CNCZ, at the $L_3$ absorption edge of $Cu^{2+}$. By doing so, RIXS has been demonstrated, for the very first time, to be a powerful tool for probing their structural, electronic and magnetic properties. By analyzing $dd$ and charge-transfer excitations, we have established with certainty that $CuO_6$ octahedral units in Mg-CNCZ and CNCZ suffer from sizeable Jahn-Teller distortions. The possibility of a distortion that lowers the local symmetry of $Cu^{2+}$ sites from cubic to tetragonal was already observed from the refinement of the crystal structure in both samples, but a precise estimate of the energy associated to it could not be made. Here, we provide a direct measurement of the energy associated to the JT instability for both Mg-CNCZ (0.96) and CNCZ (1.08 eV). Moreover, the investigation of the low-energy spectral region has revealed that the relative energies of the magnetic peaks in the two systems is $\frac{4}{5}$, coinciding to the ratio between the average spin values of available elemental species in Mg-CNCZ and CNCZ: indeed, the extra non-magnetic ion found in the five-component HEO reduces the effective magnetic interaction, thus decreasing the spin-flip excitation energy. Within the framework of the Heisenberg model, and assuming that RIXS coherently excites spin waves at resonant sites only, we have developed a more formal derivation of the factor $\frac{4}{5}$, reproducing the experimental evidence. Finally, we have explained the momentum dependence of the magnetic excitations by including the magnetic structure factor $S_m(\mathbf{q}, E)$ in the calculations for the magnetic excitation intensity, together with a proper expression for the energy dispersion relation $\hbar\omega(\mathbf{q})$. By doing so, we have quantified the effective anti-ferromagnetic coupling $J$ to approximately 22 meV. A more solid interpretation of the magnetic behaviour of HEOs, however, calls for further investigations. To test the validity of our interpretation of the RIXS process on these magnetically disordered materials it could be interesting to perform RIXS at the absorption edges of other elemental species. In addition, temperature-dependent measurements could be relevant to improve our understanding of their magnetic properties. In conclusion, we have demonstrated that RIXS is capable of providing a plenitude of

novel information about prototypical Mg-CNCZ and CNCZ compounds, and we believe that it can be a relevant technique also for studying other related compounds, with the aim to fully explore the emergent realm of HEOs.

# A | Appendix

## A.1. Kramers-Heisenberg equation

Here the Kramers-Heisenberg equation is derived, following the most relevant steps of the theoretical work by Ament [65]. The interaction between the scattering x-rays and the solid sample is described by quantum electrodynamics (QED). To simplify the theoretical treatment, we work under two relevant assumptions:

- the Hamiltonian of the whole system is derived in the low-energy approximation of QED: the electrons interacting with the quantized electromagnetic field describing scattering x-ray photons are assumed to be **non-relativistic** electrons i.e. electrons moving at speeds much smaller than the speed of light $c$;

- the electromagnetic fields involved in the light-matter interaction event are much smaller than the mass $m$ of the electron. If $\mathbf{A}(\mathbf{r}, t)$ is the vector potential of the electromagnetic field and $\Phi$ is the scalar potential, the following relations must be satisfied:

$$\frac{e|\mathbf{A}(\mathbf{r}, t)|}{2mc} \ll 1 \tag{A.1}$$

$$\frac{e\Phi}{2mc^2} \ll 1 \tag{A.2}$$

In this framework, the Hamiltonian describing the interaction of $N$ electrons with the electromagnetic field is

$$\mathcal{H} = \sum_{j=1}^{N} \frac{[\mathbf{p}_j + e\mathbf{A}(\mathbf{r}_j)]^2}{2m} - \sum_{j=1}^{N} e\Phi(\mathbf{r}_j) - \frac{e\hbar}{2mc} \sum_{j=1}^{N} \boldsymbol{\sigma}_j \cdot \nabla \times \mathbf{A}(\mathbf{r}) +$$

$$+ \sum_{j=1}^{N} \frac{e\hbar}{2(2mc)^2} \boldsymbol{\sigma}_j \cdot \{\mathbf{E}(\mathbf{r}_j) \times [\mathbf{p}_j + e\mathbf{A}(\mathbf{r}_j)] - [\mathbf{p}_j + e\mathbf{A}(\mathbf{r}_j)] \times \mathbf{E}(\mathbf{r}_j)\} + \tag{A.3}$$

$$+ \sum_{j=1}^{N} \frac{e\hbar^2 \rho(\mathbf{r}_j)}{8(mc)^2 \epsilon_0} + \int d\mathbf{k} \sum_{\boldsymbol{\epsilon}} \hbar\omega_{\mathbf{k}} \left( c_{\boldsymbol{\epsilon}, \mathbf{k}}^{\dagger} c_{\boldsymbol{\epsilon}, \mathbf{k}} + \frac{1}{2} \right)$$

where $\boldsymbol{\sigma}_j$ and $\mathbf{p}_j$ are the Pauli matrices and the momentum operator of the $j^{th}$ electron at site $j$, $\mathbf{E}(\mathbf{r}_j) = -\nabla\phi(\mathbf{r}) - \frac{\partial \mathbf{A}(\mathbf{r})}{\partial t}$ is the electric field, $c^{\dagger}_{\boldsymbol{\epsilon},\mathbf{k}}$ is the creation operator of a photon with wavevector $\mathbf{k}$ and polarization state $\boldsymbol{\epsilon}$ and $c_{\boldsymbol{\epsilon},\mathbf{k}}$ is the corresponding annihilation operator. $\varepsilon_0$ is the permittivity of free space. The first term of $\mathcal{H}$ is the kinetic energy of the $N$ electrons in presence of an electromagnetic field. The second term denotes the potential energy of the system, while the third term describes Zeeman splitting in the presence of a magnetic field $\mathbf{B}(\mathbf{r}) = \nabla \times \mathbf{A}(\mathbf{r})$. The effect of spin-orbit coupling is encompassed in the fourth term. The fifth term is called Darwin term and is a correction term acting on $s$ states only. Finally, the last term describes the energy of the electromagnetic field as sum of all photon modes $(\mathbf{k}, \boldsymbol{\epsilon})$.

At this point it is useful to highlight that equation A.3 can be reformulated by gathering all terms in 3 contributions:

$$\mathcal{H} = \mathcal{H}_{el} + \mathcal{H}_{ph} + \mathcal{H}' \tag{A.4}$$

$\mathcal{H}_{el}$ contains all terms describing the energy of electrons, $\mathcal{H}_{ph}$ gathers terms related solely to the energy of the radiation field and $\mathcal{H}'$ is the electron-photon interaction Hamiltonian. In the context of perturbation theory, $\mathcal{H}'$ represents a perturbing term to the system of non-interacting electrons and photons, described by the Hamiltonian $\mathcal{H}_0 = \mathcal{H}_{el} + \mathcal{H}_{ph}$. The eigenstates of $\mathcal{H}_{ph}$ are single-photon states identified by momentum, energy and polarization state. If the initial and final eigenstates of the scattered photon are $|\mathbf{k}_i, \boldsymbol{\epsilon}_i\rangle$ and $|\mathbf{k}_o, \boldsymbol{\epsilon}_o\rangle$, respectively, the following eigenvalue equations are satisfied:

$$\mathcal{H}_{ph}|\mathbf{k}_i, \boldsymbol{\epsilon}_i\rangle = \hbar\omega_{\mathbf{k}_i}|\mathbf{k}_i, \boldsymbol{\epsilon}_i\rangle \tag{A.5}$$

$$\mathcal{H}_{ph}|\mathbf{k}_o, \boldsymbol{\epsilon}_o\rangle = \hbar\omega_{\mathbf{k}_o}|\mathbf{k}_o, \boldsymbol{\epsilon}_o\rangle \tag{A.6}$$

The energy and the momentum of the photon are linked by the simple relation $\omega_{\mathbf{k}_i} = c|\mathbf{k}_i|$. As a result of the scattering process the solid transits from an initial state $|i\rangle$ with energy $E_i$ to a final state $|f\rangle$ with energy $E_f$. $|i\rangle$ and $|f\rangle$ are both eigenfunctions of $\mathcal{H}_{el}$:

$$\mathcal{H}_{el}|i\rangle = E_i|i\rangle \tag{A.7}$$

$$\mathcal{H}_{el}|f\rangle = E_f|f\rangle \tag{A.8}$$

Since $\mathcal{H}_0$ contains only non-interacting terms, the eigenstates of the unperturbed Hamiltonian $\mathcal{H}_0$ are obtained simply by multiplying eigenstates of $\mathcal{H}_{el}$ to eigenstates of $\mathcal{H}_{ph}$. Moreover, eigenvalues are obtained by summing eigenvalues of $\mathcal{H}_{el}$ to eigenvalues of $\mathcal{H}_{ph}$. That said, we have all ingredients to fully characterize the initial and final states of the pro-

cess: the system transits from the ground state $|a\rangle = |i; \mathbf{k}_i, \boldsymbol{\epsilon}_i\rangle$ with energy $E_a = E_i + \hbar\omega_{\mathbf{k}_i}$ to the final state $|b\rangle = |f; \mathbf{k}_o, \boldsymbol{\epsilon}_o\rangle$ with energy $E_b = E_f + \hbar\omega_{\mathbf{k}_o}$. The relations shown hereunder are fullfilled:

$$\mathcal{H}_0|a\rangle = E_a|a\rangle \tag{A.9}$$

$$\mathcal{H}_0|b\rangle = E_b|b\rangle \tag{A.10}$$

To calculate the scattering cross section we rely on perturbation theory: the transition rate $w$ for RIXS processes is given by second order Fermi's Golden Rule:

$$w = \frac{2\pi}{\hbar} \sum_b \left| \langle b|\mathcal{H}'|a\rangle + \sum_n \frac{\langle b|\mathcal{H}'|n\rangle\langle n|\mathcal{H}'|a\rangle}{E_a - E_n} \right|^2 \delta(E_b - E_a) \tag{A.11}$$

$n$ is an index running on the intermediate states of a second order process, such as RIXS, that are eigenstates of the unperturbed Hamiltonian $\mathcal{H}_0$. The $n^{th}$ intermediate state has energy $E_n$ and the Dirac delta $\delta(E_b - E_a)$ ensures conservation of energy. While the first order amplitude yields non-resonant scattering processes, the second order amplitude is a resonant term; it dominates the first order amplitude when $E_a \simeq E_n$, a condition that is achieved when the incoming photon energy matches one of the material absorption edges. At this point it is useful to recall that the vector potential $\mathbf{A}(\mathbf{r})$ can be developed as sum of single mode vector potentials:

$$\mathbf{A}(\mathbf{r}) = \int d\mathbf{k} \sum_{\boldsymbol{\epsilon}} \mathbf{A}_{\boldsymbol{\epsilon},\mathbf{k}}(\mathbf{r}) \tag{A.12}$$

where

$$\mathbf{A}_{\boldsymbol{\epsilon},\mathbf{k}}(\mathbf{r}) = \sqrt{\frac{\hbar}{2V\varepsilon_0\omega_{\mathbf{k}}}} \boldsymbol{\epsilon} \left( c_{\boldsymbol{\epsilon},\mathbf{k}} e^{i\mathbf{k}\cdot\mathbf{r}} + c_{\boldsymbol{\epsilon},\mathbf{k}}^\dagger e^{-i\mathbf{k}\cdot\mathbf{r}} \right) \tag{A.13}$$

$V$ denotes the volume of the system. We underline that $\mathbf{A}_{\boldsymbol{\epsilon},\mathbf{k}}(\mathbf{r})$ is proportional to $c_{\boldsymbol{\epsilon},\mathbf{k}}$ and $c_{\boldsymbol{\epsilon},\mathbf{k}}^\dagger$: all terms of $\mathcal{H}'$ that are quadratic in $\mathbf{A}(\mathbf{r})$ contribute only to the first order amplitude of equation A.11, since they include terms proportional to $c_{\boldsymbol{\epsilon},\mathbf{k}}^\dagger c_{\boldsymbol{\epsilon},\mathbf{k}}$ and $c_{\boldsymbol{\epsilon},\mathbf{k}} c_{\boldsymbol{\epsilon},\mathbf{k}}^\dagger$. In other words, terms quadratic in $\mathbf{A}(\mathbf{r})$ give rise to non-resonant processes, such as non-resonant inelastic scattering or Bragg x-ray diffraction. Since RIXS is a second order process, in the following we exclusively focus on the terms linear in $\mathbf{A}(\mathbf{r})$, which instead contribute to the second order amplitude and lead to resonant processes. The first order amplitude is neglected, being dominated by the second order term in the resonance condition intrinsic to the RIXS technique. Furthermore, off-resonance processes contributing to the second

order term are ignored [86]. If we neglect spin-orbit coupling, and choosing the Coulomb gauge so that $\nabla \cdot \mathbf{A}(\mathbf{r}) = 0$, the perturbation Hamiltonian becomes

$$\mathcal{H}' \simeq -\frac{e}{mc} \sum_j \mathbf{A}(\mathbf{r}_j) \cdot \mathbf{p}_j - \frac{e\hbar}{mc} \sum_j \boldsymbol{\sigma}_j \cdot \nabla \times \mathbf{A}(\mathbf{r}_j) \tag{A.14}$$

In a RIXS experiment exploiting soft x-rays we can assume to work in the dipole approximation limit. The wavelength of the electromagnetic field is much larger than the typical spatial extension of atomic wavefunctions ($\mathbf{k} \cdot \mathbf{r} \ll 1$) and $e^{i\mathbf{k} \cdot \mathbf{r}}$ is assumed to be approximately constant and equal to 1. Under this assumption, replacing $\mathcal{H}'$ in equation A.11 leads to the following expression of the second order amplitude:

$$\frac{e^2\hbar}{2m^2V\varepsilon_0\sqrt{\omega_{\mathbf{k}_i}\omega_{\mathbf{k}_o}}} \sum_n \sum_{j,j'}^N \frac{\langle f|\boldsymbol{\epsilon}_o^* \cdot \mathbf{p}_{j'}|n\rangle\langle n|\boldsymbol{\epsilon}_i \cdot \mathbf{p}_j|g\rangle}{E_g + \hbar\omega_{\mathbf{k}_i} - E_n + i\Gamma_n} \tag{A.15}$$

The imaginary term $i\Gamma_n$ is introduced to account for the finite lifetime of the core holes generated in the intermediate states. Usually the transition operators in a RIXS process are rewritten exploiting the definitions

$$\mathcal{D}_i = \frac{1}{im\omega_{\mathbf{k}}} \sum_j^N e^{i\mathbf{k} \cdot \mathbf{r}_j} \boldsymbol{\epsilon} \cdot \mathbf{p}_j \tag{A.16}$$

and

$$\mathcal{D}_o = \frac{1}{im\omega_{\mathbf{k}}} \sum_{j'}^N e^{i\mathbf{k} \cdot \mathbf{r}_{j'}} \boldsymbol{\epsilon} \cdot \mathbf{p}_{j'} \tag{A.17}$$

To calculate the double differential cross section $\frac{d^2\sigma}{d\hbar\omega d\Omega}$, the transition rate $w$ is multiplied by the density of photon states in the solid angle $\rho_{ph}$ and is divided by the photon flux $\Phi$: $\frac{d^2\sigma}{d\hbar\omega d\Omega} = \frac{w\rho_{ph}}{\Phi}$ [87]. Replacing the expressions A.15, A.16 and A.17 in equation A.11 we finally obtain the **Kramers-Heisenberg** equation

$$\frac{d^2\sigma}{d\hbar\omega d\Omega} = r_e^2 m^2 \omega_{\mathbf{k}_o}^3 \omega_{\mathbf{k}_i} \sum_f \left| \sum_n \frac{\langle f|\mathcal{D}_o^\dagger|n\rangle\langle n|\mathcal{D}_i|g\rangle}{E_g + \hbar\omega_{\mathbf{k}} - E_n + i\Gamma_n} \right|^2 \delta(E_g - E_f + \hbar\omega) \tag{A.18}$$

used to calculate the RIXS cross section. $r_e = \frac{e^2}{4\pi\varepsilon_0 mc^2}$ is the classical electron radius. The formula can be generalized accounting for the statistical distribution of electrons at finite

temperature $T$:

$$\frac{d^2\sigma}{d\hbar\omega d\Omega} \propto \sum_{i,f} \frac{1}{Z} e^{-E_i/k_B T} \left| \sum_n \frac{\langle f|\mathcal{D}_o^\dagger|n\rangle\langle n|\mathcal{D}_i|g\rangle}{E_g + \hbar\omega_{\mathbf{k}} - E_n + i\Gamma_n} \right|^2 \delta(E_g - E_f + \hbar\omega) \qquad \text{(A.19)}$$

where $k_B$ is the Boltzmann constant and $Z$ is the partition function.

## A.2.   Basis transformation matrices

We report here the matrices $\mathcal{T}_d$ and $\mathcal{T}_p$. They perform a basis transformation from the spherical harmonics basis to the cubic harmonics basis. The full expression of $\mathcal{T}_d$ is

$$
\begin{array}{c|ccccccccc}
 & Y_{2,2}^{\downarrow} & Y_{2,2}^{\uparrow} & Y_{2,1}^{\downarrow} & Y_{2,1}^{\uparrow} & Y_{2,0}^{\downarrow} & Y_{2,0}^{\uparrow} & Y_{2,\bar{1}}^{\downarrow} & Y_{2,\bar{1}}^{\uparrow} & Y_{2,\bar{2}}^{\downarrow} & Y_{2,\bar{2}}^{\uparrow} \\
\hline
d_{x^2-y^2}^{\downarrow} & \frac{1}{2}U_- & \frac{1}{2}D_- & 0 & 0 & 0 & 0 & 0 & 0 & \frac{1}{2}U_- & \frac{1}{2}D_- \\
d_{x^2-y^2}^{\uparrow} & \frac{1}{2}U_+ & \frac{1}{2}D_+ & 0 & 0 & 0 & 0 & 0 & 0 & \frac{1}{2}U_+ & \frac{1}{2}D_+ \\
d_{3z^2-r^2}^{\downarrow} & 0 & 0 & 0 & 0 & U_+ & D_+ & 0 & 0 & 0 & 0 \\
d_{3z^2-r^2}^{\uparrow} & 0 & 0 & 0 & 0 & U_- & D_- & 0 & 0 & 0 & 0 \\
d_{xy}^{\downarrow} & -\frac{i}{2}U_+ & -\frac{i}{2}D_+ & 0 & 0 & 0 & 0 & 0 & 0 & \frac{i}{2}U_+ & \frac{i}{2}D_+ \\
d_{xy}^{\uparrow} & -\frac{i}{2}U_- & -\frac{i}{2}D_- & 0 & 0 & 0 & 0 & 0 & 0 & \frac{i}{2}U_- & \frac{i}{2}D_- \\
d_{xz}^{\downarrow} & 0 & 0 & \frac{1}{2}U_+ & \frac{1}{2}D_+ & 0 & 0 & -\frac{1}{2}U_+ & -\frac{1}{2}D_+ & 0 & 0 \\
d_{xz}^{\uparrow} & 0 & 0 & \frac{1}{2}U_- & \frac{1}{2}D_- & 0 & 0 & -\frac{1}{2}U_- & -\frac{1}{2}D_- & 0 & 0 \\
d_{yz}^{\downarrow} & 0 & 0 & -\frac{i}{2}U_+ & -\frac{i}{2}D_+ & 0 & 0 & -\frac{i}{2}U_+ & -\frac{i}{2}D_+ & 0 & 0 \\
d_{yz}^{\uparrow} & 0 & 0 & -\frac{i}{2}U_- & -\frac{i}{2}D_- & 0 & 0 & -\frac{i}{2}U_- & -\frac{i}{2}D_- & 0 & 0 \\
\end{array}
$$

while $\mathcal{T}_p$ is

$$
\begin{array}{c|cccccc}
 & Y_{1,1}^{\downarrow} & Y_{1,1}^{\uparrow} & Y_{1,0}^{\downarrow} & Y_{1,1}^{\uparrow} & Y_{1,\bar{1}}^{\downarrow} & Y_{1,\bar{1}}^{\uparrow} \\
\hline
p_{\frac{3}{2},\frac{3}{2}} & 1 & 0 & 0 & 0 & 0 & 0 \\
p_{\frac{3}{2},\frac{1}{2}} & 0 & \sqrt{\frac{1}{3}} & \sqrt{\frac{2}{3}} & 0 & 0 & 0 \\
p_{\frac{3}{2},\bar{\frac{1}{2}}} & 0 & 0 & 0 & \sqrt{\frac{2}{3}} & \sqrt{\frac{1}{3}} & 0 \\
p_{\frac{3}{2},\bar{\frac{3}{2}}} & 0 & 0 & 0 & 0 & 0 & 1 \\
p_{\frac{1}{2},\frac{1}{2}} & 0 & \sqrt{\frac{2}{3}} & -\sqrt{\frac{1}{3}} & 0 & 0 & 0 \\
p_{\frac{1}{2},\bar{\frac{1}{2}}} & 0 & 0 & 0 & \sqrt{\frac{1}{3}} & -\sqrt{\frac{2}{3}} & 0 \\
\end{array}
$$
.

## A.3.   $\mathcal{H}_{MO_6}$ **Hamiltonian**

The 23×23 Hamiltonian describing the $CuO_6$ octahedral system is here reported.

$$
\mathcal{H}_{MO_6}
$$

# Acknowledgements

This thesis represents the conclusion of my course of study and its realization could only happen by virtue of the fundamental assistance of many people. First, I would like to show my sincere gratitude to my supervisor Prof. Marco Moretti. From the very beginning I admired his ability to compliment his indisputable professionalism to a formidable humour. I am grateful to have been able to benefit from his constant availability and his infinite patience.

I am also indebted to Prof. Giacomo Ghiringhelli, for giving me the opportunity to work on this thesis and for approaching me to the world of scientific research for the first time. I also thank all the other members of the PoliMiX group and beyond, who contributed to making me feel part of a real research group: Prof. Lucio Braicovich, Dr. Riccardo Arpaia, Roberto, Hao, Francesco, Giacomo and my thesis mates Maryia and Pietro.

Special thanks go to my lifelong friends Carmi, Sba, Curra, Versa, Ema, Alessia and Federica, for putting up with an infinite number of "non posso devo studiare", not so quickly replaced by "non posso devo scrivere", and for being able to lighten the heaviest days.

I would like to thank all friends that accompanied me throughout my course of study: Pisa, Gio and Tia, from the very first classes in the "spaccaculi" room; Fra and Fede, from groupmates to real friends; Sara, Pietro and Sara, for sharing lessons, coffees and physics discussions.

I extend my most sincere gratitude to Andrea, Sabrina, Giovanni, Marco and Sara, for considering me as part of their family from the first moment.

Special thanks go to Andrea, Erica, Simone, Elisa and my beautiful grandmother, from whom I have always received more than what I gave, unconditionally. A very special thank goes to Leo and Fede, whose noise during study hours is certainly more than compensated by the happiness they spread every day.

Thanks to my parents, for letting me follow my passion, for cultivating it and for showing me the most genuine form of love everyday.

Finally, to Gaia, I would like to say this: we know how much effort it took for us to achieve this goal; we shared everything, from moments of immense satisfaction to periods of disappointment and tiredness. More than anyone, you represented an unparalleled

source of strength and energy. For this and much more, I want to dedicate my thesis to you.

Milano, 5$^{th}$ October 2023

# List of Figures

# List of Tables

# Bibliography

[1] J.-W. Yeh, S.-K. Chen, S.-J. Lin, J.-Y. Gan, T.-S. Chin, T.-T. Shun, C.-H. Tsau, and S.-Y. Chang, Advanced Engineering Materials **6**, 299 (2004), https://onlinelibrary.wiley.com/doi/pdf/10.1002/adem.200300567 .

[2] B. Cantor, I. Chang, P. Knight, and A. Vincent, Materials Science and Engineering: A **375-377**, 213 (2004).

[3] B. L. Musicó, D. Gilbert, T. Z. Ward, K. Page, E. George, J. Yan, D. Mandrus, and V. Keppens, APL Mater **8** (2020), https://doi.org/10.1063/5.0003149.

[4] J. Gild, M. Samiee, J. L. Braun, T. Harrington, H. Vega, P. E. Hopkins, K. Vecchio, and J. Luo, Journal of the European Ceramic Society **38**, 3578 (2018).

[5] S. Jiang, T. Hu, J. Gild, N. Zhou, J. Nie, M. Qin, T. Harrington, K. Vecchio, and J. Luo, Scripta Materialia **142**, 116 (2018).

[6] Z. Sun, Y. Zhao, C. Sun, Q. Ni, C. Wang, and H. Jin, Chemical Engineering Journal **431**, 133448 (2022).

[7] S. Albedwawi, A. AlJaberi, G. Haidemenopoulos, and K. Polychronopoulou, Materials Design **202**, 109534 (2021).

[8] S. Aamlid, M. Oudah, J. Rottler, and A. Hallas, Journal of the American Chemical Society **145** (2023), https://doi.org/10.1021/jacs.2c11608.

[9] A. Dupuy, X. Wang, and J. Schoenung, Materials Research Letters **7**, 60 (2019).

[10] C. Rost, E. Sachet, T. Borman, A. Moballegh, E. Dickey, D. Hou, J. Jones, S. Curtarolo, and J.-P. Maria, Nature Communications **6**, 8485 (2015).

[11] A. Sarkar, R. Djenadic, D. Wang, C. Hein, R. Kautenburger, O. Clemens, and H. Hahn, Journal of the European Ceramic Society (2017), 10.1016/j.jeurceramsoc.2017.12.058.

[12] Z. Li, P. K G, Y. Deng, D. Raabe, and C. Tasan, Nature **534**, 227 (2016).

[13] D. Bérardan, S. Franger, D. Dragoe, A. Meena, and N. Dragoe, physica status solidi (RRL) - Rapid Research Letters **10**, 328–333 (2016).

[14] D. Bérardan, S. Franger, A. Meena, and N. Dragoe, Journal of Materials Chemistry A **4** (2016), 10.1039/C6TA03249D.

[15] R. J. Spurling, E. A. Lass, X. Wang, and K. Page, Phys. Rev. Mater. **6**, 090301 (2022).

[16] M. Brahlek, M. Gazda, V. Keppens, A. Mazza, S. McCormack, A. Mielewczyk-Gryń, B. Musicó, K. Page, C. Rost, S. Sinnott, C. Toher, T. Ward, and A. Yamamoto, (2022), 10.48550/arXiv.2208.12709.

[17] K. Chen, X. Pei, L. Tang, H. Cheng, Z. Li, C. Li, X. Zhang, and L. An, Journal of the European Ceramic Society **38**, 4161 (2018).

[18] C. Rost, Z. Rak, D. Brenner, and J.-P. Maria, Journal of the American Ceramic Society **100**, 2732 (2017).

[19] J. Sushil, A. Kumar, A. Gautam, and M. I. Ahmad, Materials Chemistry and Physics (2020), 10.1016/j.matchemphys.2020.124014.

[20] J. L. Braun, C. M. Rost, M. Lim, A. Giri, D. H. Olson, G. N. Kotsonis, G. Stan, D. W. Brenner, J.-P. Maria, and P. E. Hopkins, Advanced Materials **30**, 1805004 (2018), https://onlinelibrary.wiley.com/doi/pdf/10.1002/adma.201805004 .

[21] R. Liu, H. Chen, Z. Kunpeng, Y. Qin, B. Jiang, T. Zhang, G. Sha, X. Shi, C. Uher, W. Zhang, and L. Chen, Advanced Materials **29** (2017), 10.1002/adma.201702712.

[22] F. B. Lewis and N. H. Saunders, Journal of Physics C: Solid State Physics **6**, 2525 (1973).

[23] H. Xie, H. Lee, W. Youn, and M. Choi, Journal of Applied physics **94**, 4967 (2003).

[24] A. Slifka, B. Filla, and J. Phelps, Journal of Research of the National Institute of Standards and Technology **103** (1998), 10.6028/jres.103.021.

[25] P. Sahoo, D. Misra, G. Chaubey, J. Salvador, N. Takas, and P. P. Poudeu, MRS Proceedings **1256** (2011), 10.1557/PROC-1256-N06-21.

[26] X. Wu, J. Lee, V. Varshney, J. Wohlwend, A. Roy, and T. Luo, Scientific Reports **6**, 22504 (2016).

[27] A. Krivchikov and A. Jezowski, (2020).

[28] G. Instruments, G. Instruments, Complex impedance in Corrosion , 1 (2007).

[29] M. Balcerzak, K. Kawamura, R. Bobrowski, P. Rutkowski, and T. Brylewski, Journal of Electronic Materials **48** (2019), 10.1007/s11664-019-07512-z.

[30] D. J. Griffiths, *Introduction to Electrodynamics*, 4th ed. (Cambridge University Press, 2017).

[31] R. Serway, *Principles of Physics*, Principles of Physics No. v. 2 (Saunders College Pub., 1997).

[32] C. Brinker and G. Scherer, *Sol-Gel Science: The Physics and Chemistry of Sol-Gel Processing* (Elsevier Inc., United States, 2013) publisher Copyright: © 1990 Elsevier Inc. All rights reserved.

[33] Z. Feng and M. S. Seehra, Phys. Rev. B **45**, 2184 (1992).

[34] R. Kannan and M. S. Seehra, Phys. Rev. B **35**, 6847 (1987).

[35] S. Limpijumnong and W. R. L. Lambrecht, Phys. Rev. B **63**, 104103 (2001).

[36] A. Sarkar, R. Djenadic, N. J. Usharani, K. P. Sanghvi, V. S. Chakravadhanula, A. S. Gandhi, H. Hahn, and S. S. Bhattacharya, Journal of the European Ceramic Society **37**, 747 (2017).

[37] R. Shannon and C. Prewitt, Acta Crystallographica Section B Structural Crystallography and Crystal Chemistry **25**, 925 (1969).

[38] "General properties of zno," in *Zinc Oxide* (John Wiley Sons, Ltd, 2009) Chap. 1, pp. 1–76, https://onlinelibrary.wiley.com/doi/pdf/10.1002/9783527623945.ch1 .

[39] G. Tunell, E. Posnjak, and C. J. Ksanda, Journal of the Washington Academy of Sciences **23**, 195 (1933).

[40] J. Bularzik, P. Davies, and A. Navrotsky, Journal of the American Ceramic Society **69**, 453 (2005).

[41] P. K. Davies and A. Navrotsky, Journal of Solid State Chemistry **38**, 264 (1981).

[42] D. Keen and A. Goodwin, Nature **521**, 303 (2015).

[43] E. O'Quinn, K. Sickafus, R. Ewing, G. Baldinozzi, J. Neuefeind, M. Tucker, A. Fuentes, D. Drey, and M. Lang, Science Advances **6**, eabc2758 (2020).

[44] G. Anand, A. Wynn, C. Handley, and C. Freeman, Acta Materialia **146** (2017), 10.1016/j.actamat.2017.12.037.

[45] J. Kaufman and K. Esfarjani, Journal of Materials Research **36** (2021), 10.1557/s43578-021-00198-2.

[46] Z. Rák, J.-P. Maria, and D. Brenner, Materials Letters **217**, 300 (2018).

[47] D. Bérardan, A. Meena, S. Franger, C. Herrero, and N. Dragoe, Journal of Alloys and Compounds **704** (2017), 10.1016/j.jallcom.2017.02.070.

[48] A. Sarkar, R. Kruk, and H. Hahn, Dalton Trans. **50**, 1973 (2021).

[49] R. Witte, A. Sarkar, L. Velasco Estrada, R. Kruk, R. Brand, B. Eggert, K. Ollefs, E. Weschke, H. Wende, and H. Hahn, Journal of Applied Physics **127**, 185109 (2020).

[50] H. Zhu, H. Xie, Y. Zhao, S. Dai, M. Li, and X. Wang, Journal of Magnetism and Magnetic Materials **535**, 168063 (2021).

[51] J. Zhang, J. Yan, S. Calder, Q. Zheng, M. A. McGuire, D. L. Abernathy, Y. Ren, S. H. Lapidus, K. Page, H. Zheng, J. W. Freeland, J. D. Budai, and R. P. Hermann, Chemistry of Materials **31**, 3705 (2019).

[52] J. A. Mydosh, *Spin glasses: an experimental introduction* (CRC Press, 1993).

[53] W. L. Roth, Phys. Rev. **110**, 1333 (1958).

[54] D. Betto, Y. Peng, S. Porter, G. Berti, A. Calloni, G. Ghiringhelli, and N. Brookes, Physical Review B **96** (2017), 10.1103/PhysRevB.96.020409.

[55] Z. Rák and D. W. Brenner, Journal of Applied Physics **127**, 185108 (2020).

[56] M.-P. Jimenez-Segura, T. Takayama, D. Bérardan, A. Hoser, M. Reehuis, H. Takagi, and N. Dragoe, Applied Physics Letters (2019).

[57] J. Ghijsen, L.-H. Tjeng, H. Eskes, G. Sawatzky, and R. Johnson, Physical Review B - Condensed Matter and Materials Physics **42**, 2268 (1990).

[58] M. Moretti, *Magnetic and orbital resonant inelastic soft x-ray scattering*, Phd thesis, Politecnico di Milano (2011).

[59] "Crystal field theory," in *Electronic Structure and Properties of Transition Metal Compounds* (John Wiley Sons, Ltd, 2010) Chap. 4, pp. 84–131.

[60] J. C. Slater and G. F. Koster, Phys. Rev. **94**, 1498 (1954).

[61] N. Brookes, F. Yakhou-Harris, K. Kummer, A. Fondacaro, J. Cezar, D. Betto, E. Velez-Fort, A. Amorese, G. Ghiringhelli, L. Braicovich, R. Barrett, G. Berruyer, F. Cianciosi, L. Eybert, P. Marion, P. van der Linden, and L. Zhang, Nuclear In-

struments and Methods in Physics Research Section A: Accelerators, Spectrometers, Detectors and Associated Equipment **903**, 175 (2018).

[62] V. Strocov, T. Schmitt, U. Flechsig, T. Schmidt, A. Imhof, Q. Chen, J. Raabe, R. Betemps, D. Zimoch, J. Krempaský, X. Wang, M. Grioni, A. Piazzalunga, and L. Patthey, Journal of synchrotron radiation **17**, 631 (2010).

[63] K. Zhou, A. Walters, M. García-Fernández, T. Rice, M. Hand, A. Nag, J. Li, S. Agrestini, P. Garland, H. Wang, S. Alcock, I.-T. Nistea, B. Nutter, N. Rubies, G. Knap, M. Gaughran, F. Yuan, P. Chang, J. Emmins, and G. Howell, Journal of Synchrotron Radiation **29** (2022), 10.1107/S1600577522000601.

[64] J. Dvorak, I. Jarrige, V. Bisogni, S. Coburn, and W. Leonhardt, Review of Scientific Instruments **87**, 115109 (2016).

[65] L. J. P. Ament, "Resonant inelastic x-ray scattering studies of elementary excitations," (2010).

[66] L. J. P. Ament, M. van Veenendaal, T. P. Devereaux, J. P. Hill, and J. van den Brink, Rev. Mod. Phys. **83**, 705 (2011).

[67] G. Ghiringhelli, N. B. Brookes, E. Annese, H. Berger, C. Dallera, M. Grioni, L. Perfetti, A. Tagliaferri, and L. Braicovich, Phys. Rev. Lett. **92**, 117406 (2004).

[68] J. P. Hu, D. J. Payne, R. G. Egdell, P.-A. Glans, T. Learmonth, K. E. Smith, J. Guo, and N. M. Harrison, Phys. Rev. B **77**, 155115 (2008).

[69] M. M. Sala, V. Bisogni, C. Aruta, G. Balestrino, H. Berger, N. B. Brookes, G. M. de Luca, D. D. Castro, M. Grioni, M. Guarise, P. G. Medaglia, F. M. Granozio, M. Minola, P. Perna, M. Radovic, M. Salluzzo, T. Schmitt, K. J. Zhou, L. Braicovich, and G. Ghiringhelli, New Journal of Physics **13**, 043026 (2011).

[70] L. J. P. Ament, G. Ghiringhelli, M. M. Sala, L. Braicovich, and J. van den Brink, Phys. Rev. Lett. **103**, 117003 (2009).

[71] D. Betto, R. Fumagalli, L. Martinelli, M. Rossi, R. Piombo, K. Yoshimi, D. Di Castro, E. Di Gennaro, A. Sambri, D. Bonn, G. A. Sawatzky, L. Braicovich, N. B. Brookes, J. Lorenzana, and G. Ghiringhelli, Phys. Rev. B **103**, L140409 (2021).

[72] R. Fumagalli, L. Braicovich, M. Minola, Y. Y. Peng, K. Kummer, D. Betto, M. Rossi, E. Lefrançois, C. Morawe, M. Salluzzo, H. Suzuki, F. Yakhou, M. Le Tacon, B. Keimer, N. B. Brookes, M. M. Sala, and G. Ghiringhelli, Phys. Rev. B **99**, 134517 (2019).

[73] E. Previato, SIAM Review **46**, 349 (2004).

[74] "Schematic representation of the esrf," `https://www.esrf.fr/home/UsersAndScience/Accelerators.html` (), accessed: 2023-08-29.

[75] "Id32 beamline optics," `https://www.esrf.fr/home/UsersAndScience/Experiments/EMD/ID32/optics.html` (), accessed: 2023-08-29.

[76] R. Reininger and A. Castro, Nuclear Instruments Methods in Physics Research Section A-accelerators Spectrometers Detectors and Associated Equipment - NUCL INSTRUM METH PHYS RES A **538**, 760 (2005).

[77] M. Grioni, J. F. van Acker, M. T. Czyžyk, and J. C. Fuggle, Phys. Rev. B **45**, 3309 (1992).

[78] F. Tavani, M. Fracchia, A. Tofoni, L. Braglia, A. Jouve, S. Morandi, M. Manzoli, P. Torelli, P. Ghigna, and P. D'Angelo, Phys. Chem. Chem. Phys. **23**, 26575 (2021).

[79] M. Medarde, A. Fontaine, J. L. García-Muñoz, J. Rodríguez-Carvajal, M. de Santis, M. Sacchi, G. Rossi, and P. Lacorre, Phys. Rev. B **46**, 14975 (1992).

[80] S. R. Barman, A. Chainani, and D. D. Sarma, Phys. Rev. B **49**, 8475 (1994).

[81] M. Magnuson, S. Butorin, J. Guo, and J. Nordgren, Physical Review B **65** (2012), 10.1103/PhysRevB.65.205106.

[82] D. Zhu, Q. Cao, Q. Ruimin, S. Zhu, W. Yang, W. Xia, Y. Tian, L. Guo-Lei, and S. Yan, Scientific Reports **6**, 24188 (2016).

[83] F. Frati, M. O. J. Y. Hunault, and F. M. F. de Groot, Chemical Reviews **120**, 4056 (2020), pMID: 32275144, https://doi.org/10.1021/acs.chemrev.9b00439 .

[84] M. M. Sala, V. Bisogni, C. Aruta, G. Balestrino, H. Berger, N. B. Brookes, G. M. de Luca, D. D. Castro, M. Grioni, M. Guarise, P. G. Medaglia, F. M. Granozio, M. Minola, P. Perna, M. Radovic, M. Salluzzo, T. Schmitt, K. J. Zhou, L. Braicovich, and G. Ghiringhelli, New Journal of Physics **13**, 043026 (2011).

[85] M. T. Hutchings and E. J. Samuelsen, Phys. Rev. B **6**, 3447 (1972).

[86] M. Blume, Journal of Applied Physics **57**, 3615 (1985).

[87] W. Schuelke, *Electron Dynamics by Inelastic X-Ray Scattering*, Oxford Series on Synchrotron Radiation (OUP Oxford, 2007).